

ACCURACY AND PATIENT DOSE IN NEUTRON STIMULATED EMISSION
COMPUTED TOMOGRAPHY FOR DIAGNOSIS OF IRON OVERLOAD:
SIMULATIONS IN GEANT4

by

Anuj Jawahar Kapadia

Department of Biomedical Engineering
Duke University

Date: _____

Approved:

Georgia D. Tourassi, Ph.D., Supervisor

Gregg E. Trahey, Ph.D., Supervisor

Calvin R. Howell, Ph.D.

Joseph Y. Lo, Ph.D.

Rendon C. Nelson, M.D.

Dissertation submitted in partial fulfillment of
the requirements for the degree of Doctor of Philosophy
in the Department of Biomedical Engineering
in the Graduate School
of Duke University

2007

ABSTRACT

ACCURACY AND PATIENT DOSE IN NEUTRON STIMULATED EMISSION

COMPUTED TOMOGRAPHY FOR DIAGNOSIS OF IRON OVERLOAD:

SIMULATIONS IN GEANT4

by

Anuj Jawahar Kapadia

Department of Biomedical Engineering
Duke University

Date: _____

Approved:

Georgia D. Tourassi, Ph.D., Supervisor

Gregg E. Trahey, Ph.D., Supervisor

Calvin R. Howell, Ph.D.

Joseph Y. Lo, Ph.D.

Rendon C. Nelson, M.D.

An abstract of a dissertation submitted in partial fulfillment of
the requirements for the degree of Doctor of Philosophy
in the Department of Biomedical Engineering
in the Graduate School of Duke University

2007

Copyright by
Anuj Jawahar Kapadia
2007

Abstract

Neutron stimulated emission computed tomography (NSECT) is being proposed as an experimental technique to diagnose iron overload in patients. Proof-of-concept experiments have suggested that NSECT may have potential to make a non-invasive diagnosis of iron overload in a clinical system. The technique's sensitivity to high concentrations of iron combined with tomographic acquisition ability gives it a unique advantage over other competing modalities. While early experiments have demonstrated the efficacy of detecting samples with high concentrations of iron, a tomography application for patient diagnosis has never been tested. As with any other tomography system, the performance of NSECT will depend greatly on the acquisition parameters that are used to scan the patient. In order to determine the best acquisition geometry for a clinical system, it is important to evaluate and understand the effects of varying each individual acquisition parameter on the accuracy of the reconstructed image. This research work proposes to use Monte-Carlo simulations to optimize a clinical NSECT system for iron overload diagnosis.

Simulations of two NSECT systems have been designed in GEANT4, a spectroscopy system to detect uniform concentrations of iron in the liver, and a tomography system to detect non-uniform iron overload. Each system has been used to scan simulated samples of both disease models in humans to determine the best scanning strategy for each. The optimal scanning strategy is defined as the combination

of parameters that provides maximum accuracy with minimum radiation dose. Evaluation of accuracy is performed through ROC analysis of the reconstructed spectrums and images. For the spectroscopy system, the optimal acquisition geometry is defined in terms of the number of neutrons required to detect a clinically relevant concentration of iron. For the tomography system, the optimal scanning strategy is defined in terms of the number of neutrons and the number of spatial and angular translation steps used during acquisition. Patient dose for each simulated system is calculated by measuring the energy deposited by the neutron beam in the liver and surrounding body tissue.

Simulation results indicate that both scanning systems can detect wet iron concentrations of 5 mg/g or higher. Spectroscopic scanning with sufficient accuracy is possible with 1 million neutrons per scan, corresponding to a patient dose of 0.02 mSv. Tomographic scanning requires 8 angles that sample the image matrix at 1 cm projection intervals with 4 million neutrons per projection, which corresponds to a total body dose of 0.56 mSv.

The research performed for this dissertation has two important outcomes. First, it demonstrates that NSECT has the clinical potential for iron overload diagnosis in patients. Second, it provides a validated simulation of the NSECT system which can be used to guide future development and experimental implementation of the technique.

Acknowledgments

There are so many people to thank for helping me achieve what would otherwise have been a distant dream. It has been an eventful journey with many highs and lows, right from almost not being allowed to enter the United States to losing my mentor last year. It has not been an easy ride for any of the people involved.

I am indebted to my advisor Gina Tourassi for taking on the responsibility of handling not one but two additional students after Carey's passing. She has been extremely supportive with everything from answering my distress emails at 3:00 am to helping with last minute changes to experiments. I consider myself lucky to have been able to work under her guidance.

I would like to thank our in-house computer guru Brian Harrawood for his tremendous contribution to the development of the simulation. His help with coding, debugging, scripting and data management have gone a long way in helping me retain my sanity.

Thanks go out to Calvin Howell for his outstanding guidance with nuclear physics, and Matthew Kiser and Alexander Crowell for making those long arduous nights of data acquisition in TUNL almost entertaining. I would also like to acknowledge Anthony Hutcheson and Anton Tonchev for their help with gamma detector setup and acquisition.

I would like to thank each member of the Duke Advanced Imaging Laboratories, for their contributions to the NSECT project, especially Janelle Bender and Amy Sharma for their insightful discussions, comments and critique on my work. Special thanks go out to Joseph Lo for being like a second advisor during Carey's absence. His help and guidance have been invaluable.

I would like to thank my wife and my family for their unconditional support and constant encouragement. Their faith and belief has been very important in achieving this milestone. I can only hope that I continue to make them proud with all my future endeavors.

Finally, I am indebted to my mentor Carey E. Floyd Jr. for his help, guidance and support all through this journey. He will always be a role model both as an advisor and as a human being. From him I learnt that a passion for science and new research ideas and above all, dedication to students were of utmost importance to make a career in research and academia. I wish he had been alive to share this moment with me, a milestone in my academic career and hope that he is proud of the work he helped create. Here's to you, Carey!



In memory of

Dr. Carey E. Floyd, Jr.

a dedicated scientist, advisor, mentor, colleague and friend
March 17, 1954 – August 28, 2006

Contents

Abstract	iv
Acknowledgments.....	vi
List of Tables.....	xii
List of Figures	xiv
List of Abbreviations	xviii
1. Introduction	1
1.1 Preview of Chapters.....	2
2. Background.....	4
2.1 Theoretical Foundation of NSECT	4
2.2 Clinical Potential of NSECT	7
2.3 Iron Overload Disorders	8
2.3.1 Hemochromatosis and Hemosiderosis	8
2.3.2 Current Diagnostic Techniques.....	9
3. Hypothesis.....	14
3.1 Parameter Optimization	14
3.2 Simulations	15
4. Monte-Carlo Simulation Design of the NSECT System	17
4.1 Simulation Geometry.....	18
4.1.1 Neutron Source.....	20
4.1.2 Gamma Detectors.....	21
4.1.3 Tomographic Gantry	23

4.2	Samples	24
4.2.1	Samples for System Evaluation.....	26
4.2.1.1	Natural Iron Spectroscopic Sample.....	26
4.2.1.2	Composite Mixture Spectroscopic Sample.....	26
4.2.1.3	Composite Iron-Copper Tomographic Sample	27
4.2.2	Iron Overload Sample for Spectroscopic Analysis.....	30
4.2.3	Torso Iron Overload Sample for Tomography	32
4.3	Physics Lists	36
5.	NSECT System Evaluation for Spectroscopy.....	39
5.1	Spectral Analysis	41
5.1.1	Background Reduction.....	41
5.1.2	Identification of Energy Peaks.....	46
5.1.3	Element Matching	49
5.1.4	Statistical Analysis	50
5.2	Comparison of Simulated and Experimental Spectrums.....	51
5.2.1	Natural Iron Spectroscopic Sample	52
5.2.2	Composite Mixture Spectroscopic Sample	55
5.3	Iron Overload Sensitivity Analysis	58
6.	NSECT System for Tomography	72
6.1	Tomography in NSECT	72
6.1.1	Acquisition Geometry.....	73
6.1.2	Reconstruction Algorithm.....	74

6.1.2.1	Overview of Fourier Based and Algebraic Algorithms.....	74
6.1.2.2	Maximum Likelihood Expectation Maximization	77
6.1.3	Monte-Carlo Simulation of MLEM Probability Matrix.....	81
6.2	Evaluation of NSECT Tomography System Simulation	84
6.3	Tomographic Simulation of Iron Overload Sample	95
6.3.1	Acquisition Geometry.....	105
6.3.2	Reconstructed Images.....	108
6.3.3	ROC Analysis.....	119
7.	Optimization of NSECT Scanning Strategy	133
7.1	Calculation of Patient Dose.....	133
7.2	Optimum Acquisition Geometry	139
8.	Summary, Conclusion and Future Work	141
8.1	Summary of Findings.....	141
8.2	Conclusion.....	143
8.3	Future Work	144
References	146
Biography	152

List of Tables

Table 1: Elemental composition of the liver phantom	31.
Table 2: Representative iron values in normal subjects, patients with hemochromatosis, and patients with alcoholic liver disease	34.
Table 3: Elemental composition of human skeletal bone	35.
Table 4: Analysis of simulated and experimental spectrums natural iron sample.....	53.
Table 5: Analysis of simulated and experimental spectrums for composite sample	57.
Table 6: Results of ROC analysis for spectroscopic sensitivity testing.....	69.
Table 7: Accuracy of spectroscopic measurement for 3 values of neutron flux.....	69.
Table 8: Analysis of gamma energy peaks from the simulated and experimental spectrums for the mixed iron-copper tomographic sample	88.
Table 9: Summary of the differences in widths of the reconstructed regions in the simulated and experimental images	94.
Table 10: Tomographic acquisition geometries evaluated for detection of iron overload in the liver	106.
Table 11: Results of ROC analysis for the 10 mg/g lesion compared with the liver background	121.
Table 12: Ratio of pixel values within the 10 mg/g and 20 mg/g lesions	126.
Table 13: Results of ROC analysis for the 5 mg/g lesion compared with the normal liver background	127.
Table 14: Results of ROC analysis for the 3 mg/g lesion compared with the normal liver background	129.

Table 15: Effective dose delivered from an NSECT spectroscopy scan with 1 million incident neutrons	136.
Table 16: Effective dose delivered from an NSECT tomography scan corresponding to the optimal set of acquisition parameters.....	138.
Table 17: Dose values for different combinations of acquisition parameters.....	140.

List of Figures

Figure 1: Principle of NSECT	5.
Figure 2: Example of a complex object in Geant4.....	19.
Figure 3: Composite iron-copper tomographic sample.....	28.
Figure 4. Geant4 simulation of the iron-copper sample system.....	29.
Figure 5: Abdominal CT scan showing the liver	30.
Figure 6: Liver iron overload sample for sensitivity analysis.....	31.
Figure 7: Abdominal CT scan in the coronal and transverse planes	32.
Figure 8: Simulated liver chamber of the tomographic torso phantom	33.
Figure 9. Geant4 simulation of the torso tomography phantom.....	35.
Figure 10: Example of energy spread in gamma line for a ^{56}Fe sample	40.
Figure 11: Example of sample-out background from a water sample	43.
Figure 12: Example of sample-out background correction for iron sample in water.....	44.
Figure 13: Example of polynomial curve-fitting for residual background correction	45.
Figure 14: Example of dynamic thresholding for peak identification.....	47.
Figure 15: Example of automatic peak finding tool applied to sample iron spectrum....	48.
Figure 16: Example of statistical significance testing for two spectrums.....	51.
Figure 17: Comparison of simulated and experimental gamma spectrums for a natural iron sample in air	53.
Figure 18: Example of energy dependent detector efficiency	55.

Figure 19: Comparison of simulated and experimental normalized gamma spectrums for the Fe, NaCl and KCl composite sample	56.
Figure 20: GEANT4 simulation of iron overload spectroscopic analysis	63.
Figure 21: Simulated gamma spectrum from a water sample	64.
Figure 22: Simulated gamma spectrum from calibration sample (Fe = 25 mg/g) with background correction	66.
Figure 23: Simulated gamma spectrum from liver with iron overload (Fe =3 mg/g) with background correction	67.
Figure 24: GEANT4 tomography simulation for the composite iron-copper tomographic sample.....	85.
Figure 25: Comparison of simulated and experimental normalized gamma spectrums for the iron-copper tomography sample.....	87.
Figure 26: Comparison of the modulation in detected iron counts at each projection of the simulated and experimental simulation	90.
Figure 27: Reconstructed images of copper from simulated and experimental acquisition of the iron-copper N-sample	92.
Figure 28: Reconstructed images of iron from simulated and experimental acquisition of the iron-copper mixed N-sample.....	92.
Figure 29: Combined reconstructed images from simulated and experimental acquisition of the iron-copper mixed N-sample	93.
Figure 30: Line profile of the intensity distribution through the simulated and experimentally reconstructed images	94.
Figure 31: Gamma detector array geometry placed around the iron overload torso sample.....	98.
Figure 32: Comparison of gamma spectrums for the array detectors with different diameters.....	99.

Figure 33: Gamma spectrum for an iron sample in water with elastic scatter included in the system.....	101.
Figure 34: Comparison of gamma spectrums from an iron sample in water with and without elastic scatter	102.
Figure 35: Variation in the SNR for 4 regions of interest in an image from iron with successive iterations of MLEM.....	110.
Figure 36: Reconstructed image for ^{56}Fe showing successive iterations of the MLEM algorithm	112.
Figure 37: Reconstructed image for ^{12}C showing successive iterations of the MLEM algorithm	114.
Figure 38: Comparison of the original sample with the corresponding reconstructed image for carbon	115.
Figure 39: Comparison of the original sample with the corresponding reconstructed image for iron	115.
Figure 40: Effect of downsampling the number of neutron counts on the reconstructed image.....	116.
Figure 41: Effect of downsampling the number of angular positions on the reconstructed image.....	117.
Figure 42: Effect of downsampling the number of spatial steps on the reconstructed image.....	118.
Figure 43: Regions corresponding to locations of known iron concentrations in the reconstructed image	120.
Figure 44: Variation in Az values with reducing neutron counts and angular positions for the 10 mg/g lesion	122.
Figure 45: Variation in Az values with reducing neutron counts and angular positions for the 10 mg/g lesion	123.

Figure 46: Variation in Az values with reducing neutron counts and angular positions for the 10 mg/g lesion	123.
Figure 47: Variation in Az values with reducing neutron counts and angular positions for the 10 mg/g lesion	124.
Figure 48: Variation in Az values with reducing neutron counts and angular positions for the 5 mg/g lesion	128.
Figure 49: Variation in Az values with reducing neutron counts and angular positions for the 5 mg/g lesion	128.
Figure 50: Variation in Az values with reducing neutron counts and angular positions for the 3 mg/g lesion	130.
Figure 51: Variation in Az values with reducing neutron counts and angular positions for the 3 mg/g lesion	130.
Figure 52: Reconstructed images for the optimized scan of a normal sized human liver sample.....	131.
Figure 53: Geometry for scanning the tomographic liver to measure patient dose	137.

List of Abbreviations

ART	: Arithmetic Reconstruction Technique
AUC	: Area under ROC Curve
BRT	: Bayesian Reconstruction Technique
CT	: Computed Tomography
EM	: Expectation Maximization
FBP	: Filtered Back-Projection
FT	: Fourier Transform
HPGe	: High Purity Germanium
IFT	: Inverse Fourier Transform
MLEM	: Maximum Likelihood Expectation Maximization
MRI	: Magnetic Resonance Imaging
MRS	: Magnetic Resonance Spectroscopy
NSECT	: Neutron Stimulated Emission Computed Tomography
RBE	: Relative Biological Equivalent
ROC	: Receiver Operating Characteristic
ROI	: Region of Interest
SIRT	: Simultaneous Iterative Reconstruction Technique
TOF	: Time of Flight
TUNL	: Triangle Universities Nuclear Laboratory

1. Introduction

Neutron stimulated emission computed tomography (NSECT) is being developed as a novel tomographic approach to measure the concentration of trace elements in the body at micro-molar levels. An NSECT system uses spectral information obtained from inelastic scattering reactions between neutrons and a target atomic nucleus to identify the atom and determine its concentration in the tissue [1, 2]. Several studies have shown that analysis of the concentration in a tissue can be used to detect certain diseases that are characterized by concentration changes [3-8]. The theoretical principles of NSECT suggest that it may have the potential to perform non-invasive identification and measurement of elevated concentration levels in diseased organs in the body.

Specifically, this dissertation explores the possibility of using NSECT for the diagnosis of hemochromatosis, also known as iron overload in the liver. Iron overload in the liver is currently diagnosed by quantifying the concentration of liver iron through an invasive biopsy [9-11]. Repeated invasive biopsies are difficult to perform in patients due to the morbidity and potential complications associated with them. There is a need for a non-invasive technique that can determine element concentrations in the liver without subjecting a patient to the inconvenience associated with an invasive biopsy.

Here we present NSECT as a possible alternative for diagnosis of liver iron overload and investigate parameter-optimization for tomographic imaging of the liver in a clinical scenario.

1.1 Preview of Chapters

The goal of this work is to optimize a novel imaging technique to diagnose an existing clinical disorder in patients. Proof-of-concept experiments were performed as early as 2003 to investigate if there was any possibility of performing NSECT scans for biological imaging. As a result, the development and progress of the research described here was often performed through a series of independent experiments, some often running simultaneously with the experimental implementation. Care has been taken to ensure that the role of each independent experiment in the overall project is clear to the reader.

Chapter 2 provides an introduction to the principles of NSECT and describes its role in the clinical diagnosis of iron overload disorders. As some readers may not be familiar with iron overload disorders, a brief overview of the clinical implications of iron overload along with an overview of clinical techniques currently used for diagnosis are included.

Chapter 3 presents the working hypothesis of the study and provides justification for choosing Monte-Carlo simulations to evaluate the hypothesis.

Chapter 4 discusses the design and development of a Monte-Carlo simulation for diagnosis of iron overload in patients. Each part of the development process is described in detail with regards to the tomographic acquisition system, neutron source, gamma detectors and simulated samples for system evaluation and testing. Finally, the chapter

describes how the samples are developed for clinical disease models of different types of iron overload.

Chapter 5 describes the validation and testing of the NSECT simulation for spectroscopic acquisitions. The simulated system is first tested and validated against experimental data for non-tissue samples. After satisfactory validation, the simulation is used to perform a study to investigate NSECT's ability to diagnose iron overload through spectroscopy.

Chapter 6 extends the spectroscopic acquisition model to tomography and introduces the differences between the two applications. The tomography system is first validated with data acquired from a physical sample, and upon satisfactory validation, is then used to identify a possible set of acquisition parameters for imaging iron distributions in the liver.

Chapter 7 addresses the issue of patient dose and describes the technique that is used to calculate the dose delivered from an NSECT scan.

A summary of the research findings and conclusions are presented in chapter 8, along with possible extensions for future research work.

2. Background

2.1 *Theoretical Foundation of NSECT*

Neutron Stimulated Emission Computed Tomography (NSECT) is a spectroscopic technique to obtain quantitative information about the distribution of elements in a body using inelastic scatter interactions between incident neutrons and target nuclei. A beam of fast neutrons is used to stimulate atomic nuclei in the target sample to emit characteristic gamma rays that are collected in an energy-sensitive gamma spectrometer. This technique uses a spectroscopic approach to analyze changes in element concentrations in organs of interest. This analysis is performed by obtaining spectral information about the sample through inelastic scattering interactions between neutrons and target atomic nuclei to identify the nuclear isotope and determine its concentration in the tissue.

Principle: A neutron, incident on a body, travels freely along its projected path until it collides with an atomic nucleus. If the neutron scatters inelastically with the atomic nucleus, the nucleus gets excited into one of its quantized higher-energy states. Often the excited nucleus will rapidly decay to a lower energy state, emitting a gamma-ray photon whose energy is equal to the difference between the two states (Figure 1). As these energy states are well established and mostly unique to each isotope, the energy of the emitted gamma photon becomes a unique signature of the emitting nucleus.

Detection and analysis of the emitted gamma ray spectrum enables identification and quantification of the target atom.

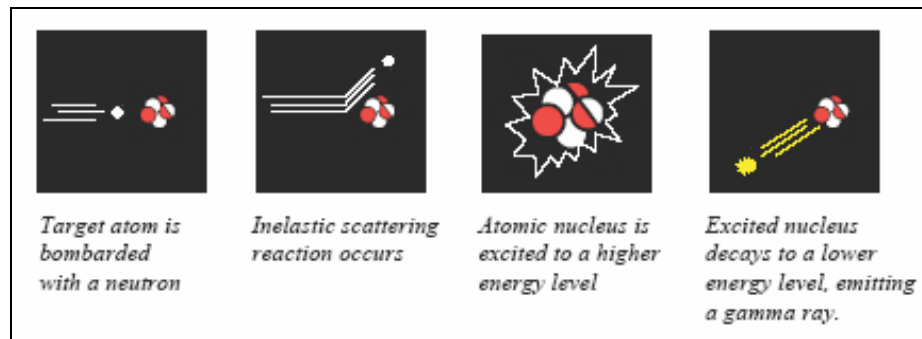


Figure 1. Principle of Neutron Stimulated Emission Computed Tomography (NSECT)

Gamma ray measurement in NSECT is performed simultaneously with irradiation of the sample as in the case of prompt gamma neutron activation analysis (PGNAA). However, these two techniques differ greatly in the method of gamma ray production. PGNAA relies on neutron capture interaction followed by prompt gamma emission, while NSECT uses inelastic scatter spectroscopy to identify the scattering isotope without inducing radioactivity in the sample.

While the principles of NSECT are somewhat similar to those of gamma ray emission computed tomography (G-ECT), NSECT differs from G-ECT in that the gamma-rays are emitted by excited stable isotopes as opposed to emission-decay from radioactive tracers. This provides a unique advantage over G-ECT techniques in not having to inject or induce radioactive tracers in the patient. Stable isotopes that are

naturally present in the body can be used to obtain quantitative information about their spatial distribution.

While NSECT can be used over a wide range of elements and isotopes, the elements of interest for medical applications show characteristic gamma lines with energies ranging from 350 keV to 6500 keV. As a result, NSECT cannot use standard gamma cameras that are normally used in G-ECT. These gamma cameras are unable to provide sufficient spatial or energy resolution for NSECT imaging. NSECT uses high purity germanium (HPGe) detectors which exhibit excellent energy resolution within the range of NSECT energies. Unfortunately, HPGe detectors with adequate efficiency are usually large single-crystal detectors that do not have the ability to provide spatial information. Spatial information in NSECT is obtained from the position of the neutron beam which illuminates a single projection path at a time.

The NSECT technique is a computed tomography extension of neutron inelastic scatter spectroscopy. A thin neutron beam is used to illuminate a line projection of characteristic gamma intensities through the sample. The beam is rotated and translated through multiple positions in the sample to obtain a set of tomographic projections. These projections can be reconstructed to obtain a quantitative map of the spatial distribution of each element in the body.

As described in the following section, this application of inelastic scatter tomography is useful for a variety of disorders that exhibit changes in element concentrations in the body.

2.2 Clinical Potential of NSECT

There are several diseases in humans that are characterized by changes in element concentrations within the diseased tissue [3, 4, 12-16]. Many of these diseases require invasive biopsies to determine the severity of the disease. For example, diseases such as hemochromatosis and Wilson's disease exhibit changes in iron and copper concentrations in the liver [11, 17]. These disorders are diagnosed through invasive liver biopsy to determine the severity of the disease. NSECT provides a non-invasive alternative with the potential to obtain the same information without the need for a biopsy. Further, several cancers such as breast, prostate and brain cancer have been associated with changes in the concentration of trace elements in the diseased organ [3, 4, 6, 12, 18, 19]. Often these changes are observed much earlier than morphological changes associated with cancer. Quantifying these elements can provide *in-vivo* cancer diagnosis at very early stages when concentrations of trace elements in tissue begin to change. Trace element concentration changes have also been reported in Alzheimer's disease [20-23], renal disease [24-26] and cardiac disorders [27-31].

This thesis focuses specifically on detection of iron overload disorders in the liver. The following sections present a brief overview of common iron overload disorders in the liver along with their currently preferred diagnostic methods.

2.3 *Iron Overload Disorders*

2.3.1 Hemochromatosis and Hemosiderosis

Hereditary hemochromatosis is a genetic iron storage disorder characterized by an inappropriate increase in intestinal iron absorption. It is one of the most common autosomal recessive disorders and is observed primarily in European and American populations, where approximately 1 in 10 persons is a heterozygous carrier while 3 in 1000 persons are homozygotes [10, 11]. An increase in absorption of iron by the intestine leads to excessive iron deposits in parenchyma cells of organs. As the body lacks an effective mechanism for eliminating excess iron, this iron accumulates in organs such as the liver, heart, spleen, pancreas and kidney, which may cause extensive tissue damage, liver cirrhosis, cardiac failure, hepatic failure, and hepatocellular carcinoma. Total body iron content in advanced stages of the disorder may often increase by up to 5 times the normal (i.e. from 3-4 grams to over 20 grams total) [10, 11]. Although the disorder affects both men and women, clinical expression in men is 5-10 times higher. Women are usually diagnosed much later as their bodies are able to remove some iron through blood loss from menstruation and pregnancy.

In addition to the hereditary form, a non-genetic form of iron overload is sometimes seen in conjunction with chronic disorders such as thalassemia major, myelodysplasia (including sideroblastic anemia), and moderate aplastic anemia where patients receive frequent blood transfusions as part of treatment procedures. Since the body cannot effectively eliminate the excess transfusion iron, it gets stored in organs, mostly in the liver, heart and spleen. This acquired form is commonly referred to as hemosiderosis or transfusion iron overload, and is seen to occur more frequently than hereditary hemochromatosis. Studies have reported transfusion iron overload prevalence as high as 44% in patients receiving transfusion for thalassemia major [32].

Accurate measurement of the body's iron content is vital for effective diagnosis and management of iron-overload disorder [9, 33]. Since a significant part of the body's total iron is stored in the liver, an estimate of the liver's iron concentration is used as an accurate measure of the body's total iron content. The morbidity associated with the currently accepted technique of diagnosis, invasive liver biopsy, poses several limitations in monitoring the progress of the disorder.

2.3.2 Current Diagnostic Techniques

The currently preferred technique for definitive measurement of iron overload is liver biopsy [9, 34]. Like most others, this biopsy is an unpleasant procedure associated with several potential complications such as infection and bleeding, which in a small number of cases may even lead to death. Repeated biopsy is often required for

monitoring the disease. The morbidity associated with performing repeated biopsy creates two obstacles, one, in following the progress of patients obtaining therapeutic treatments, and two, in developing new forms of treatment for the disorder. Results from biopsy also suffer from a 20% margin of error, primarily due to errors in tissue sampling [35, 36]. A workshop conducted by the National Institute of Diabetes and Digestive and Kidney Diseases (NIDDK) to assess the needs for techniques to determine iron concentration in the body concluded that “physicians have a pressing clinical need for quantitative means of measuring body storage iron that are noninvasive, safe, accurate, and readily available to improve the diagnosis and management of patients with iron overload, including those with hereditary hemochromatosis, thalassemia major, sickle cell disease, aplastic anemia, myelodysplasia, and other disorders” [37].

Although several attempts have been made to expand existing diagnostic imaging modalities to include non-invasive quantification of tissue element concentration, few have shown satisfactory results in clinical scenarios. NSECT’s immediate competition comes primarily from X-ray CT, Magnetic Resonance Imaging (MRI) and MR Spectroscopy (MRS).

X-ray CT shows an increase in liver density on the CT image due to increased attenuation of x-rays by the excess iron deposited in the liver. Several studies have been performed to evaluate this relationship between iron concentration and liver density in the CT image [38, 39]. While values of 70 H.U. have been reported for hepatic iron

concentration of 6mg/g liver dry weight, CT suffers from low specificity in detecting iron overload because there exist a number of other diseases such as Wilson's disease that also lead to increased x-ray attenuation within the liver [40]. Although some studies have reported inadequate sensitivity for liver iron concentrations below 6mg/g liver dry weight, the lower diagnostic limits for CT are generally unclear.

MRI obtains an indirect estimate of hepatic iron from the effect of ferritin and hemosiderin iron on the proton resonance behavior of tissue water. Bound iron exhibits paramagnetic properties, and in the presence of an external magnetic field, sets up local magnetic fields of its own. These local fields interfere with the resonance behavior of protons in surrounding water, causing a loss in signal intensity in the MRI image. Iron concentration is determined by measuring this loss in signal. Several studies have been performed to assess the efficacy of MRI in quantifying hepatic iron. Although MRI shows greater specificity and sensitivity to hepatic iron quantification than CT, it suffers from the following drawbacks:

- Signal intensity in regions of high iron concentration (> 20 mg/g dry weight) is extremely low due to signal distortion from local magnetic fields, making it difficult to follow patients with the most severe iron overloading [41].
- It shows a small change in signal intensity in cases of mild or moderate iron overload (< 6 mg/g dry weight) due to low iron concentration in the liver, making it difficult to discriminate between different concentrations [40].

- The variability of the relationship between signal intensity and hepatic iron concentration is increased in the presence of fibrosis of any degree. Studies suggest that without a biopsy to determine whether or not fibrosis is present, the prediction interval for an estimate of the hepatic iron derived from MRI is too broad to be of any practical assistance in the management of transfusion iron overload [41].
- Studies have used a ratio of signal intensity between liver and muscle, based on an assumption that the iron concentration in muscle does not change with respect to hepatic iron [40]. This assumption may not be accurate as increases in muscle iron concentration have been observed in cases of African iron overload [11].

MRS detects the magnetic moments of target nuclei in different chemical structures, which have different characteristic resonance patterns depending on the interactions between neighboring chemical structures. Its application, however, is limited to a few elements as the number of nuclei with appropriate magnetic moments is limited. Most imaging has been performed on ^1H and ^{31}P and some on ^{13}C , ^{14}N , ^{19}F , and ^{23}Na . Although imaging studies have also been performed with Fe, a low signal from bound Fe makes quantification studies difficult. MRS also suffers from limited spatial resolution (larger than 1cm) [42].

Thus, each of the non-invasive techniques that have attempted to quantify iron has met with limited success due to limitation in sensitivity or resolution. CT and MRI lack sufficient sensitivity in detecting mild to moderate degrees of iron overload, while MRI also shows a lack of sensitivity in cases of severe iron overload.

The purpose of this thesis is to investigate and optimize NSECT as a clinically feasible non-invasive alternative to obtain an accurate measurement of liver iron concentration at clinically relevant values where other imaging modalities suffer from reduced sensitivity.

3. Hypothesis

As explained in the previous chapter, all current techniques for diagnosis of iron overload suffer from limitations. NSECT has the potential to develop into a quantitative diagnostic imaging for detection of liver iron overload in clinical scenarios. However, in order to achieve this, the NSECT system needs to be optimized to detect iron overload in the liver in clinically relevant scenarios.

This dissertation tests the following working hypothesis: It is possible to optimize a clinical setup for an NSECT system that can achieve clinically useful accuracy in iron overload detection, while at the same time maintaining clinically permissible levels of patient dose.

3.1 Parameter Optimization

Being a tomographic acquisition technique with potentially high levels of patient dose, it is imperative to optimize the various acquisition parameters to obtain the best possible image with the lowest achievable level of patient dose. In its current implementation, NSECT has 4 parameters that can be individually adjusted for different effects on the accuracy of the image and the associated patient dose. These parameters are: (a) Incident neutron flux, (b) Number of spatial projections, (c) Number of angular projections, (d) Number, size and location of the detectors. In order to optimize the

NSECT system, we must characterize the effects of each of these parameters on the resulting reconstructed image.

3.2 Simulations

NSECT experiments are currently performed using a nuclear accelerator source and high purity germanium (HPGe) gamma-ray detectors. Due to the inherently low efficiency of the acquisition geometry, NSECT experiments are prohibitively time consuming in nature. Each experimental acquisition requires approximately 2 days of scan time per sample to get adequate statistical accuracy in the detectors. As it is not feasible to run experiments to investigate the effect of each individual parameter, we need to have a valid simulation environment that will allow us to do this.

This dissertation proposes the use of Monte-Carlo simulations to model the NSECT acquisition system, and use these simulations to investigate the effects of different acquisition parameters on the reconstructed image. The use of simulations has the following advantages:

- a) Use of only computational resources
- b) No dependence on nuclear accelerator
- c) Easy to control each acquisition parameter individually
- d) Complete control over experimental conditions including physical interactions, background noise and overall efficiency of the geometry

While the iron storage mechanism of the liver is generally well understood, it has not yet been clearly demonstrated whether the excess iron stored in overloaded livers is stored uniformly or in patches of varying concentration within the liver. Liver biopsy measurements are generally taken from one or more regions that appear cirrhotic under ultrasound guidance, with the assumption that cirrhosis directly corresponds to elevated iron concentration. This relation between cirrhosis and iron concentration has not yet been clearly demonstrated. Thus, there are three possibilities for distribution of excess iron in the liver:

- a. As a uniform distribution throughout the liver
- b. As a non-uniform distribution located in areas of cirrhosis
- c. As a non-uniform distribution located randomly regardless of cirrhosis.

NSECT has the ability to generate quantitative tomographic images of the iron distribution in the liver in order to investigate all three possibilities of iron storage.

If successful, these extensive computer simulations can be verified empirically and used to guide development of a clinical imaging system for diagnosis of iron overload through NSECT. The following chapters present original research work to test the underlying study hypothesis.

4. Monte-Carlo Simulation Design of the NSECT System

As discussed in the previous chapter, optimization of the NSECT system to implement a clinical setup for iron overload diagnosis requires a Monte-Carlo simulation to allow system optimization without the need for a nuclear accelerator. The first step of this task is to develop a Monte-Carlo simulation tool to model the interactions between neutrons and atomic nuclei as a practical alternative to evaluate the effects of dose-reduction techniques on detection accuracy. This simulation will be designed using stochastic modeling methods in GEANT4 [43]. GEANT4 is a high-energy-physics object-oriented Monte-Carlo programming toolkit for simulating the passage of particles through matter. It has been developed by a worldwide collaboration of about 100 scientists in Europe, Russia, Japan, Canada and the United States. GEANT4, which stands for GEometry ANd Tracking (version 4), accounts for a diverse range of interactions of particles with matter across a wide energy range. It is an object-oriented programming package which incorporates a powerful set of random number generators, physics units and constants, and provides all the tools required for detector simulation including geometry, tracking and detector response management. Any object or material can be defined as a detector in GEANT4, which presents a readily feasible option for dose analysis experiments. GEANT4 provides visualization and an interactive user interface to visualize the simulated acquisition systems. Its programming package

allows individual simulation of different types of user-defined “objects” such as neutron sources and detectors composed of a single element or a mixture of elements, which can be integrated into a single module separately through its object-oriented nature.

The Monte-Carlo simulation of the NSECT system developed in GEANT4 is described in the following sections.

4.1 Simulation Geometry

The simulated NSECT system model consists of 3 parts – (a) Neutron Source, (b) Gamma Detectors, and (c) Tomographic Gantry. Each part is designed as a separate GEANT4 object to facilitate modifying individual parameters on one part independently of the others.

Objects in GEANT4 are constructed using a combination of one or more simple three-dimensional structures of any shape and size, filled with any desired material which can be built using a combination of elements and isotopes from its library. For example, it is possible to specify an object like a simple hollow box by defining it as a cube filled with air. It can then be connected to another cube, hemisphere, cone, or any other shape to form a complex structure based on a mathematical or logical relationship between the two, for example sum or difference of the two. An example of this object construction shown in figure 2, which shows a model of a human breast torso sample made up of a combination of an oval tube representing the torso, and two hemispherical regions for the breasts.

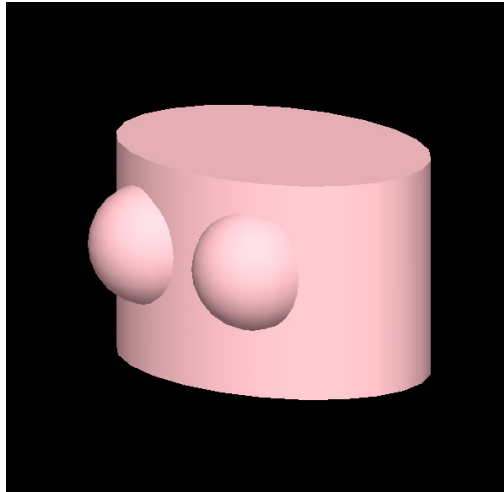


Figure 2. Example of a complex object in GEANT4. This object is created as a sum of simple three-dimensional structures to model a human breast torso sample, with the torso modeled as an oval tube, and the breasts modeled as hemispheres.

All simulations in GEANT4 require the creation of a finite virtual space called the 'world', which acts as the world for the experiment. This world defines the virtual space within which the experiment will occur. All sources, detectors and samples are placed in the world. Particle interactions are tracked only as long as they occur inside the world. Particles exiting the world are terminated. The world can be defined as any three-dimensional geometric object such as a cube or sphere of any shape or size. It can be filled with any material such as air, water or tissue. For all the simulations developed in this project, the world is defined as a cube with edge 1 m, and is filled with air. The 1 m dimension is large enough to accommodate all samples with their tomographic geometries designed in this simulation experiment along with gamma detectors placed at their necessary locations.

4.1.1 Neutron Source

The neutron source is created by defining an object called a 'GEANT4 Particle Gun', and assigning it three user-defined dynamic parameters:

- a. particle type (e.g. neutrons, gammas, positrons)
- b. particle energy (ranging from eV to GeV)
- c. beam width (ranging from μm to km)

Incident particle type can be set to a variety of particles including neutrons and gamma rays with energies ranging from a few eV to several GeV. For liver studies using NSECT, the particle gun is set to produce neutrons between 5 MeV to 7.5 MeV, identical to the particles produced by the accelerator source during the physical experiment. Each of these parameters can be modified at anytime during the experiment without having to recompile the code.

This particle gun is placed at the left edge of the world so that every particle exiting the gun enters directly into the world space. The exit position of the particle from the gun is given a user-specified width, which determines the width of the emitted neutron beam. GEANT4 executes each neutron as an individual event rather than a beam. Therefore, in order to create a multi-element neutron beam with a finite width, each neutron that exits the gun is assigned a randomly selected point of emission within a finite distance about the center of the gun. An integration of a large number of individual neutron events produces a beam with a finite user-specified width. The beam

widths in this simulation are varied between 5 mm and 10 mm to simulate different acquisition experiments.

Thus, a typical output of the 'GEANT4 Particle Gun' object is a collection of individual neutron events distributed randomly within a 5 mm width about the gun-center, forming a 5 MeV neutron beam with a 5 mm user-defined width.

4.1.2 Gamma Detectors

Gamma detectors are created as solid cylinders with two user-defined dimensions, diameter of 10 cm and height 9 cm. Each cylinder is filled with high-purity germanium (100% Ge, density= 5.32 g/cm³) to simulate the HPGe detectors used in the physical experiment.

The detector material is then 'sensitized', i.e. it is defined to track particle interactions and record the energy deposited at each interaction within the detector. For each interaction taking place within the detector volume, the following parameters are recorded:

- a. Neutron event number
- b. Type of interaction
- c. Energy deposited at each step of the interaction
- d. Energy and type of particle created from the interaction

In instances where a particle undergoes multiple interactions within an object, this information can be recorded for each subsequent event produced.

Each detector can be placed at any desired location in the GEANT4 world. In the current configuration, the detectors are placed at a backward angle of ± 135 degrees with respect to the sample in the beam plane to mimic the position of the detector in the physical experiment. The physical experiment uses the ± 135 degree configuration because a majority of the states of interest to NSECT decay by an electric quadrupole transition whose distribution has a maximum intensity at about 45 and 135 degrees. Using the 135 degree orientation helps reduce the neutron damage to the physical gamma detectors from neutrons that elastically scatter from the target.

The number of gamma detectors used in this simulation varies between 1 and 6. Although only two HPGe detectors were used in the physical experimental scan, six detectors have been used in the simulated system designed here to increase gamma-ray detection efficiency and reduce computing time. Gamma emissions through inelastic scatter occur in all directions around the sample. As each detector has a finite diameter and is placed at a finite length from the target, the solid angle presented by the detector face to the emitted gamma rays becomes very small. This leads to a significant reduction in the efficiency of gamma incidence on the detector. Using six detectors increases the efficiency of gamma ray incidence on the detector face by six-fold. All six detectors are placed at orientations of ± 135 degrees with respect to the beam.

Detector efficiency is modeled by collecting information from all events occurring in the detector and then retaining only a required fraction of these events. For

example, for a 60% efficient HPGe detector, 100% of events will be recorded, but only 60% of these will be used to generate spectral results.

4.1.3 Tomographic Gantry

As mentioned earlier, tomography is required for detection of non-uniform element distributions within a sample. Tomography in NSECT is currently performed in a manner similar to first generation CT with a stationary beam and single element detector. The sample is translated through the beam, then rotated through a finite angle and translated through the beam again. In the simulation, this translation-rotation is facilitated by a tomographic gantry which is designed as a gantry chamber within the world, filled with the same material as the world (air). The chamber can be rotated to any angle from 0-180 degrees in clockwise or anticlockwise direction, and can be moved to any desired xyz lateral position within the world. The user defines the number of translation and rotation positions along with the translation and rotation increments. Once a sample is created, it can simply be placed in the gantry chamber for rotation and translation along the gantry specified parameters. An example of this specified tomographic acquisition geometry is 11 spatial positions at increments of 10 mm with 8 angles at increments of 22.5 degrees to scan from 0 to 180 degrees.

Examples of this simulation with the world, object sample and gamma detectors are shown in the next section.

4.2 Samples

Samples in GEANT4 are created in a manner similar to that used for the detectors, i.e. we define a complex shape based on a combination of one or more simple shapes, and fill it with a material made from a combination of one or more elements. GEANT4 allows defining of complex materials such as liver tissue using a combination of simple elements from the GEANT4 material database. This database not only contains most elements and isotopes that commonly exist in nature, but also allows defining an unknown element by specifying its atomic and mass numbers. A compound molecule can be created as a combination of one or more elements in any desired proportion. For example, air can be created as a mixture of N₂ (78%), O₂ (21%), Ar (0.96%) and CO₂ (0.04%). In addition to these mixtures, GEANT4 also incorporates a list of standard reference materials derived from the National Institute of Standards and Technology (NIST) database of material properties. This database contains a list of NIST defined standard materials such as air, water, human muscle and human bone which can be directly incorporated into a simulation.

Three sets of samples have been created in this simulation. The first is a set of non-biological samples designed for evaluating the simulation of the NSECT system. These samples are based on real physical samples that were scanned during experimental NSECT acquisition in the nuclear laboratory. A comparison of gamma

energy spectra from the simulated samples with the corresponding real samples will be used for evaluation of the simulation.

The second and third samples model the human torso with iron overloaded livers. As mentioned earlier, since it has not been clearly demonstrated whether iron concentration in overloaded livers is uniform or occurs in patches throughout the liver, both scenarios have been implemented and modeled here.

Specifically, the second sample is that of a human torso with an iron overloaded liver with varying degrees of iron concentration in a uniform distribution. This sample is scanned using simple spectroscopic acquisition to investigate the limits of sensitivity for the current NSECT system.

The third sample is a tomographic acquisition sample of the human torso with simulated liver iron overload. This simulation models a non-uniform iron distribution in the form of two high-concentration 'lesions' of iron to evaluate simulated tomographic acquisition for detection of iron overload in the liver.

Each of these samples is described in detail in the sections below.

4.2.1 Samples for System Evaluation

Three non-biological samples have been designed to evaluate the GEANT4 simulation of the NSECT system.

4.2.1.1 Natural Iron Spectroscopic Sample

This sample is created as a 3mm thick disc of natural iron containing the three most abundantly found stable isotopes of iron. The circular disc has a 10 cm diameter with 3 mm thickness, and density of 7874 kg/m³ corresponding to natural iron.

⁵⁴Fe → z=26, a=53.93 g/mole, abundance = 5.8%

⁵⁶Fe → z=26, a=55.93 g/mole, abundance = 91.75%

⁵⁷Fe → z=26, a=56.93 g/mole, abundance = 2.45%

This iron disc is placed in the world and is surrounded by air.

4.2.1.2 Composite Mixture Spectroscopic Sample

This composite sample contains 6 elements in preset concentrations and is based on a corresponding physical sample scanned in laboratory experiments. The sample contains an aqueous solution of 5g Fe, 2.5g NaCl and 2.5g KCl in 40g water inside a cylinder measuring 5 cm in diameter with 2.55 cm height to give a volume of 50 cm³. The composite material in the cylinder has a density of 1 g/cm³ which corresponds to that of water. When filled with this material, the 50 cm³ cylinder contains 50g of the mixture, which is identical to the quantity used in the laboratory experiment.

The six elements in the composite mixture are designed as show below:

$^1\text{H} \rightarrow z=1, a= 1.01 \text{ g/mole, percent mass} = 8.4\%$

$^{16}\text{O} \rightarrow z=8, a= 16.00 \text{ g/mole, percent mass} = 67\%$

$^{23}\text{Na} \rightarrow z=20, a= 40.08 \text{ g/mole, percent mass} = 1.98\%$

$^{56}\text{Fe} \rightarrow z=26, a=55.93 \text{ g/mole, percent mass} = 10\%$

$^{35}\text{Cl} \rightarrow z=17, a=35.45 \text{ g/mole, percent mass} = 5\%$

$^{39}\text{K} \rightarrow z=19, a=39.10 \text{ g/mole, percent mass} = 2.62\%$

This cylindrical sample is placed in the world and is surrounded by air.

4.2.1.3 Composite Iron-Copper Tomographic Sample

This sample is based on an experimental tomographic acquisition sample which contains two bars of natural iron and two bars of natural copper arranged in the shape of the letter 'N'.

Figure 3a shows the physical sample along with its corresponding GEANT4 simulation in figure 3b. The iron and copper bars are aligned together in the shape of the letter "N". Each bar measures 6 mm in thickness, 60 mm in height and 24 mm in depth. The outer vertical bars are made of copper while the diagonal inner bars are made of iron. The simulated sample is designed by defining 4 rectangular bars with identical dimensions, and filling each bar with either iron or copper material with the most abundant stable isotopes for each element as detailed below.

Natural Iron: density 7874 kg/m³

⁵⁴Fe → z=26, a=53.93 g/mole, abundance = 5.8%

⁵⁶Fe → z=26, a=55.93 g/mole, abundance = 91.75%

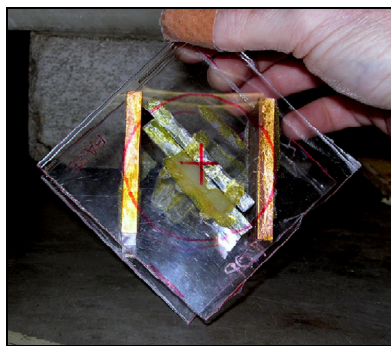
⁵⁷Fe → z=26, a=56.93 g/mole, abundance = 2.45%

Natural Copper: density 8920 kg/m³

⁶³Cu → z=29, a=62.93 g/mole, abundance = 69.17%

⁶⁵Cu → z=29, a=64.93 g/mole, abundance = 30.83%

The alignment of the bars in the simulated sample is achieved by integrating each individual bar with the tomographic gantry at the respective position. All gantry movements are automatically transferred to the each bar of the sample, effectively rotating the sample as a single unit. The sample and gantry are placed in the world and surrounded by air.



(a) Physical Sample



(b) Simulated Sample

Figure 3. Composite iron-copper tomographic sample. The sample is made up of copper (outer, vertical bars) and iron (inner, diagonal bars) arranged like the letter N. Each bar measures 6mm in thickness, 60mm in height and 24mm in depth.

For this sample, the gantry is initialized to provide 88 projections divided into 11 spatial positions at 7 mm intervals, and 8 angles at 22.5 degree intervals from 0 – 180 degrees. This acquisition geometry is identical to that used during experimental acquisition of the physical sample.

Figure 4a and 4b show two views of the simulated system with the GEANT4 world, composite iron-copper sample, and six gamma detectors. The world is shown as a black box with six cylindrical gamma detectors shown in green. The gantry containing the N-sample is an invisible box placed around the sample. Figure 4a shows the sample in initial position while figure 4b shows the same sample with 1 rotation of 22.5 degrees.

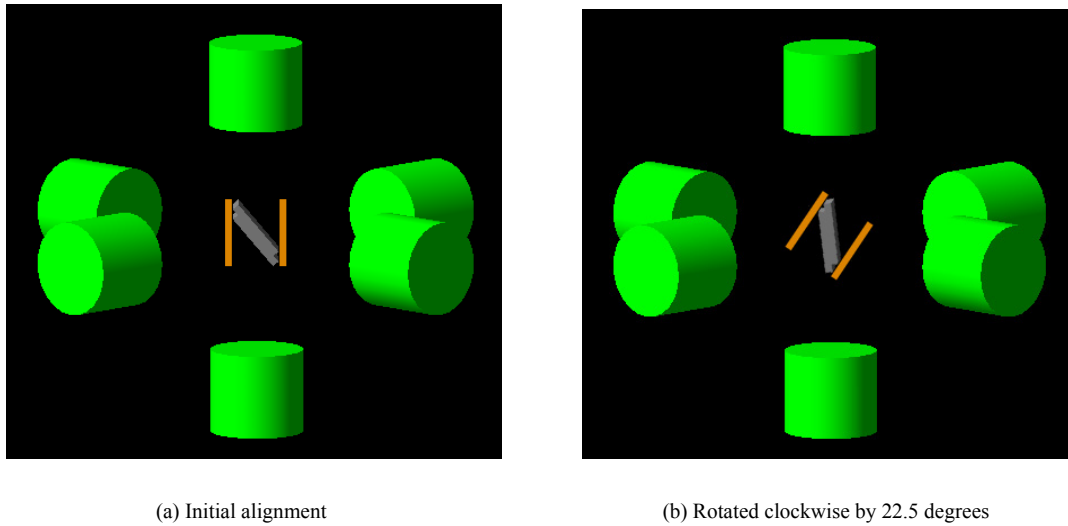


Figure 4. GEANT4 simulation of the iron-copper sample system used for tomographic acquisition showing the sample at different stages of rotation. The bars are aligned together through a tomographic gantry, which is an invisible box placed around the sample. The six green cylinders correspond to gamma detectors.

4.2.2 Iron Overload Sample for Spectroscopic Analysis

This sample is designed as a slice of the human torso containing a section of the liver based on the abdominal CT scan shown in figure 5. The torso is designed as an elliptical tube with a 30 cm major axis, 25 cm minor axis, and 11 cm height, and is filled with water to simulate the elastic scattering properties of the human body. The liver in this spectroscopic sample is modeled as an approximation of the liver in the abdominal CT scan in figure 5, as an elliptical tube with 20 cm major axis and 10 cm minor axis. While the dimensions of the abdomen in this CT scan are not known exactly, 30 cm is used as an approximate length for the major axis of a torso, and all other dimensions are scaled down using the length of the major axis as a standard.



Figure 5. Abdominal CT scan showing the anatomy and location of the liver with respect to the abdomen. The simulated iron overload sample is modeled as an approximation of this abdomen [Source: http://netmedicine.com/xray/ctscan/img_ct/ctal11a.jpg].

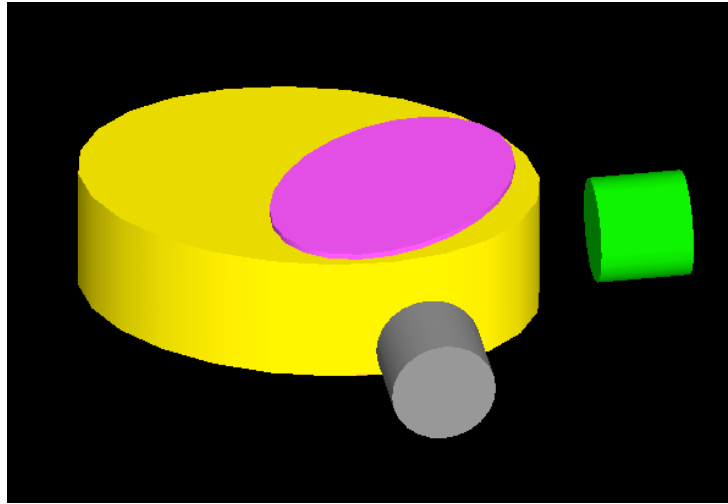


Figure 6. Liver iron overload sample for sensitivity analysis. The torso slice is shown as a yellow elliptical tube, the liver is shown as a pink elliptical tube, and gamma detectors are shown as green and grey cylinders.

The height of the liver is set to 9 cm to give a total volume of 1413.7 cm³. The liver chamber is filled with a uniform concentration of composite liver tissue whose composition is derived from ICRU Report 46 as shown in table 1 [44]. Iron overload is modeled by increasing the percentage of iron in the tissue composition from 0.0 mg/g corresponding to normal liver to 10 mg/g corresponding to extreme iron overload (twice the value of clinically reported concentration in patients). This upper limit is set higher than the clinical upper limit in order to investigate NSECT's diagnostic ability in the presence of severely high concentrations of iron, where MRI is known to suffer from reduced sensitivity.

Element	O	C	H	N	P	S	K	Cl	Na	Fe	Density
Normal (%)	71.6	13.9	10.2	3.0	0.3	0.3	0.3	0.2	0.2	0.0	1060 kg/m ³

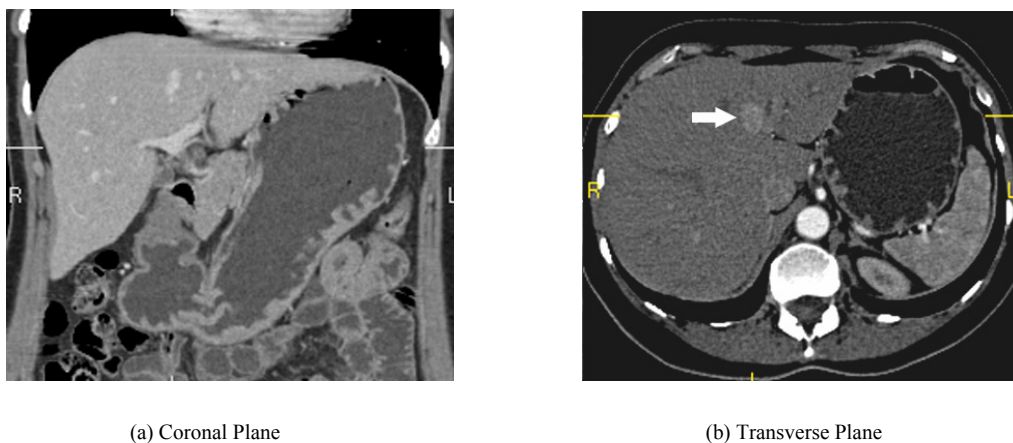
Table 1. Elemental composition of the liver sample (obtained from ICRU report 46).

4.2.3 Torso Iron Overload Sample for Tomography

This sample is a GEANT4 model of a human torso containing a liver with a non-uniform distribution of iron overload. This non-uniform iron overload is created in the form of two high-concentration 'lesions' of iron placed in an otherwise uniformly distributed iron overload. The sample is created in 4 parts – the torso, liver, uniform distribution of iron overload, and high concentration lesions. As this is a tomography sample, it is integrated with the tomographic gantry, which provides spatial and angular translations in user-defined steps.

The torso is modeled in a manner similar to the spectroscopy torso sample above as an elliptical tube with a 40 cm major axis, 30 cm minor axis, and 20 cm height, based on approximate dimensions for a human being. The torso is filled with water to simulate the elastic scattering properties of the human body.

The general shape and dimension of the liver are modeled from abdominal CT scans shown in figure 7.



(a) Coronal Plane
(b) Transverse Plane
Figure 7. Abdominal CT scan in the coronal and transverse planes showing the position of the liver in the abdomen.

Figure 8 show three views of the corresponding simulated liver. The liver is modeled as a combination of 2 objects, a half cylinder coupled with a polyhedron. The dimensions of the liver are determined by defining the major axis of the torso in the abdominal CT scans to be 40 cm and scaling approximate values for the remaining dimensions to the major axis. Using this technique, the dimensions of the liver are set to the following: The half cylinder measures 26 cm in diameter, which forms the major axis of the liver. The polyhedron measures 12 cm in length, which makes the minor axis of the liver 25 cm. Both, the half-cylinder and the polyhedron, measure 12 cm in height, which effectively becomes the height of the liver.

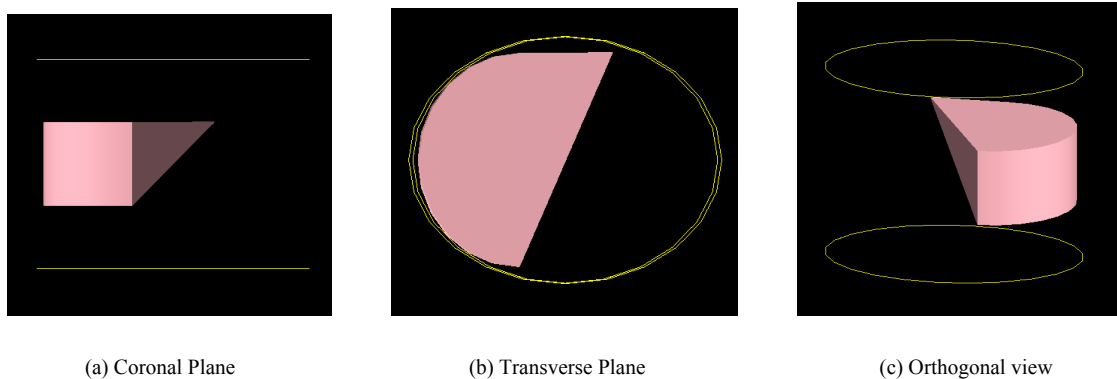


Figure 8. Simulated liver chamber of the tomographic torso sample. The liver is designed as a combination of a half cylinder and a polyhedron. 3 views of the liver can be seen here – coronal, transverse and orthogonal.

The liver chamber is filled with a uniform distribution of the simulated composite human liver tissue obtained from ICRU Report 46 (table 1). Iron overload is simulated by increasing the concentration of iron in the liver from 0.0 mg/g (normal) to 5.0 mg/g (severe iron overload). This value selected for severe iron overload is a

clinically relevant value within the limits corresponding to clinical iron overload, as shown in table 2.

Diagnosis	Liver iron (mg/g dry wt)	Liver iron (mg/g wet wt) (dry/wet = 3.3)
Normal	0.3 – 1.4	0.09 – 0.42
Alcoholic liver disease	0.3 – 2	0.09 – 0.60
Heterozygotes	0.3 – 3	0.09 – 0.90
Homozygotes with early symptomatic hemochromatosis	2.0 – 4.0	0.60 – 1.20
Symptomatic Hemochromatosis	6.0 – 18.0	1.80 – 5.45

Table 2. Representative iron values in normal subjects, patients with hemochromatosis, and patients with alcoholic liver disease (from Harrison's Principles of Internal Medicine – Hemochromatosis [11])

A non-uniform distribution of iron is modeled by creating two high-concentration 'lesions', each with a higher concentration of iron than the surrounding liver tissue. Each lesion is designed as a spherical region of 3 cm diameter, placed with its center in the plane of the neutron beam at locations shown in fig 9. Except for higher iron content, both lesions have identical tissue composition as the rest of the liver. Lesion 1 is given an iron concentration of 10 mg/g, while lesion 2 is given a concentration of 20 mg/g. The surrounding liver tissue contains a uniform iron concentration of 5 mg/g.

These values of iron concentration in different regions of the liver are based on preliminary experiments and sensitivity analysis simulations which suggest that NSECT should be able to detect iron concentrations above 5 mg/g. As it is not known what concentration difference can be detected through tomographic scanning, concentrations of 10 mg/g and 20 mg/g have been chosen as starting points for tomographic acquisition. If these lesions are detected with sufficient accuracy, then a second disease model with

lower iron concentration limits described in table 2 will be scanned to optimize the system with a model that is clinically relevant.

The spinal cord is modeled as a cylindrical tube with outer diameter 5 cm and inner diameter 1 cm. The material of the spinal cord is defined as skeletal bone, based on tissue composition obtained from ICRU Report 46 [44].

Element	O	Ca	C	P	N	H	S	Mg	Na	Fe	Density
Normal (%)	43.5	22.5	15.5	10.3	4.2	3.4	0.3	0.2	0.1	0.000	1920 kg/m ³

Table 3. Elemental composition of human skeletal bone (obtained from ICRU report 46).

The spinal cord serves two functions in this simulation:

- a) It presents a dense anatomic structure that acts as a neutron attenuator in certain projections.
- b) It realistically models the anatomy of the torso and provides a point for visual orientation of the reconstructed image.

Figure 9 shows the complete GEANT4 simulation of the torso, iron overloaded liver, high-concentration lesions, and the spinal cord.

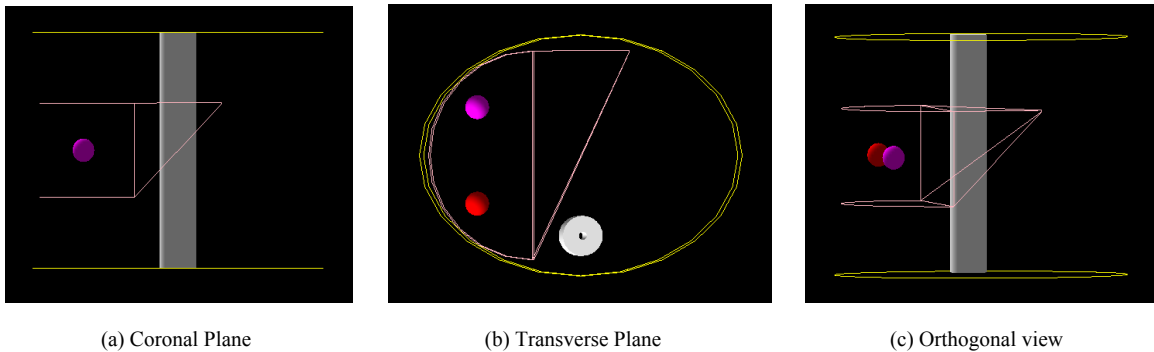


Figure 9. GEANT4 simulation of the torso tomography sample. The outline of the torso is marked by the yellow lines. The liver is shown as a pink outline with two high concentration spherical lesions inside. The spine is visible as a white cylindrical tube.

For this sample, the tomographic gantry is initialized to provide 1248 projections divided into 52 spatial positions at 5 mm intervals, and 24 angles at 7.5 degree intervals from 0 – 180 degrees.

This model of the torso and liver is integrated with the tomographic gantry, which is placed in the world surrounded by air.

4.3 Physics Lists

The GEANT4 library contains a wide variety of particle physics interactions for a host of particles at energies ranging from a few eV to several GeV. In order for an interaction to be included in a simulation model, it must be selected from the library and included in a list that is accessible to the simulated model. While adding every possible physics interaction will to a simulation will model a real world scenario more accurately, it will simultaneously slow down the overall model tremendously. GEANT4 processes each particle as an individual event on a per-event basis. As a particle is incident on another particle in its path, GEANT4 decides the interaction between them in the following manner. The list of possible physics interactions for the two particles in their respective energy ranges are picked from the library, and a probability for each interaction is calculated. A random number generator is used to select the interaction that occurs between these two particles. Each daughter product of the interaction is then treated as an individual particle that travels through the sample medium until it

interacts with another particle in its path. This process is repeated for all the particles specified as long as they are within the world.

Therefore, at every step of the Monte-Carlo interaction, GEANT4 will have to consider each physics list when selecting the particle interaction at that step, even if that interaction cannot realistically occur at that neutron energy. To avoid this scenario, only the interactions observed for particles at our energies of interest have been included in the simulation model. NSECT typically uses a neutron beam with energy between 2 MeV and 8 MeV. Therefore, only the following interactions, which are expected to occur at these energies and contribute to either signal or noise, are included in the simulation.

- Interactions contributing to signal: Neutron inelastic scatter, Neutron elastic scatter, Gamma Compton scatter
- Interactions contributing to noise: Neutron elastic scatter, Neutron capture, Low Energy Rayleigh scattering, Low Energy Photo-electric effect, Low Energy Ionization, Low Energy Bremsstrahlung, Annihilation.
- Particles relevant to this simulation: Neutrons, gamma photons, e^+ , e^- .

There are a few other particles such as anti-neutrinos which also need to be included in the simulation to ensure error-free execution of the code. While the occurrence of these particles is extremely rare (1 occurrence in 10 million events), it is sufficient to cause the simulation to crash if it is not included in the particle list.

After completion of the Monte-Carlo simulation design of the NSECT system, the next logical step is to evaluate the performance of the simulation and verify its accuracy against physical experimental data. The following chapter describes experiments for system evaluation and sensitivity analysis.

5. NSECT System Evaluation for Spectroscopy

The next step after designing the simulation of the NSECT system is to test its validity and efficacy compared to the real world. While a simulation provides an excellent method for evaluating the NSECT technique, it is important to first verify that the simulated model is as close to the physical experimental model as possible. This chapter evaluates the validity of the simulation by comparing results from the simulated system and physical experiments for the three non-tissue samples described in section 4.3.1. After the developed simulation environment is successfully validated, the simulation will be used to determine NSECT's sensitivity for the detection of liver iron overload in humans.

Two points must be made clear before describing the analysis of spectra. The first point refers to digit precision used to describe energy levels and gamma lines in the spectra. The following sections and subsequent chapters discuss energy level values for several elements and isotopes. These theoretical values are known accurately to a precision of two significant digits. However, the scripts that are used to create spectra from experimental and simulated raw data perform rounding off of the energy of the detected gamma photon to the nearest integer in order to assign the detected photon to a single energy bin. Therefore, two digit precision has been used to describe theoretical values of energy levels and gamma lines, while integers are used to describe the values in the spectra.

Second, the rounding off of the gamma energies, combined with the slight variation in detected energy for a Compton scattered gamma photon, can lead to a spread in the gamma energy over a few energy channels in the spectrum. To account for this spread, gamma ray counts from energy peaks adjacent to the main gamma line energy are counted and summed for that gamma line. For most elements and isotopes described in this simulation, this spread was consistently found to occur within ± 1 keV on either side of the main gamma line energy. For example, in the simulated spectrum shown in figure 10, the gamma line from ^{56}Fe at 846.77 keV is present as energy peaks at 846 keV and 847 keV.

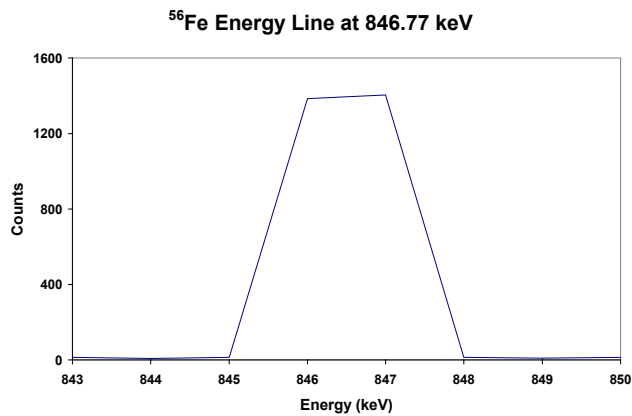


Figure 10. Example of energy spread in gamma line for a ^{56}Fe sample. The original gamma line occurs at 846.77 keV. In the simulated spectrum, this line appears as a peak spread over 846 keV and 847 keV.

Before presenting results from the simulation, it is important to establish a set of rules for evaluating the simulated data. The following section describes the development of tools and techniques to analyze an NSECT spectrum to extract information about the elemental make-up of the sample.

5.1 Spectral Analysis

Spectral analysis in NSECT is performed in 4 steps: background correction, identification of energy peaks, element matching and statistical analysis. The first step corrects the NSECT energy spectrum for sample and detector dependent background counts. The second and third steps identify energies in the spectrum that are significant enough to be classified as peaks and find potential element matches for each of these peaks. Finally, the last step analyzes the statistical significance of each detected peak in the spectrum. Each of these steps is described in the following subsections.

5.1.1 Background Reduction

The first step in spectral analysis is reduction of background counts from the energy spectrum. Background in the simulated NSECT system can be classified into two types: sample dependent background and detector dependent background. Each is reduced using one of two correction techniques. Sample dependent background is reduced through a sample-out subtraction scan while detector dependent background is reduced through a polynomial curve-fit subtraction. Each source of background and its corresponding correction technique are described below.

Sample dependent background originates from tissue samples that contain a large quantity of water. At the energies of operation for NSECT, hydrogen interacts with neutrons through two prominent reactions: elastic scatter and neutron capture. Elastic scatter interactions cause incident neutrons to scatter onto materials in the system

outside of the sample and interact with them to produce non-sample gamma lines. In the physical experimental system, these materials can include hardware components such as the collimator, shielding blocks and sample holders in the experiment area. However, as the simulation contains only the gamma detectors, this elastic scatter background appears as discrete lines in the spectrum at locations corresponding to materials in the detector. Strong energy peaks corresponding to germanium in the HPGe detectors are seen in the spectrum. The second interaction, neutron capture on hydrogen, gives rise to a prominent gamma line at 2224 keV, often seen to be the most dominant energy peak in a spectrum. These two sources of sample dependent background are reduced using a sample-out subtraction technique.

The sample-out subtraction technique is performed in two steps. First, an estimate of the sample correlated background is obtained by substituting the sample with an equivalent mass of water, which contains hydrogen to generate elastic scatter and neutron capture. This estimate of the water-dependent background is then subtracted from the sample-in data to obtain an estimate of the spectrum due to neutron interactions in the sample only.

Estimation of Sample-out Background from Simulated Water Sample

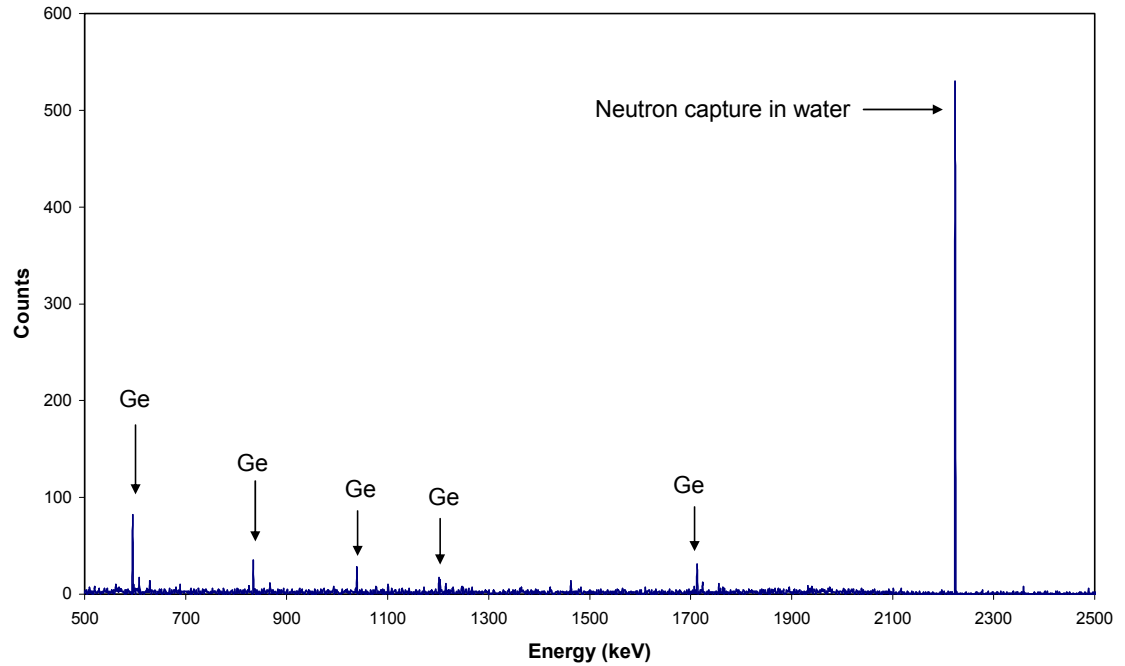


Figure 11. Example of sample-out background from a water sample. Peaks are seen for neutron capture on hydrogen in water at 2224 keV, and for 5 gamma lines from germanium in the HPGe detectors at 595 keV, 834 keV, 1039 keV, 1204 keV and 1713 keV.

Figure 11 and figure 12 show an example of sample out subtraction for an iron sample in water. Figure 11 shows the sample-out spectrum obtained with a water sample in the neutron beam. Figure 12 shows the original spectrum from the iron sample in water along with the sample-out subtracted difference spectrum. The difference spectrum yields a gamma line from ^{56}Fe at 847 keV.

Iron sample: Background Correction

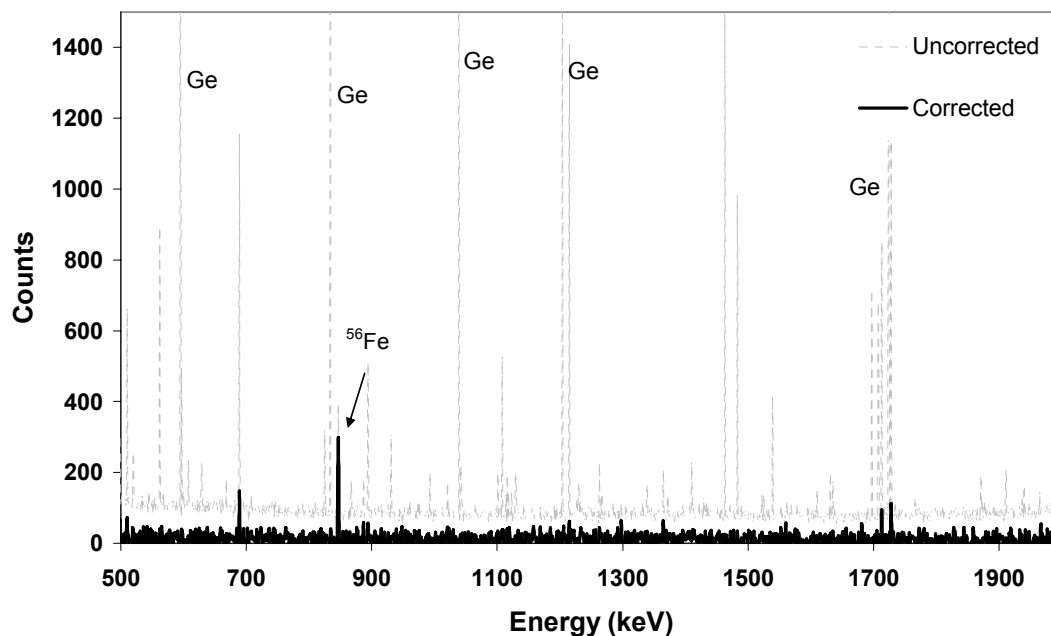


Figure 12. Example of sample-out background correction for iron sample in water. The 5 gamma lines from germanium in the HPGe detectors at 595 keV, 834 keV, 1039 keV, 1204 keV and 1713 keV are significantly reduced.

Detector dependant background appears as a continuous spread over a broad range of energies increasing towards the lower energy region of the spectrum. When high energy gamma rays are incident on a detector, some of the gammas will deposit their full energy in the detector while others may Compton-scatter out of the detector's active volume. This scatter may occur in one or more steps, depositing some energy into the detector at each step. As a result, the energy of the gamma photon may be distributed to the energy channels below it, leading to a compounded effect at lower energy channels. This residual background effect can be reduced using a polynomial

curve-fit subtraction.

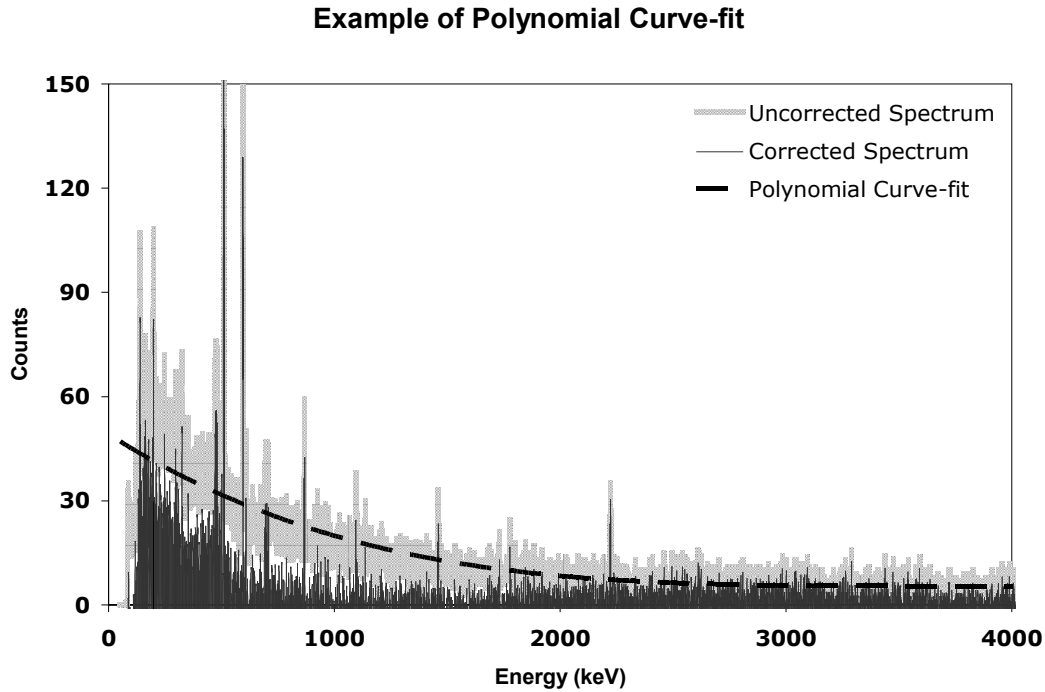


Figure 13. Example of polynomial curve-fitting for residual background correction. The uncorrected spectrum is shown in grey with the polynomial curve overlaid in dotted black. The resulting corrected spectrum is shown in the foreground as a solid black line in the lower part of the image.

The polynomial curve-fit subtraction technique is performed by fitting a fifth degree polynomial curve to model the residual background due to Compton scatter of the detected gammas, and then subtracting this polynomial from the sample-out corrected data. An example of this is shown in figure 13, which shows an original uncorrected spectrum (light gray), the polynomial curve fit to underlying background (dotted black line), and the spectrum after residual background correction (solid black line in the lower part of the image). The resultant image shows a reduced effect from the Compton scattered energy deposited in the lower channels of the detector.

5.1.2 Identification of Energy Peaks

After correcting for sample and detector related backgrounds, each spectrum is analyzed to identify the location of a peak using an automated peak-finding algorithm. The algorithm looks for energy peaks with heights above a specified minimum threshold within a specified energy window, and identifies energy peaks whose p-value is ≤ 0.05 using a z-score test with a Poisson assumption. First, energy peaks with heights above a certain threshold are identified as potential peaks. The threshold is dynamically modeled using a polynomial curve-fit to estimate a pseudo-background in the data due to the following reason. In the HPGe gamma detectors used in NSECT acquisition, the detection efficiency drops off as a function of the energy channel. As a result, the detection efficiency is much worse for higher energy gamma rays than for lower energy gamma rays. Higher energy gamma rays in the spectrum are reported with lower peak values. If peak identification is performed using an absolute threshold value, it may lead to missed identification of a peak at higher energies even though the energy peak may be real and significant. To prevent this missed identification event, the algorithm uses a pseudo background fit which is modeled using a 5th degree polynomial curve fit on the detector data. The threshold for peak identification is determined as a factor of this pseudo-background for each channel of the detector. As the heights of the detected gamma peaks at higher energies decrease, the value of the pseudo-background decreases, thereby decreasing the threshold value for peak identification at higher

energy channels. An example of the dynamic threshold application is shown in figure 14. Figure 14 a shows a sample that is analyzed with the threshold set at an absolute value of 11, leading to several peaks at higher energies not being detected. Figure 14 b shows the same spectrum analyzed with a dynamic threshold set at 5 times the pseudo-background, which is able to detect peaks at higher energy ranges. Peak identification in the lower energy region remains unchanged.

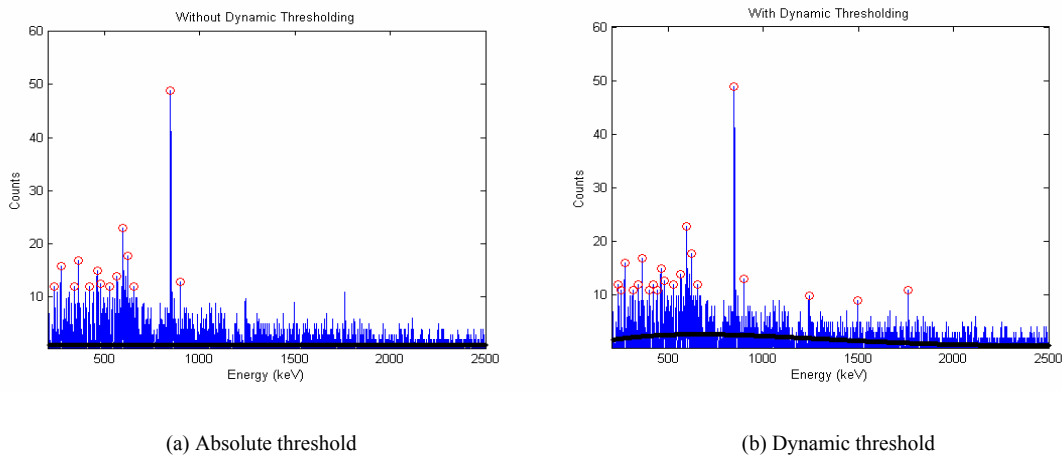


Figure 14. Example of dynamic thresholding for peak identification. Figure (a) shows a spectrum analyzed with an absolute threshold value which excludes peaks at higher energies. Figure (b) shows the same spectrum analyzed with a dynamic threshold set at 5 times the pseudo-background fit. While peaks in the lower energy range remain unaffected, higher energy peaks are now detected clearly.

Each energy detected as a potential peak is then compared to its underlying background using a z-score test for difference of means. Collection of gamma rays in the detectors is assumed to follow Poisson counting statistics, where, for each energy peak, the mean and variance are equal to the number of counts in the peak. With this assumption, the statistical significance for any two energy peaks can be calculated using

the z-score test for a difference of means. Peaks with a two-tailed p-value ≤ 0.05 are considered statistically significant.

An example of the algorithm's operation applied to an iron spectrum is shown in figure 15. The solid blue line shows the original background corrected spectrum. The black line shows the pseudo-background fit used to generate the peak threshold. Energy peaks identified with p-values ≤ 0.05 are denoted by circles. For this spectrum, the peak threshold is set at a factor of 4 higher than the background, and the element detection window width is set at ± 6 keV. These values have been analyzed and optimized through a separate study [45].

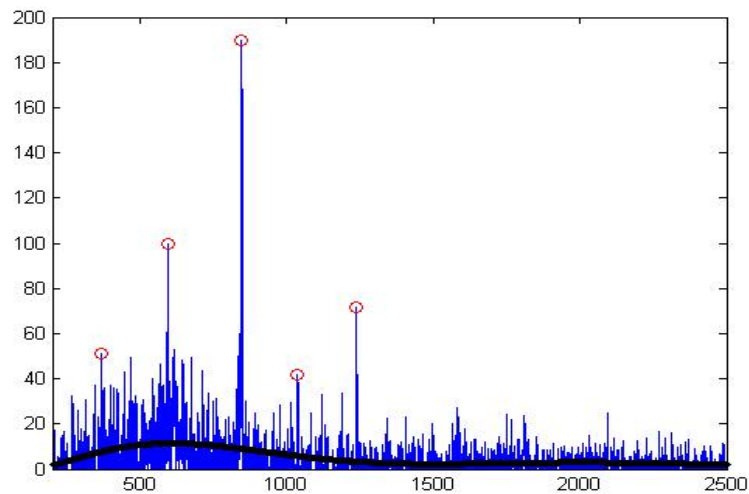


Figure 15. Example of automatic peak finding tool applied to a sample iron spectrum. The blue line shows the background corrected spectrum. The solid black line shows the polynomial curve-fit pseudo-background used for calculating the peak-defining threshold. The red dots show the energies identified as peaks. For this iron spectrum, the identifier shows peaks at 369 and 595 keV corresponding to germanium, and at 846, 1037 and 1238 keV, corresponding to iron.

Each energy identified as a statistically significant peak is passed on to the next step in the analysis process to identify potential element matches.

5.1.3 Element Matching

Element matching for energy peaks reported by the peak-finding algorithm is performed manually using the National Nuclear Data Center's Nuclear Structure & Decay Data online tool (NuDat 2.3) [46]. This identification is made in three steps:

- (a) All elements with gamma lines at the energy peak of interest are listed.
- (b) Isotopes of elements that are not expected to be present in the sample, for example radioactive isotopes or rare stable isotopes with low abundance, are discarded from the list of matches.
- (c) Prior information about the remaining isotopes' line contributions to prominent gamma lines is used to identify a possible element match.

Prior information about gamma line contributions for an isotope comes from experimental and theoretical knowledge of energy level transitions for that isotope. The line contributions of prominent gamma lines have been studied experimentally for several isotopes including ^{12}C , ^{40}Ca , ^{35}Cl , ^{63}Cu , ^{56}Fe and ^{16}O . These experiments have been used to establish the relative ratios of prominent gamma lines for each of these elements. These gamma line ratios are taken into consideration when matching an element with an energy peak. For example, with a 5.0 MeV incident neutron beam, ^{56}Fe is known to have gamma lines generated from energy level transitions at 846.77 keV, 1037.84 keV, 1238.28 keV and 1810.77 keV. Peaks for these 4 energies are expected to be prominent in the resulting spectrum. An experimental spectral acquisition of a solid iron sample is then

used to determine the ratios of these spectral lines relative to each other. For ^{56}Fe , this ratio of is found to be approximately (6):(0.5):(1.6):(0.4). Therefore, a gamma energy peak at 1038 keV in the spectrum can not be attributed to ^{56}Fe unless there is a 10x stronger peak present at 846 keV.

5.1.4 Statistical Analysis

As mentioned earlier, all statistical significance testing of detected energy peaks is performed using the z-score test for difference of means with a Poisson assumption. Energy peaks that are matched with elements have already been tested in the peak-identification process. In this step, energy peaks from two different spectra are tested to determine whether their variation between the two spectra is statistically significant. This comparison is used to determine the diagnostic significance of a peak between two spectra, for example, normal liver and iron overloaded liver. Consider the spectra shown in figures 16a and 16b below, which correspond to a normal tissue sample and disease tissue sample respectively. In both spectra, peaks A through E are detected above underlying background with a p-value ≤ 0.05 . While the heights of peaks A, B, D and E are unchanged in the two spectra, the height of peak C varies from 134 counts in the normal spectrum to 192 counts in the disease spectrum. The statistical significance of the difference for this peak is calculated as follows:

$$z = \frac{\mu_{disease} - \mu_{normal}}{\sqrt{\mu_{disease} + \mu_{normal}}} = (192-134)/(192+134)^{1/2} = 3.21 \rightarrow \text{p-value} \leq 0.05$$

Therefore, peak C is considered to be of diagnostic significance.

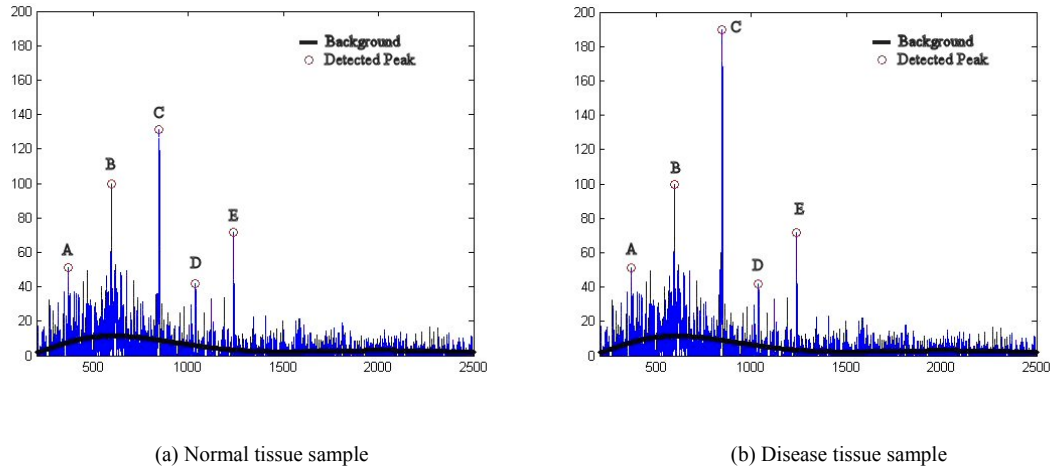


Figure 16. Example of statistical significance testing for two spectra. Peaks detected above the background with a p -value ≤ 0.05 are marked by letters A to E. Peak C is found to have a statistically significant difference between the two spectra.

These spectral analysis tools and techniques have been used to analyze all spectra shown in the following sections.

5.2 Comparison of Simulated and Experimental Spectra

Spectroscopic testing of the NSECT system simulation is performed using the natural iron spectroscopic sample and the composite mixture spectroscopic sample described in sections 4.2.1.1 and 4.2.1.2. Spectra generated from each simulated sample are compared with the corresponding experimental spectrum using two pre-determined criteria for system evaluation:

1. Gamma energy peaks in the simulated spectrum must be observed at energies corresponding to prominent excited state transitions in the target nuclei

2. Locations of peaks in the simulated spectrum must be in agreement with peak locations in the experimental spectrum.

Each simulated spectrum has been analyzed using these two criteria for system evaluation.

The following sections describe the comparison results from these two simulated samples.

5.2.1 Natural Iron Spectroscopic Sample

The natural iron sample designed in Section 4.2.1.1 is scanned using a simulated 7.5 MeV neutron beam with two HPGe gamma detectors. The scanning geometry is identical to that used during the corresponding experimental scan. Fig 17 shows the background corrected normalized spectra from the simulated and experimental scans for this sample. Table 4 shows a summary of the evaluation for this spectrum.

Thin iron sample: Simulated vs Experimental Spectrum

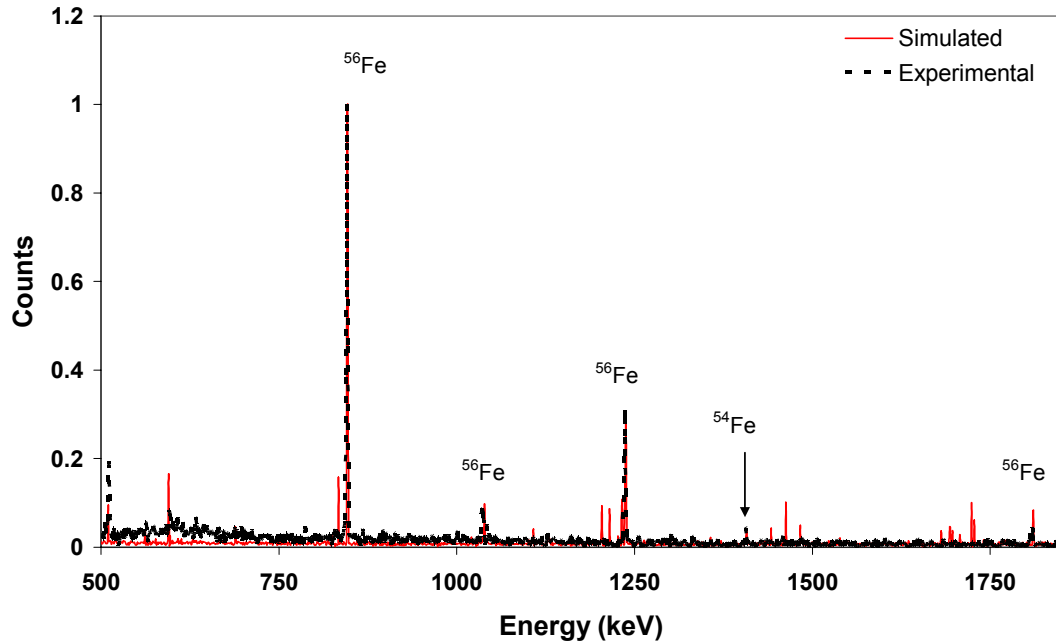


Figure 17. Comparison of simulated and experimental gamma spectra for a natural iron sample in air. The simulated spectrum is shown as a solid red line, while the experimental spectrum is depicted by an overlaid dotted black line. Energy peaks corresponding to the 4 most prominent excited states in ^{56}Fe can be seen at 847 keV, 1039 keV, 1238 keV and 1811 keV.

Element	Energy (keV)	Simulated counts (Normalized)	Experimental counts (Normalized)	Difference (%)
^{56}Fe	847 keV	1.000	1.000	0.00%
^{56}Fe	1039 keV	0.098	0.088	11.61%
^{56}Fe	1238 keV	0.281	0.309	9.15%
^{56}Fe	1811 keV	0.083	0.045	83.33% (4.50%)

Table 4. Analysis of the simulated and experimental gamma spectra for the natural iron sample. Peaks for 4 excited states in ^{56}Fe are seen in both spectra. The large percent difference in the peak at 1811 keV can be attributed to the decrease in energy efficiency of the HPGe detector at higher energies. When corrected for this efficiency decrease, the percent difference reduces to 4.5% (shown in brackets).

Gamma energy peaks are seen for each of the 4 prominent excited states expected at this neutron energy: 847 keV, 1039 keV, 1238 keV and 1811 keV. The

locations and heights of gamma energy peaks in both spectra are in general agreement with each other. All energy peaks except the peak at 1811 keV are within 15% of the corresponding peak heights in the experimental spectrum. The discrepancy in the 1811 keV peak can be attributed to the decrease in efficiency of the physical gamma detector at higher energies. This decrease in efficiency varies with the geometry used during acquisition and can be different for each detector crystal. This efficiency can be estimated with Monte-Carlo simulations based on calibration measurements made at different energies for each detector crystal. These simulations take into account the manufacturer specified detector efficiency, user-determined detector efficiency obtained through calibration scans performed over a wide range of energies, and the geometry of acquisition. An example of this decrease in efficiency for the HPGe detectors used in the experimental scans is shown in figure 18. From this detector efficiency curve, it can be seen that the detector efficiency at 847 keV is 5×10^{-4} while the efficiency at 1800 keV drops to about 2.6×10^{-4} . This decrease of a factor of 1.92 is able to account for the variation in the height of the peak at 1811 keV. When corrected for this drop in efficiency, the difference between the counts in the simulated and experimental spectra reduces to 4.5%.

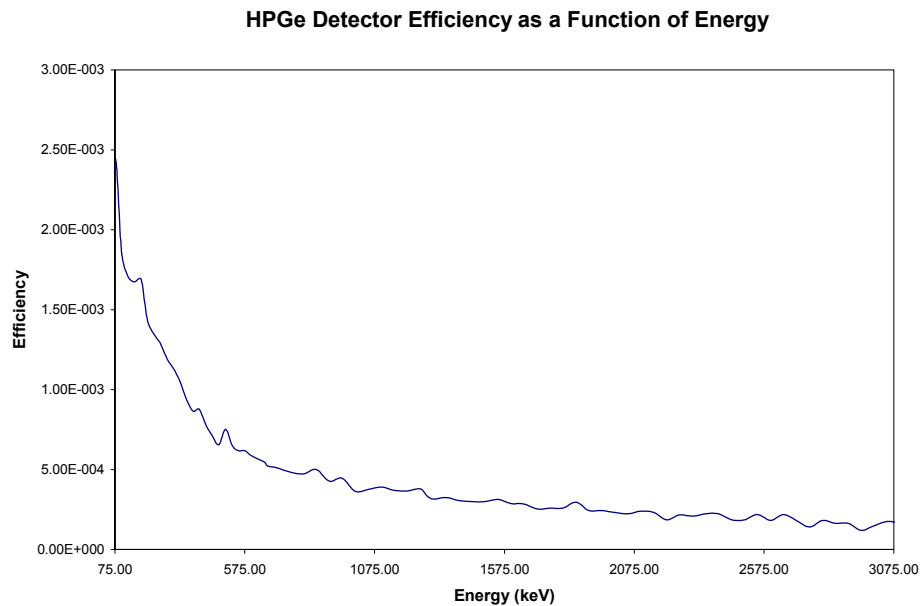


Figure 18. Example of energy dependent detector efficiency. The efficiency is calculated through a Monte-Carlo simulation that takes into account the manufacturer specified detector efficiency, calibrated detector efficiency, and the geometry of acquisition (courtesy Anthony Hutcheson, TUNL and Dept. of Physics, Duke University).

5.2.2 Composite Mixture Spectroscopic Sample

The composite mixture sample described in section 4.2.1.2 is scanned with a simulated 6.0 MeV neutron beam with two HPGe gamma detectors. Figure 19 shows the background corrected normalized spectra from the simulated and experimental scans.

Table 5 shows a summary of the evaluation for this spectrum.

Fe + NaCl + KCl solution in water: Simulated vs Experimental Spectrum

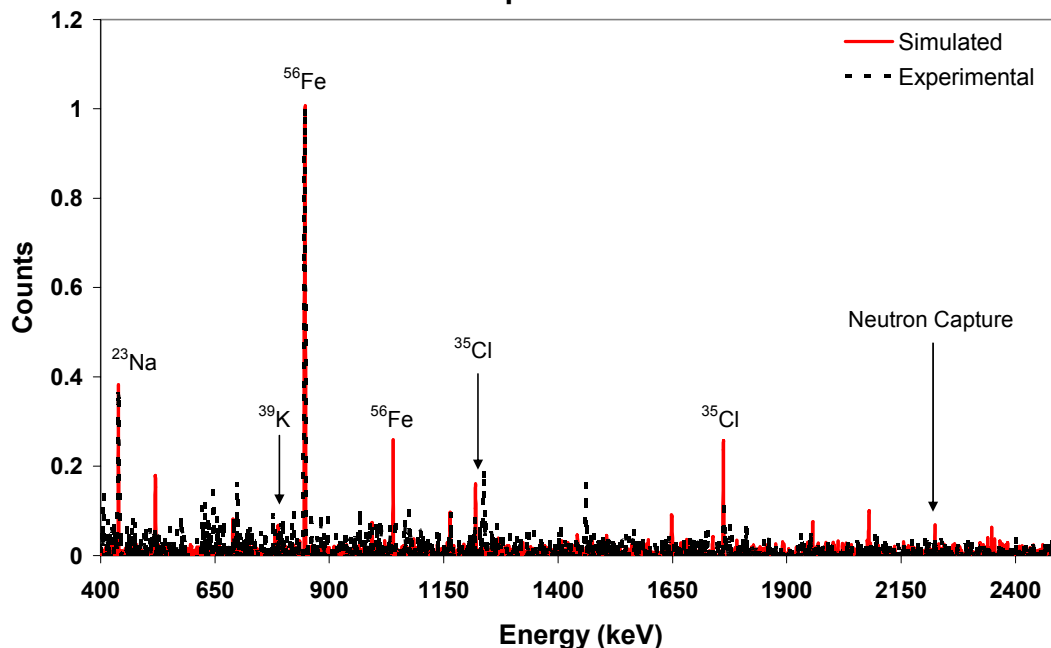


Figure 19. Comparison of simulated and experimental normalized gamma spectra for the Fe, NaCl and KCl composite sample. The simulated spectrum is shown as a solid red line, while the experimental spectrum is depicted by an overlaid dotted black line. Energy peaks corresponding to all 4 elements are seen in the spectra.

Gamma energy peaks are seen for lines from each of the 4 elements listed in the sample. Peaks are seen for ^{23}Na at 440 keV, ^{39}K at 782 keV, ^{56}Fe at 847 keV and ^{35}Cl at 1220 and 1761 keV. Except for the peak from ^{39}K at 782 keV, the locations and heights of all other gamma energy peaks in both spectra are in general agreement with each other. The heights of these peaks are observed to be within 15% of the corresponding peak heights from the experimental spectrum. While the two peaks from ^{35}Cl initially appear larger in the simulated spectrum, the difference drops to approximately 10% for both after correction for detector efficiency.

Element	Energy (keV)	Simulated counts (Normalized)	Experimental counts (Normalized)	Difference (%)	Efficiency Corrected
²³ Na	440 keV	0.382	0.365	4.76%	4.76%
³⁹ K	782 keV	0.044	0.058	24.42%	24.42%
⁵⁶ Fe	847 keV	1.000	1.000	0.00%	0.00%
³⁵ Cl	1220 keV	0.106	0.086	23.53%	9.56%
³⁵ Cl	1761 keV	0.255	0.111	129.56%	10.69%

Table 5. Analysis of the simulated and experimental gamma spectra for the Fe, NaCl and KCl composite sample. Peaks for all 4 elements are seen in both spectra. The large percent difference in the peaks at 1220 keV and 1811 keV can be attributed to the decrease in energy efficiency of the HPGe detector at higher energies. When corrected for this efficiency decrease, the percent difference reduces to less than 15% for both.

This sample contains a significant quantity of water, which gives rise to the 2224 keV gamma line from neutron capture. While the uncorrected heights of the neutron capture peak in the simulated spectrum was different from the experimental result, both peaks were reduced in the sample-out subtraction.

The data shown in table 5 is efficiency corrected for some energy peaks and not due to the sparseness of the detector efficiency data which comes from a Monte-Carlo simulation in MCNP. The detection efficiency curve shown in figure 18 is not an exact plot for this acquisition setup, but instead, an approximation based on a general acquisition geometry.

The large percentage difference in the ³⁹K peak at 782 keV is most likely due to poor statistics in detection for the peak arising from a combination of a relatively low cross section and low concentration in the sample. ³⁹K shows a lower neutron inelastic cross section (0.29 barns at 5 MeV) compared to ⁵⁶Fe (1.40 barns at 5 MeV) [47].

This analysis demonstrates the validity of the NSECT system simulation for spectroscopy of single element samples as well as composite mixture samples. Analysis for the tomography system has been described in a later section.

The validated spectroscopy system can now be used to determine the sensitivity of the NSECT technique for spectroscopic detection of iron overload in humans.

5.3 *Iron Overload Sensitivity Analysis*

After verifying the working of the GEANT4 simulation of NSECT, it is important to determine whether the NSECT technique in its current form has the ability to diagnose a clinically relevant concentration of iron in the human body. Liver iron concentrations in patients have been commonly reported to range from 1.5 mg/g in relatively milder cases of iron overload to 6 mg/g in severe cases [9-11, 34]. In rare cases, concentrations have been reported to be as high as 9 mg/g [48]. While both MRI and CT have the ability to diagnose elevated iron concentrations at clinically relevant values, their effective detection ability is limited to a narrow concentration range that occupies a small window between 1 mg/g and 6 mg/g which does not cover this entire range. For NSECT to develop into a clinically applicable diagnostic technique, it is important to determine whether it has the potential to show any improvements over other existing non-invasive techniques. In the performance validation of the NSECT simulation, the samples used have been non-tissue samples with only a few elements and a small quantity of water. In clinical scenarios where scanning must be performed on patients,

the significant addition of elastic scatter noise from hydrogen in the human torso will substantially change the noise estimate for the NSECT system. An estimate of the increase scatter background must be obtained to facilitate investigation of NSECT's ability to diagnose iron overload in a clinical scenario. The experiment described here aims to determine whether the minimum concentration of iron that can be detected in the presence of elevated torso noise lies within the range of clinical iron overload.

Sensitivity analysis is performed using spectroscopic interrogation of the human torso sample described in section 4.2.2. This sample models a uniform distribution of iron overload which can be varied in steps to simulate degrees of iron overload. Four liver samples are created by varying the concentration of iron from 1 mg/g to 10 mg/g in discrete steps. The lowest value of 1 mg/g corresponds to a normal iron concentration in the liver. The second value of 3 mg/g represents a value in the middle of the iron concentration range for overload, while the third value 5 mg/g is closer to the upper limit. The fourth value of 10 mg/g selected to assess the performance of the NSECT system in the presence of extreme concentrations of iron, for example in a scenario where iron is distributed non-uniformly and the spectroscopic scan focuses on a region with severely high iron concentration.

The remaining elements in the liver tissue in each sample are kept relatively constant, with only minor variations in concentrations of ^{14}N , ^{31}P , ^{32}S and ^{39}K to maintain

arithmetic consistency in the sample as the concentration of iron in the tissue is increased.

Although tomography is the final goal for NSECT, a spectroscopic examination is used here as a first step towards tomographic analysis. Unless iron overload detection is successful using simple spectroscopy for a uniform distribution of iron overload, it is unlikely to be successful in tomographic analysis where the total number of incident neutrons will be distributed over a larger number of projections, effectively reducing the statistical accuracy at each projection. If spectroscopic detection is found to be feasible at clinically relevant concentrations of iron, then the simulation can be easily expanded to a tomographic acquisition setup.

To determine the accuracy of spectroscopic iron overload measurement in the liver, a calibration sample with an iron concentration of 25 mg/g is used to establish a ratio of iron concentration to gamma counts. The experimentally established ratio is then used to determine a measured value of iron concentration for each liver sample. In order to maintain the geometric accuracy of the sample, the calibration sample used here is the same human torso sample with a uniform liver iron concentration of 25 mg/g.

Each liver sample is scanned 10 times with 800,000 neutrons through spectroscopic acquisition to generate a super data set of 8 million neutron events per sample. A different random seed is used for each simulation in order to ensure that the simulations are not correlated. The super data set is used to generate additional data sets

for 4 different values of incident neutron counts: 1 million, 0.75 million, 0.5 million and 0.25 million. This is done by randomizing the complete data set with 8 million counts and then sampling the required number of neutron counts from the randomized data set. For example, to generate a data set with 1 million counts, the super data set is first randomized, and the first 1 million counts are selected for the new parsed data set. At most 2 non-overlapping samples are parsed from each randomized data set to ensure minimal overlap in the data. This process is used to generate a data set of 10 acquisitions for each sample with 4 different values of neutron events, giving a total of 40 acquisitions per sample.

Finally, a water sample is scanned for an equal number of neutron counts to estimate the sample-dependent background that originates from elements other than iron. The water sample spectrum is used to perform background subtraction for each of the liver samples described above. In addition to providing a background noise estimate for sample-dependent background reduction, this spectrum also gives an estimate of the scatter noise generated by the human torso.

Gamma spectra are generated for each sample in the spectroscopy data set and corrected for sample-dependent background noise from the water sample with the sample number of neutron counts. Gamma-ray counts for energies corresponding to iron are identified for each individual sample.

The effect of reducing the number of neutrons on the accuracy of detection is tested through Receiver Operating Characteristic (ROC) analysis for each sample. ROC curves have been widely used in medicine to increase the precision with which medical tests are evaluated [49]. An ROC analysis can be used to compare the detectability of a disease by 2 or more diagnostic tests, by a combination of tests, or by a combination of a test and reader. ROC analysis has also been used to determine optimum criterion levels that maximize accuracy or any other measure of clinical efficacy for a diagnostic imaging modality.

The criterion used to determine the sensitivity of iron overload detection is that the area under the ROC curve (AUC) for acquisition must be greater than a minimum threshold of $A_z = 0.85$. Acquisitions with $A_z < 0.85$ can not be considered diagnostically significant. This threshold value of 0.85 has been selected as a starting point for analysis since NSECT is a new imaging modality and there are no known experiments or standards to provide a validated threshold for such analysis. As the technique continues to evolve and its detection limits are better understood, the threshold for A_z will be adjusted accordingly for future analyses.

Results for the sensitivity determination in the spectroscopy system are described below.

Figure 20 shows the working of the GEANT4 simulation for a spectroscopic scan of the liver. Neutrons are shown in blue, entering the liver from the top right corner of

the image. Each neutron is made incident onto the liver and may interact with liver tissue and torso at one or more points along its path. Scattered particles can be seen exiting the liver and torso chambers. From the inherent geometry of the simulation, some of these particles may be detected in the gamma detectors, while a majority will go undetected. HPGe gamma detectors are shown in grey and green.

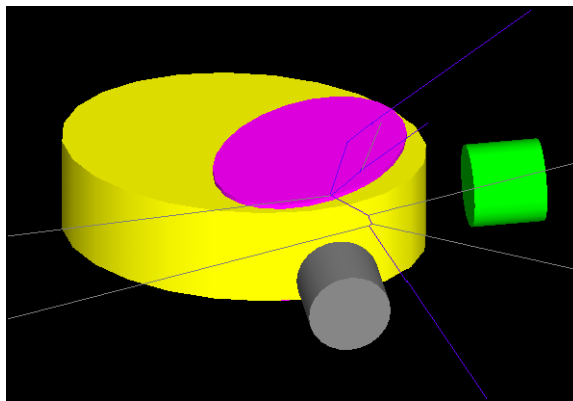


Figure 20. GEANT4 simulation of iron overload spectroscopic analysis. The sample used here is a uniform liver iron overload sample with an elevated concentration of iron. The torso is shown in yellow, liver in pink, and HPGe detectors in green and gray. The liver contains a uniform distribution of iron overload. Incident neutrons are shown in blue and enter from the top right corner of the image. Scattered particles can be seen exiting the sample after multiple scattering events.

Figure 21 shows an estimate of the simulated water background spectrum for this system with 2 million neutron counts. Both sources of sample and detector dependent backgrounds are clearly visible in the spectrum. Peaks from 5 excited states in germanium are visible at 595 keV, 834 keV, 1039 keV, 1204 keV and 1713 keV.

**Simulated Spectrum from Water Sample
2 million neutron events**

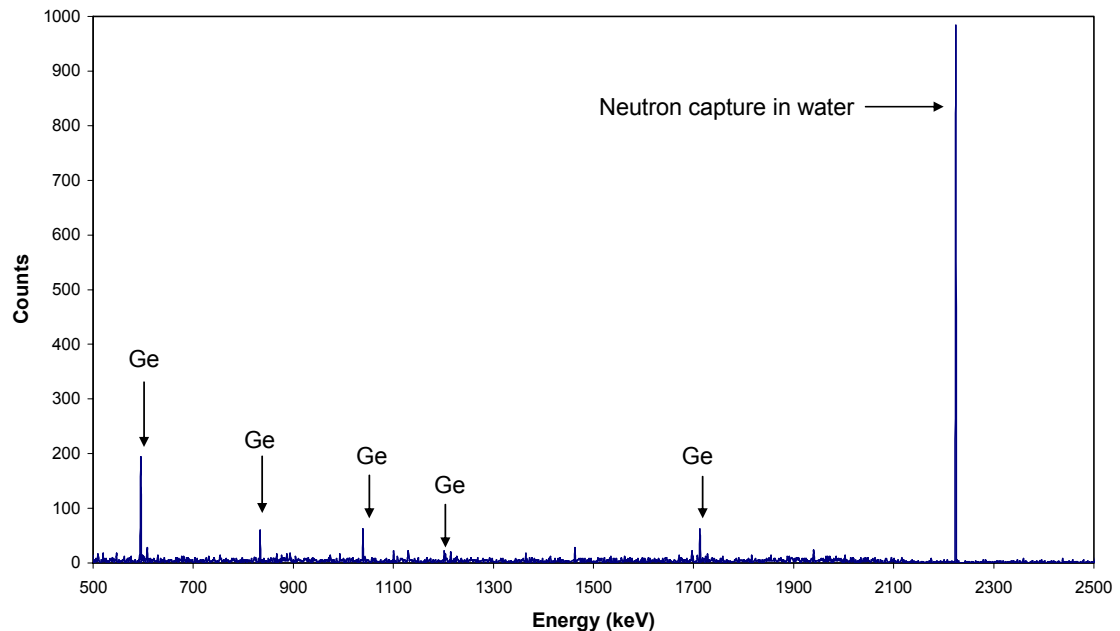


Figure 21. Simulated gamma spectrum from a water sample. This spectrum is used to estimate the scatter background from tissue, which can be used for background correction in liver spectra. Peaks are seen for excited states in germanium and for neutron capture on hydrogen in water.

Three key background effects can be seen in the spectrum from the water sample.

- i. Neutrons scattering elastically with hydrogen scatter onto the gamma detectors. These neutrons undergo inelastic scattering with germanium, which leads to creation of the Ge gamma lines seen in the spectrum.
- ii. The large peak at 2224 keV from neutron capture on hydrogen leads to an increase in residual background over the lower channels of the detector due to Compton scattering of the detected gammas.

- iii. The prominence of elastic scatter interactions leads to reduced detection of nuclei such as carbon, which have their first excited state at the higher end of the spectrum. Elastic scatter reduces the energy of the incident neutrons with each interaction. As a result, fewer neutrons are able to retain their initial incident energy as they pass through the sample. This translates to reduced excitation of nuclei such as carbon (first excited state at 4434 keV), unless the initial incident neutron energy is sufficient to compensate for this loss.

While the first two effects are corrected through sample-out background subtraction, the third effect is somewhat more challenging to correct. It can not be corrected through any background reduction technique. One possible method of correction that can be used is to calculate the loss in detected counts for the high-energy nucleus through a simulation that eliminates elastic scatter, and use this value to correct the gamma spectrum. A similar technique has been described and used for tomographic analysis of the liver sample presented in a later section. At this point however, as the elastic effect is not found to be significant for the energy peak from ^{56}Fe , it has been left uncorrected in this spectroscopy experiment.

Figure 22 shows the simulated spectrum from the calibration sample with an iron concentration of 25 mg/g for 2 million neutron events. The original uncorrected spectrum is shown as a dotted gray line while the background corrected spectrum is shown as a solid black line. As can be seen, the peaks from germanium and the neutron

capture line at 2224 keV reduce significantly after background correction. A slight decrease can be seen in the Compton background over the lower channels of the detector. However, the peak at 847 keV corresponding to ^{56}Fe remains relatively unchanged.

**Simulated Spectrum from Calibration Sample (Fe = 25 mg/g)
(2 million neutron events)**

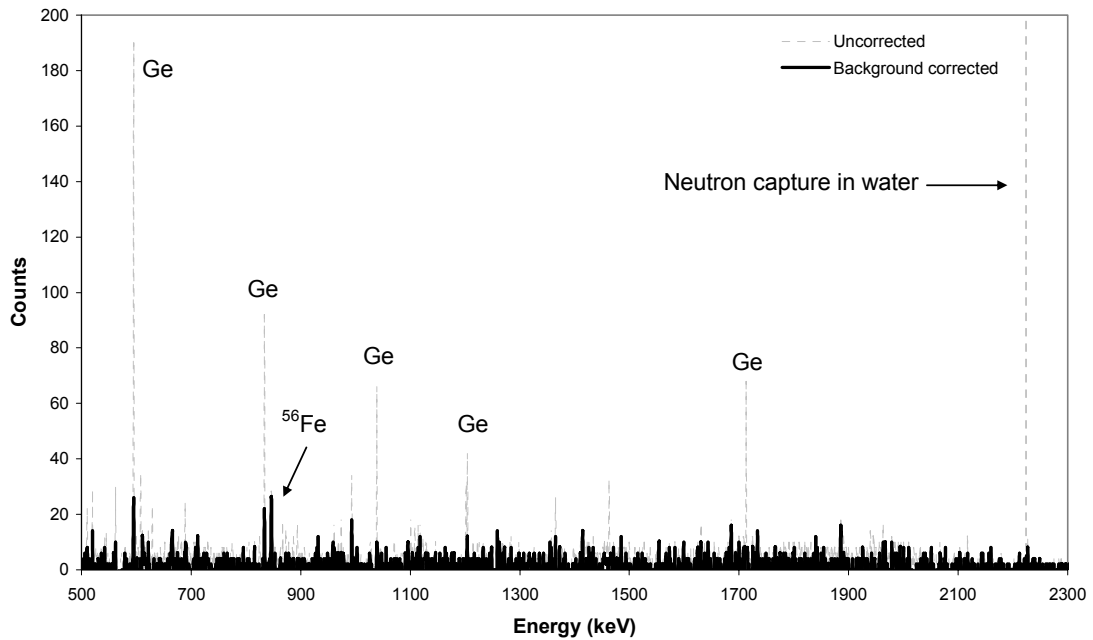


Figure 22. Simulated gamma spectrum from calibration sample (Fe = 25 mg/g) with background correction. The background corrected spectrum is shown as a solid black line while the original uncorrected spectrum appears as a gray dotted line. Peaks for germanium and neutron capture on hydrogen are significantly reduced through sample-out subtraction, while the signal peak from iron at 847 keV remains unchanged.

The background corrected spectrum is analyzed using the z-score test for difference of means, as described earlier. For this spectrum 52 counts are detected in the peak at 846-847 keV over a background of 4 counts. The background is determined through a polynomial curve-fit estimation performed in a manner similar to that

described for polynomial background correction. The p-value is calculated using the z-score test for the difference of the means with a Poisson assumption, which for this spectrum is ≤ 0.001 .

Figure 23 shows a similar spectrum for an iron concentration of 3 mg/g. At this concentration of iron, it is difficult to detect the iron peak above background with sufficient statistical significance. To ensure that the lack of statistical significance in this sample was not due to a limitation in the number of neutron counts used, the spectrum was generated once more for the maximum number of neutron counts, but no significant improvement was observed in the p-value.

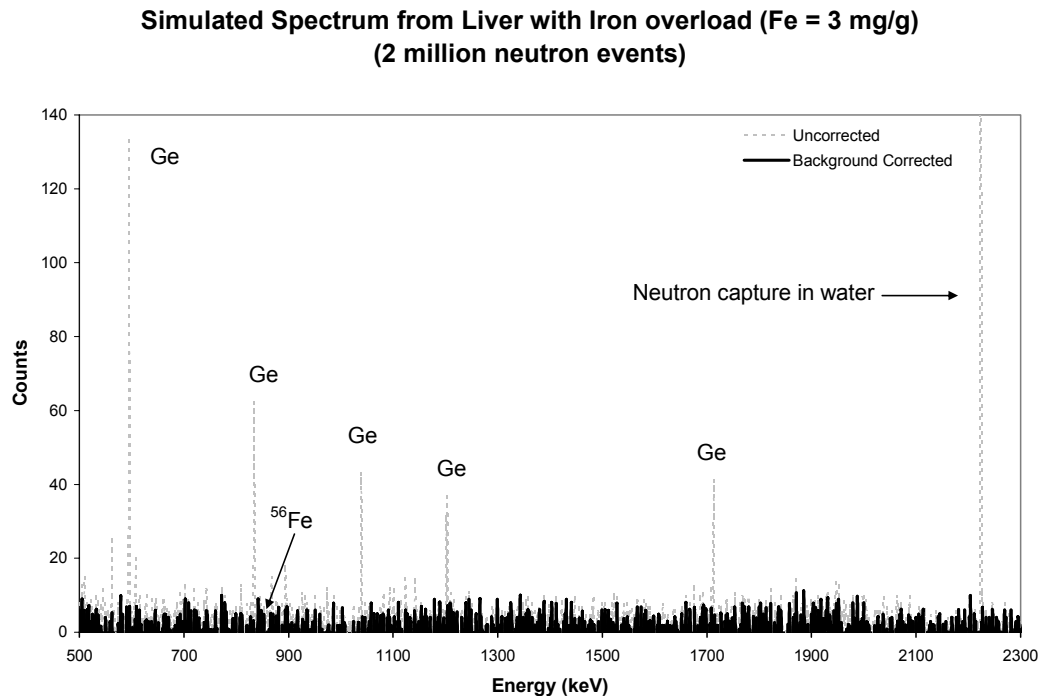


Figure 23. Simulated gamma spectrum from liver with iron overload (Fe =3 mg/g) with background correction. The background corrected spectrum is shown as a solid black line while the original uncorrected spectrum appears as a grey dotted line. In this spectrum, the peak from iron at 847 keV is difficult to identify clearly above the underlying background.

ROC analysis to calculate Az is performed by comparing the counts in the 846 keV peak in the iron overload spectrum against the counts in the 847 keV peak in the corresponding normal liver spectrum for each of the 10 samples in the data set corresponding to the combination of iron concentration and incident neutrons. The spectral counts from the ^{56}Fe peak at 847 keV are fed to the ROC Analysis package LABROC, which calculates the AUC by fitting a binormal curve to the continuously distributed data [50].

Table 6 shows a summary of the result of the ROC analysis for each combination of the sample and number of neutrons used. Values of $Az \geq 0.85$ are seen for several acquisitions of the 5 mg/g and 10 mg/g iron concentration samples. Three of these combinations also give a perfect Az value of 1. The value of Az does not rise above the detection threshold for any number of incident neutrons for the 3 mg/g sample. This is most likely due to the lack of adequate statistical accuracy in detecting the ^{56}Fe peak above the underlying background in the sample. However, the Az values observed for this sample are still decent. Considering their standard errors, the value of Az is still within one standard deviation for 3 of these combinations.

Fe (mg/g)	Incident neutrons (million)			
	1	0.75	0.5	0.25
10.00	1.00	1.00	0.94 ± 0.03	0.90 ± 0.04
5.00	1.00	0.96 ± 0.04	0.91 ± 0.05	0.84 ± 0.04
3.00	0.79 ± 0.09	0.82 ± 0.08	0.74 ± 0.09	0.64 ± 0.10

Table 6. Results of ROC analysis for spectroscopic sensitivity testing. The ROC values for Az and their standard errors are obtained from LABROC software. None of the acquisition geometries are able to detect the 3 mg/g sample with Az > 0.85.

Table 7 shows the accuracy in spectroscopic measurement for each combination with Az ≥ 0.85 from above. As expected, the error of measurement increases with lower concentration of iron in the sample and with fewer incident neutron counts for each acquisition.

Fe original (mg/g)	Incident neutrons (millions)							
	1		0.75		0.5		0.25	
	Fe	Error	Fe	Error	Fe	Error	Fe	Error
10.00	10.42	4.20%	10.60	6.00%	9.10	9.00%	8.40	16.00%
5.00	5.20	4.00%	6.08	21.60%	6.16	23.20%	1.44	71.20%
3.00	5.30	76.67%	5.26	75.33%	5.36	78.67%	4.16	38.67%

Table 7. Accuracy of spectroscopic measurement for the 3 values of incident neutron flux.

Three significant findings can be derived from the analysis results of the spectroscopy simulations. First, the simulation indicates that the spectroscopic detection of iron overload through NSECT can be performed for a concentration of 5 mg/g. This is a clinically relevant value well within the limits reported for iron overload in patients.

Second, the study indicates that for an iron overload of 5 mg/g, NSECT has the potential to perform spectroscopic quantification measurements with a quantification error of less than 15% for 1 million incident neutrons. Dose analysis described in a subsequent chapter determines the dose from this acquisition to be approximately 0.02 mSv, which is significantly lower than the dose received from a standard abdominal x-ray radiography exam. Third, the error in quantitative accuracy increases sharply between the 5 mg/g sample and 3 mg/g samples and appears to be relatively independent of the number of incident neutrons. The lack of correlation between the error and incident neutrons suggests that the concentration of 3 mg/g may lie below the threshold of detection for NSECT and the error in table 7 is purely statistical.

Three important goals have been achieved in this chapter. First, the simulation of the NSECT environment has been tested and validated against experimentally obtained data for a two spectroscopic samples. While there have been several experiments performed until now that have used both single-element and multi-element physical samples, many of these have been proof of concept studies with rudimentary acquisition systems whose primary goal was to understand the experimental challenges of NSECT. In some of these experiments, the signal to noise ratio was too low to detect anything other than dense solid metal samples. The simulation developed here is based on the system currently in use, which has advanced significantly since the early experiments. As a result, it is difficult to test the efficacy of this advanced system simulation with

experimental data acquired using rudimentary systems. The two samples presented here were scanned with an experimental setup that is not very different from the one currently in use at TUNL.

Second, the sensitivity analysis study has shown that accurate detection of iron overload through spectroscopy is possible at a value of 5 mg/g which is clinically relevant value well within the limits reported for iron overload in patients. Further, an increase in iron concentration will directly translate to an increase in the detected signal, which implies that NSECT has the potential to detect very high concentrations of iron in extreme overload cases where MRI suffers from a reduction in quantitative accuracy.

Third, as the sensitivity analysis has shown that iron concentrations below 3 mg/g may not be detected with adequate accuracy, the iron overload in the tomographic sample will be modeled with an iron concentration of at least 5 mg/g.

With these findings, the simulation is ready to be extended to a tomographic model for liver iron overload diagnosis. The tomography experiment and results are described in chapter 6 along with a discussion of the principles of NSECT tomography.

6. NSECT System for Tomography

As mentioned earlier, tomography in NSECT is required in order to investigate non-uniform iron distributions within the liver. The spectroscopy simulation of the NSECT system which has been satisfactorily validated is now expanded to perform tomographic analysis in samples. As with the spectroscopic system, the tomography system must also be validated before proceeding with system optimization to work towards a clinical system for iron overload detection.

This chapter describes the results of validation of the NSECT tomography system simulation, and then uses this simulation to determine the optimal set of scanning parameters for NSECT acquisition. The chapter is organized in 3 sections. The first section presents an overview of tomography in NSECT, the second describes the experiment for system validation, and the third describes results from the tomographic simulation of the iron overload sample.

6.1 Tomography in NSECT

As with all other tomographic imaging systems, NSECT performs tomography by acquiring a complete set of projections of line integrals through the sample. For NECT, these projections are defined by the angular and spatial sampling intervals between successive positions of the sample. While ideal tomography systems would acquire projections between 0 to 360 degrees, due to limitations in acquisition time and

concerns about patient dose, the current NSECT tomography system scans the sample from 0 to 180 degrees. The following sections describe the tomographic acquisition geometries and reconstruction algorithms currently used in the NSECT tomography system.

6.1.1 Acquisition Geometry

NSECT tomography is currently performed using the translate-rotate configuration similar to first generation CT scanners, by translating the beam horizontally through the entire sample length, then rotating the beam through a fixed angle and repeating the process. While most modern tomography systems are able to use multi-element detector grids, NSECT is limited to a single element detector, which provides virtually no spatial information. Therefore, the burden of extracting spatial information is transferred to the beam. In the current experimental implementation, the neutron beam is created by a nuclear accelerator source which cannot be moved. Therefore, with this single detector, single fixed-beam geometry, the translate-rotate geometry of first generation CT is the only one that can be implemented. As the beam cannot be moved, beam translation is achieved by translating the sample through the beam using a tomographic gantry.

6.1.2 Reconstruction Algorithm

Since the advent of computed tomography techniques, several reconstruction algorithms have been designed and implemented to generate images from projection data. These reconstruction algorithms can broadly be classified into 2 groups – Fourier based algorithms; and Linear Algebraic algorithms. Each group has its advantages and disadvantages over the other. The following subsection gives a brief overview of Fourier based and algebraic reconstruction techniques, describing why one is preferred over the other for reconstruction in NSECT.

6.1.2.1 Overview of Fourier Based and Algebraic Algorithms

The principle for Fourier based algorithms comes from the Central Slice Theorem (also called Fourier Slice Theorem) which states that the Fourier transform of a parallel projection of an image $f(x,y)$ taken at an angle θ gives a 'slice' through the centre of the two-dimensional transform $F(u,v)$, subtending at an angle θ with the u -axis [51].

This implies that a series of one-dimensional Fourier transforms of individual projections of the object taken between $0-\pi$ can be used to fill up the two-dimensional Fourier space of the object completely. The reconstruction part is simplified to a single two-dimensional Inverse Fourier transform.

Although this seems conceptually simple, a potential difficulty in implementation arises from the fact that the frequency space of the object is acquired in polar co-ordinates. Calculating a two-dimensional Inverse Fourier transform in polar co-

ordinates is a difficult task to implement. Hence, projections acquired on polar grids must be remapped to Cartesian grids to reconstruct the original object.

An example of Fourier based reconstruction algorithm is the commonly used Filtered Back-Projection (FBP), which is an improvement over simple back-projection. In simple back-projection, because a priori information about the object is not available, an assumption is made that the intensity along the entire projection length follows a uniform distribution. This assumption introduces blurring in the reconstructed image, in the form of a radial frequency component ' $1/\xi$ ' introduced in the polar-Cartesian remapping. To correct for this blurring, the two-dimensional Fourier transform must be multiplied by the inverse of the distorting radial frequency component prior to back-projection. Blurring can be considered as an impulse response of the object. Therefore, reconstruction of the original object can be achieved by de-convolving the back-projected image with the inverse of the impulse response. This process is known as filtered back projection [51, 52].

Although Fourier techniques are computationally cheaper and quicker than algebraic and iterative techniques, they require uniform sampling of the object with a sufficiently high number of samples to avoid aliasing. To reconstruct an $N \times N$ image matrix, at least $N\pi/2$ samples are required in the $0-\pi$ interval. Therefore, Fourier based algorithms are not favored for non-uniformly sampled and under-sampled cases.

Tomographic acquisition in NSECT is severely under-sampled. For example, in an NSECT experimental scan of an iron-copper sample, an 88×88 matrix was reconstructed from 8 projections angles. This matrix would require at least 138 angles for reconstruction with FBP without azimuthal aliasing. Due to the severity of under-sampling in the NSECT system, Fourier techniques are not suitable for NSECT.

Algebraic algorithms for tomographic reconstruction function by assuming that the cross-section of the original object consists of an array of unknowns, and then setting up equations for these unknowns in terms of the measured projection data [52]. The object can then be reconstructed by solving the equations simultaneously. To reconstruct an $N \times N$ image matrix, the minimum number of equations required is N^2 . In cases where these equations are not all independent, the number of equations needed may exceed N^2 . Hence these algebraic techniques (such as direct matrix inversion) are usually computationally exhaustive and difficult to implement for large image matrices [53].

Computer implementations of algebraic techniques include iterative techniques such as Arithmetic Reconstruction Technique (ART), Simultaneous Iterative Reconstruction Technique (SIRT), Bayesian Reconstruction Technique (BRT), etc. These techniques assign an initial guess for the solution and taking successive projections for the equations under consideration until the convergence point is reached. If a unique solution exists, the convergence point is defined as the unique solution. However, when

the acquired projections are not noise-free, the solution does not converge to a point, but oscillates in the neighborhood of the unique solution [52].

Algebraic techniques are highly attractive in situations where it is not possible to acquire a large number of projections, or the projections are not uniformly distributed over $0-\pi$. They can also incorporate some kind of a priori information about the object into the solution, for example, non-negativity constraints and finite boundaries of the original object. These properties of algebraic techniques make them ideal candidates for NSECT tomographic reconstruction.

The Maximum Likelihood Expectation Maximization (MLEM) algorithm for emission computed tomography is particularly desirable due to its ability to incorporate the Poisson nature of Photon counting noise in the accuracy of reconstruction. This algorithm is described in detail in the following section.

6.1.2.2 Maximum Likelihood Expectation Maximization

The MLEM algorithm is an iterative technique to calculate maximum probability estimates based on stochastic models of projection measurements which incorporate the effects of the Poisson nature of photon counting noise on the accuracy of reconstruction [54-56]. It follows principles based on Maximum Likelihood Estimation (MLE) methods [57].

The algorithm consists of 2 steps:

- i. **E-step** where we form the conditional expectation

$$E[\ln f(X, \theta|Y, \theta^n)] \dots\dots\dots \text{Eq. 3}$$

where,

$X \rightarrow$ Complete unobserved source data

$Y \rightarrow$ Incomplete observed projection data

$\theta \rightarrow$ Parameters to be estimated

$\theta^n \rightarrow$ Current estimate of the parameters

ii. **M-step** where the conditional expectation is maximized with respect to θ , with

θ^n held fixed to get the new parameter estimate θ^{n+1}

$$\frac{\partial}{\partial \theta} E[\ln f(X, \theta|Y, \theta^n)] = 0 \dots\dots\dots \text{Eq. 4}$$

Gamma detection in NSECT follows emission tomography principles similar to PET and SPECT, in that the gamma photons are emitted from within the sample. Hence, algorithms developed for emission tomography can readily be implemented in NSECT. Lange and Carson have described an algorithm for emission computed tomography, which will be implemented here to calculate the ML estimates for the object described on a pixelized grid [58].

The equation is described as:

$$\lambda_j^{n+1} = \frac{\sum_{i \in J_j} N_{ij}}{\sum_{i \in J_j} c_{ij}} = \frac{\lambda_j^n}{\sum_{i \in J_j} c_{ij}} \sum_{i \in J_j} \frac{c_{ij} Y_i}{\sum_{k \in I_i} c_{ik} \lambda_k^n} \dots\dots\dots \text{Eq. 5}$$

where,

i : subscript for projection path

j, k : subscript for pixel

I_i : Set of all pixels that contribute to projection i

J_j : Set of all projections contributed to by pixel j

λ : vector representation of the sample pixel source intensities

N_{ij} : Best current estimate of the number of detected photons originating from pixel j in the i^{th} projection

c_{ij} : probability of a neutron incident along projection path i causing a gamma photon to be emitted from image pixel j and be detected at the gamma detector.

An intuitive interpretation of this method is that the best current estimate of photons (N_{ij}) originating from pixel j in projection i , summed over all possible projections passing through pixel j , is set equal to the expected number of photons from that pixel ($\sum_{i \in J_j} c_{ij} \lambda_j$), and the resulting equation is solved for λ_j to give λ^{n+1} .

The EM algorithm has several advantages over other iterative and Fourier techniques [58].

- a. **Better tolerance to noise:** It is based on a stochastic model of projection measurements that incorporates the Poisson nature of photon counting, which is not accounted for by Fourier methods.
- b. **Greater reconstruction accuracy in low counts:** Although certain iterative techniques accommodate the presence of noise in the system (e.g. a weighted least-squares approach with weights proportional to the estimated variance

of each measurement), they do not incorporate an exact statistical model.

This difference is not a limiting factor in cases where counting statistics are high, because Poisson counting noise is only a part of the total system noise.

In low count cases, this difference is more pronounced and MLEM enjoys a distinct advantage over other iterative techniques.

- c. **Lower patient dose:** Better reconstruction accuracy in low count cases allows reduced patient dose.
- d. **Deviations from ideal scanning criteria:** MLEM can accommodate non-ideal scanning criteria such as non-uniform sampling and presence of attenuation, through its probability matrix c_{ij} . Fourier techniques are unable to account for these deviations.
- e. **Modeling detection probabilities:** The probability matrix allows incorporation of detection probabilities due to various physical effects used in the system, which in this study will be derived from the GEANT4 simulation. Some of these effects that will be included here:
 - i. Neutron beam width
 - ii. Non-uniform sampling
 - iii. Variation in spatial resolution

The following chapter describes the design of a Monte-Carlo simulation to generate this probability matrix.

6.1.3 Monte-Carlo Simulation of MLEM Probability Matrix

The probability matrix C_{ij} required for MLEM reconstruction is created using an independent Monte-Carlo simulation which models the acquisition geometry of the experimental system. In this simulated model, a predefined large number of neutrons are made to undergo “random walks” through a sample space, which is divided into square cells forming a grid. These grid cells are used to calculate the probabilities of neutron interactions in different segments of the projected path. Every neutron that passes through the sample space must cross a finite number of grid cells. Depending on the points of entry and exit of the neutron through the grid, the length of the neutron path lying in each grid cell will be different. The chance of a neutron interaction occurring in any cell is dependent on the length of the neutron path lying in that cell. For example, consider a square sample space divided into a grid of 9 equal square grid cells arranged in 3 rows and 3 columns. A neutron traveling horizontally through the first row will intersect with all 3 grid cells in that row. The path of the neutron intersecting with each cell will be equal. In this geometry, the probability of neutron interaction in each of these 3 grid cells will be $\frac{1}{3}$. For this same projection, the probability of neutron interaction in the remaining 6 grid cells is zero.

To determine the actual cell in which the neutron interaction takes place, the total length of the neutron through the sample, in this case the 3 cells of the first row, is first normalized to 1. A random number between 0 and 1 is used to determine the point of

interaction of the neutron along this path. The cell coinciding with the random location selected along the neutron path is assigned the probability of occurrence for that neutron event. In the 9 grid cell example, if the random number drawn lies between 0 and 0.33, the interaction is assigned to cell 1. Similarly, a random number between 0.34 and 0.66 assigns the interaction to cell 2, and a random number between 0.67 and 1 assigns the interaction to cell 3.

This process is repeated for a predefined number of neutrons to complete one projection. The beam is then translated tomographically through the width of the sample space at a predefined spatial sampling rate by moving the entry and exit points of the neutron within the grid according to the translate-rotate geometry of first generation CT. As the beam travels along different projections in the tomographic geometry, the number of interactions assigned to each grid cell increase. The overall probability of a neutron interaction occurring within each grid cell is calculated as the fraction of the total incident neutron events that are assigned to that cell. The result of this probability estimation is an 'interaction matrix' containing a map of neutron interactions over different regions of the sample space.

The user can select the following parameters to create this matrix: number of particles in beam (number of Monte-Carlo histories), diameter of the beam, spatial and angular sampling rates, and number of pixels in the sample space.

The calculation of this probability matrix does not take into account the presence of any modeled element nuclei. The resulting interaction matrix is simply a randomly generated map of expected neutron interactions in different regions of the sample space based on the scanning geometry alone.

While incorporating the inelastic scatter interaction cross-section of each element may perhaps provide a more accurate estimate, this information is left out of the system for three reasons:

- a) Reconstruction through NSECT is performed individually for each element. For multi-element samples, each element is reconstructed individually and the resulting images are combined after reconstruction. Under this system, reconstruction from each element is assumed to be independent of the remaining elements in the sample. Assuming no prior knowledge of the geometry of the sample being scanned, the probability of neutron interaction depends primarily on the geometry of acquisition and not on the geometry of the sample.
- b) This sample-free approach allows a single interaction matrix to be used in reconstructing all elements acquired using that geometry. Computing this probability map is a time-consuming computation task, which is cumbersome to perform repeatedly for every combination of element and acquisition geometry that needs to be reconstructed. If element distribution were incorporated into the

sample space, the interaction matrix would have to be re-evaluated for every element distribution in the sample.

- c) Modeling the element distribution of the sample in the Monte-Carlo matrix simulation would imply that information about the structure of the sample is available a priori, which may not always be true in a clinical scenario.

Therefore, the probability matrix calculates the expected probability of interaction for a single element acting independent of the remaining elements in the sample, without including any prior information about the sample.

Simulation studies for this probability matrix calculation model have demonstrated that 10,000 neutron events are adequate for reconstruction accuracy of 95% [59].

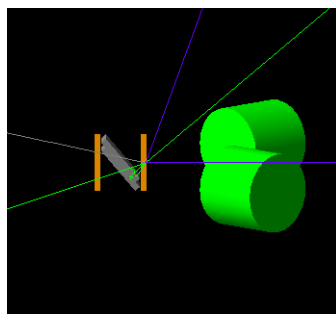
With these reconstruction tools implemented, the next step in tomographic reconstruction is to evaluate the NSECT tomography simulation by comparing simulated results with experimental data. This evaluation and validation experiment is described in the next section.

6.2 Evaluation of NSECT Tomography System Simulation

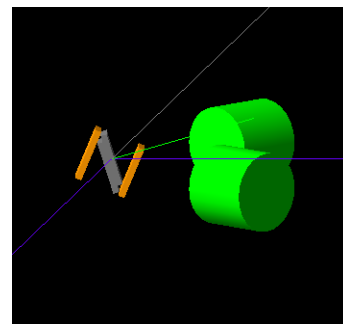
As the NSECT system simulation has been tested and validated for spectroscopic acquisition, the next step is to expand it to include tomographic scanning. As described in section 4.1.3, this expansion is performed by incorporating the tomographic gantry

chamber into the acquisition system. A sample that needs to be scanned tomographically is simply placed onto the gantry chamber which translates and rotates it along a projection path defined by the user.

Evaluation of the NSECT tomography system is performed with the composite iron-copper tomography sample described in section 4.2.1.3. Figure 24 shows two views of the composite sample being scanned with the tomography simulation. In both views, the orange bars in the sample are made of copper and the grey bars are made of iron. Gamma detectors are shown as green cylinders. Neutrons are shown as a blue line that enters from the right side of this image. Neutrons scattered off of the sample are shown as blue lines going away from the sample. Gamma-rays created through inelastic scatter are shown as green line originating from the sample. Figure 24a shows the sample oriented at the initial 0 degree angle and figure 24b shows the sample rotated clockwise by 22.5 degrees.



(a) Sample aligned at the initial position of zero degree



(b) Sample rotated clockwise through 22.5 degrees

Figure 24. GEANT4 tomography simulation for the composite iron-copper tomographic sample. The two views show the sample rotated through 22.5 degrees. The orange bars correspond to copper, grey bars to iron, and the green cylinders show HPGe detectors. The blue lines correspond to incident and scattered neutrons while green lines correspond to gamma rays created through inelastic scatter.

The sample is rotated through 8 angles and translated through 11 positions at each angle to acquire a tomographic image with 88 projections. This acquisition geometry is identical to the tomographic acquisition geometry used in the physical experiment.

Three criteria are used for validation of the tomography system. Each criterion is validated by comparing with experimental data acquired from an NSECT scan of the physical sample. For the system to be considered valid, first the simulated and experimental spectra must satisfy the conditions for spectral matching, i.e. the gamma energy peaks in the simulated spectrum must be observed at energies corresponding to prominent excited state transitions in the target nuclei and locations of peaks in the simulated spectrum must be in agreement with peak locations in the experimental spectrum. Second, the reconstructed images must show a distribution of pixel intensity in regions corresponding to the location of the sample. Third, the width of each iron and copper arm of the sample must be comparable between the simulated and experimental reconstructed images.

Figure 25 shows a comparison between the experimental and simulated spectra from this sample. The simulated spectrum is shown as a solid red line and the experimental spectrum is shown as a dotted black line. Table 8 lists the energy peaks seen in the simulated and experimental spectra along with the percentage variations in their heights. 10 gamma energy peaks corresponding to energy transitions in iron and

copper are identified in both spectra at identical locations. Peaks are seen for iron at 847 keV, 1039 keV, 1238 keV and 1811 keV, and copper at 669 keV, 962 keV, 1115 keV, 1327 keV, 1483 keV and 1863 keV.

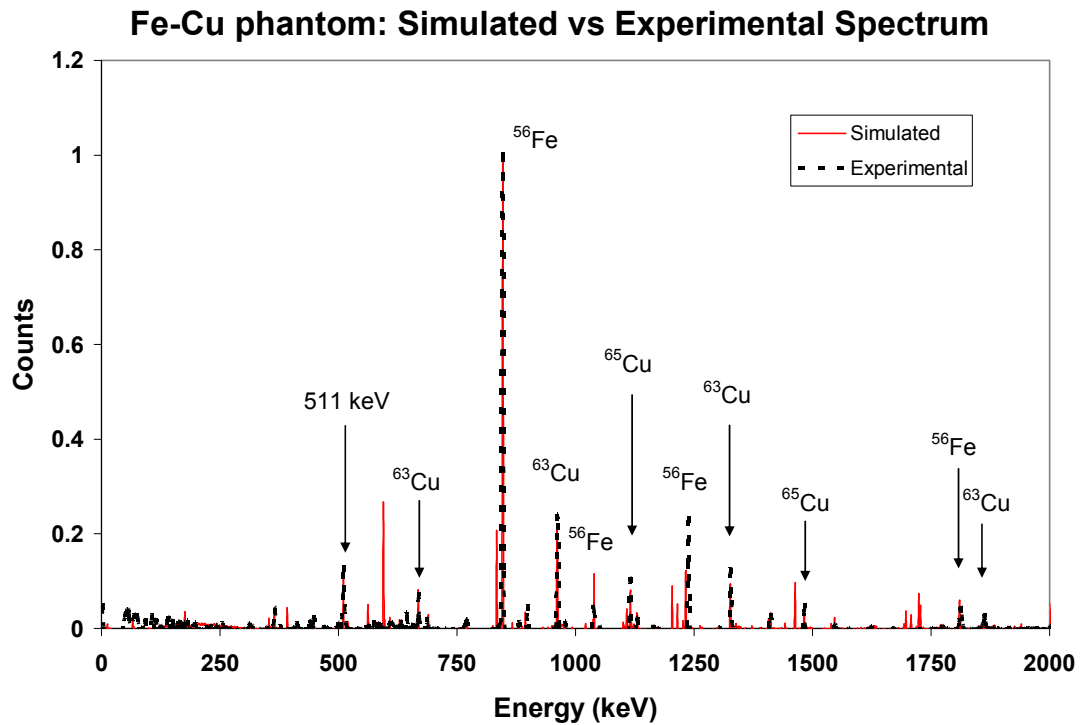


Figure 25. Comparison of simulated and experimental normalized gamma spectra for the iron-copper tomography sample. Gamma spectra from all projections are added to form this composite spectrum. The simulated spectrum is shown as a solid red line, while the experimental spectrum is depicted by an overlaid dotted black line. Energy peaks are identified for several gamma lines in both elements.

Isotope	Energy (keV)	Simulated counts (Normalized)	Experimental counts (Normalized)	Difference (%)
⁶³ Cu	669 keV	0.081	0.076	5.20%
⁵⁶ Fe	847 keV	1.000	1.000	0.00%
⁶³ Cu	962 keV	0.217	0.241	9.94%
⁵⁶ Fe	1039 keV	0.116	0.047	147.57%
⁶⁵ Cu	1115 keV	0.079	0.107	26.37%
⁵⁶ Fe	1238 keV	0.121	0.238	49.29%
⁶³ Cu	1327 keV	0.093	0.129	28.03%
⁶⁵ Cu	1483 keV	0.032	0.053	39.60%
⁵⁶ Fe	1811 keV	0.059	0.048	23.22%
⁶³ Cu	1863 keV	0.015	0.031	51.18%

Table 8. Analysis of gamma energy peaks from the simulated and experimental spectra for the mixed iron-copper tomographic sample. While 10 peaks are identified in both the spectra, only 3 peaks show differences under 10%. These peaks (shown in shaded cells) are the only ones considered for tomographic reconstruction.

All energy peaks in each spectrum have been normalized to the height of the tallest peak in the spectrum, which is seen at 847 keV corresponding to iron. The normalized peaks have been analyzed for percentage differences in height between the simulated and experimental spectra.

Of the 10 peaks identified, only 3 peaks show a percentage difference under 10%. Two of these peaks, at 669 keV and 962 keV correspond to ⁶³Cu, while the third, at 847 keV, corresponds to ⁵⁶Fe. The remaining peaks show differences ranging from 23% to 150%, which can be attributed to several factors.

The peak from ⁵⁶Fe at 1039 keV shows a large percentage difference due to a considerable overlap with a gamma line from ⁷⁰Ge that occurs at 1039.49 keV.

Neutrons that are elastically scattered onto the HPGe detectors from the sample may interact with the Ge in the detectors to cause inelastic scatter gamma emission. As the gamma-ray is emitted within the detector, its probability of detection is much greater. Similar peaks from Ge are also seen at 595 keV and 834 keV, but these do not overlap with any other energy peaks of our interest.

The peak at 1238 keV from ^{56}Fe has a similar overlap with a ^{70}Ge gamma line at 1237.3 keV. However, as this gamma line from ^{70}Ge is less intense than the gamma line at 1039.49 keV, the error in the difference is smaller for this peak than for the peak at 1039 keV.

Peaks at higher energies in the experimental spectrum are affected by the reduction in HPGe detector efficiency, which depends on the detector crystal and the configuration of the acquisition geometry. Correction for this reduction in efficiency requires detailed modeling of gamma detection efficiency for each experiment along with exhaustive calibration of the gamma detectors over a wide energy range. As many of these experiments have been performed over 3 years ago, exact modeling of detection efficiency becomes difficult at this point. These energy peaks have been left uncorrected in this spectrum. Careful geometric analysis and detector calibration will be performed for future experiments to model detector efficiency as accurately as possible.

Because of the above findings, only the three peaks with differences of less than 10% between the two spectra have been considered for tomographic reconstruction in the experiments in this thesis.

Figure 26 shows the modulation in iron counts at each projection angle. This pattern of modulation of detected iron concentration is used to analyze the path of translation and rotation of the sample in the simulated system. The experimentally obtained modulation is shown as a dotted line while the simulated modulation is plotted as a solid line. For each spectrum, iron counts at every projection are normalized to the highest number of iron counts detected in the acquisition.

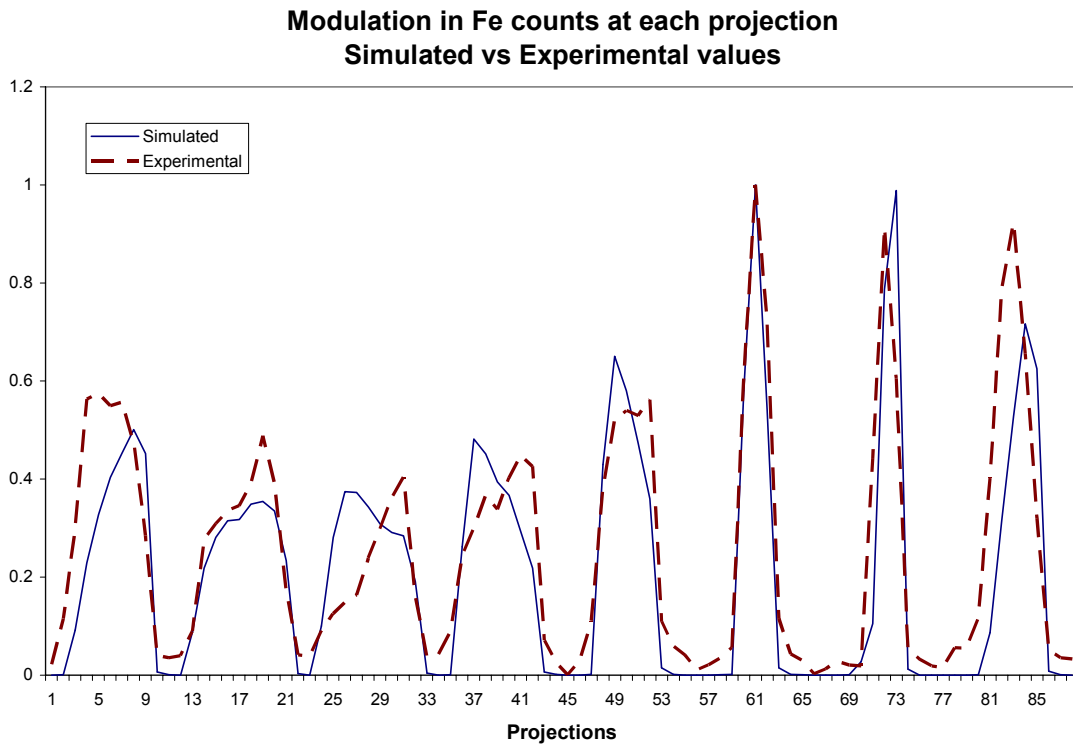
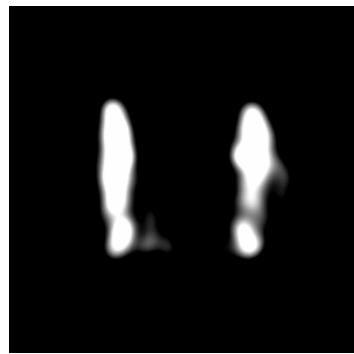


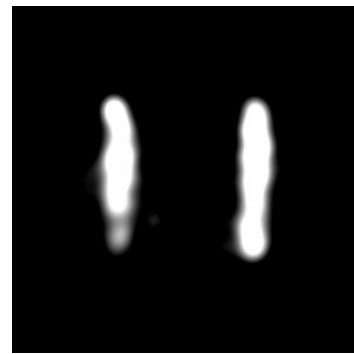
Figure 26. Comparison of the modulation in detected iron counts at each projection of the simulated and experimental simulation. The counts are normalized to the maximum detected counts in each simulation. While the overlap of the simulated and experimental curves is not exact, the general agreement in the pattern confirms the satisfactory rotation and translation of the sample in the simulated acquisition.

It can be seen that there is general agreement in the pattern of modulation between the simulated and experimental acquisitions. While the peaks are not exactly overlapping with each other, the pattern is consistent between the two. The difference in the overlap can be attributed to minute differences in the geometry of acquisition in the experimental system. The GEANT4 simulation places the sample at positions corresponding to locations used during experimental acquisition. However, due to fluctuations in the neutron beam and mechanical tolerances in the sample translation assembly, it is difficult to ensure that an identical volume of iron is scanned in both acquisitions. For example, for a projection where the beam is parallel to the longitudinal edge of the iron bars, a small difference in alignment can lead to an increase or decrease in the volume of iron illuminated by the beam. Hence, slight differences between the simulated and experimentally detected iron counts are expected.

Figure 27 and 28 show reconstructed images from the tomographic acquisitions for iron and copper respectively. Each element is reconstructed separately using the MLEM algorithm with 7 mm beam width, 8 angles and 11 spatial positions per angle for a total of 88 projections.



(a) Simulated



(b) Experimental

Figure 27. Reconstructed images of copper from simulated and experimental acquisition of the iron-copper N-sample. Gamma intensity is observed in regions corresponding to copper.



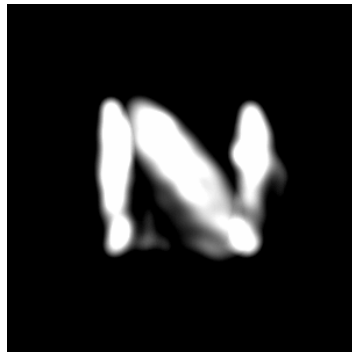
(a) Simulated



(b) Experimental

Figure 28. Reconstructed images of iron from simulated and experimental acquisition of the iron-copper mixed N-sample. Gamma intensity is observed in regions corresponding to iron.

Figure 29 shows the combined image of the iron and copper regions, obtained by adding the images reconstructed separately for iron and copper. As can be seen, the intensities in the simulated image are distributed in regions corresponding to copper and iron. The alignment between the iron and copper regions matches the alignment seen in the experimental reconstruction as well as in the original sample.



(a) Simulated



(b) Experimental

Figure 29. Combined reconstructed images from simulated and experimental acquisition of the iron-copper mixed N-sample. Images for iron and copper have been reconstructed separately and the resultant images have been added together.

Figure 30 shows a line profile of the intensity distribution through the center of the reconstructed images. A slight broadening of the regions for iron and copper is observed in both sets of images. At half maximum intensity, the width of the left copper regions is 10 mm in the simulated image and 9 mm in the experimental image, while the width of the right copper region is 9 mm in the simulated image and 8 mm in the experimental image. The width of the iron region is 18.5 mm in the simulated image and 17 mm in the experimental image. This spread in reconstructed widths can be attributed to the tomographic acquisition geometry in both cases. While each of the iron and copper bars in the original sample measured 6 mm in width, they were scanned using a 7 mm wide beam. Therefore, a spatial spread in reconstructed intensity is expected. Table 9 summarizes the differences in the widths of the reconstructed regions in both images.

Line profiles from Simulated and Experimental Reconstructions

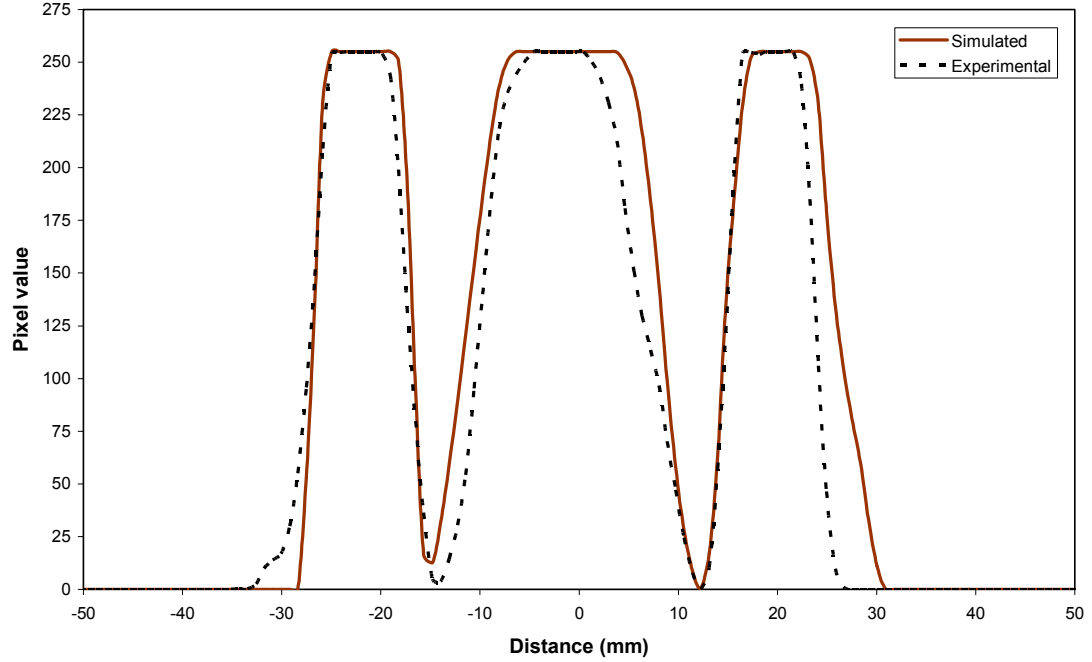


Figure 30. Line profile of the intensity distribution through the simulated and experimentally reconstructed images. At half max, the width of the left and right copper regions is 10 mm and 9 mm in the simulated image, and 9 mm and 8 mm in the experimental image. The width of iron is 18.5 mm in the simulated image and 17 mm in the experimental image.

	Region	Simulated			Experimental		
		Cu left	Cu right	Fe	Cu left	Cu right	Fe
FWHM	Reconstructed width (mm)	10.0	11.0	19.0	10.0	9.0	17.0
	Original width (mm)	6.0	6.0	14.1	6.0	6.0	14.1
	Difference error (%)	66.67%	83.33%	34.73%	66.67%	50.00%	20.54%
Max	Reconstructed width (mm)	7.0	6.0	11.0	6.0	6.0	9.0
	Original width (mm)	6.0	6.0	14.1	6.0	6.0	14.1
	Difference error (%)	16.67%	0.00%	22.00%	0.00%	0.00%	36.18%

Table 9. Summary of the differences in widths of the reconstructed regions in the simulated and experimental images.

Widths of the different regions have been calculated at two values of pixel intensity, 125 (FWHM), and 250 (maximum). The errors in difference between the reconstructed and original widths are seen to decrease at maximum intensity.

6.3 Tomographic Simulation of Iron Overload Sample

With the tomography simulation of the NSECT successfully validated, the next step is to acquire a tomographic dataset from the non-uniform iron overload sample described in section 4.2.3.

Before the acquisition and reconstruction methods for this sample are described, it is important to discuss two changes made to the tomographic simulation. Between the stages of system evaluation for spectroscopy and sensitivity analysis for the torso sample, the version of GEANT4 on the computers was updated to fix a flaw in memory management in the older version which caused repeated software crashes in the simulation. This memory management flaw had not been observed for any of the system evaluation samples as their relatively lower quantities of hydrogen generated significantly lesser elastic scatter data. While the output from GEANT4 can be customized to record the minimum amount of necessary data, every interaction must still be executed in its entirety. With the large amount of elastic scatter data that was generated in the torso samples, the software often crashed after running 5000 neutron events. The suggested fix for this problem was a version upgrade.

While the newer version was able to correct this memory management problem, it showed a significant drop in the overall speed of execution over the older version. As a result, a simulation that required 1 day of computing time with the older version now required 9 days. To compensate for this drop in efficiency, two changes have been made to the tomography simulation.

The first change made is to the shape and size of the gamma detectors used in the system. While the 10 cm diameter cylindrical gamma detectors used during system evaluation show adequate efficiency in gamma detection, their efficiency in the torso tomography system is significantly lower as they have to be moved farther back to accommodate the translating torso, which requires a minimum 40 cm of linear translation in the system. In the spectroscopy system, the gamma detectors are placed at a distance of 15 cm from the edge of the torso. This distance must be increased to at least 45 cm in the tomography system. Therefore, the $1/R^2$ reduction in detection efficiency becomes a significant factor. One proposed technique to compensate for this loss in efficiency is to use an array of gamma detectors to completely surround the sample in the form of a gamma-sphere. To implement the gamma sphere design in NSECT, the number of detectors was initially increased to six. While a six-fold efficiency increase was observed with the six-detector system as expected, a simultaneous unexpected increase was observed in the computing time for the simulation. With no other changes made to the computing system or simulation, the logical conclusion drawn was that this

was likely due to GEANT4 having to monitor 6 sensitive detectors instead of 1.

Designing a gamma sphere with 20 detectors of 10 cm diameter could lead to further loss of computing efficiency. Therefore, in order to avoid a potential computing efficiency problem, each array of detectors was substituted by a single detector with 30 cm diameter.

Detectors with 30 cm diameter are larger than most HPGe gamma detectors commonly used in nuclear experiments today. However, techniques have been described to grow large detectors of any shape and size by combining smaller individual 'segments' and are currently being investigated. Some of the segmented detectors that are currently available commercially, for example the segmented co-axial detectors manufactured by Canberra Eurisys, are able to behave like single crystal monolithic detectors by eliminating the dead zone and absorbing material between the segments. Others increase the efficiency of the detector through an 'add-back' technique that sums the energy deposited by a single particle that scatters through the individual segments [60]. With improvements in detector technology, larger gamma detectors of these dimensions may not be unrealistic.

The six gamma detectors are arranged around the sample in the form of an array as shown in figure 31. The thickness of each detector is retained at 9 cm, and it is placed at a distance of 42.5 cm from the center of the rotation of the tomography system. This geometry ensures that the sample is able to move freely inside the detector array

without striking any of the detectors. The geometry ensures that neutrons which pass through the sample without any interaction are able to exit the world without striking the detector.

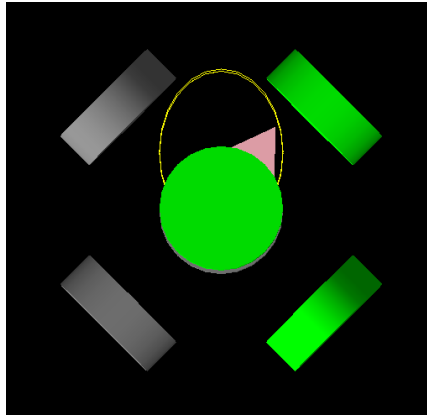


Figure 31. Gamma detector array geometry placed around the iron overload torso sample. Five detectors are visible in this view. The sixth detector is directly below the green detector in the center of the image. This detector geometry improves the detection efficiency of the system by a factor of 10.3.

The improvement in efficiency with the larger detector geometry is analyzed through a simulation of the tomography sample used for system evaluation in section 6.2. The iron-copper sample is scanned spectroscopically for 10 million neutron counts with each of the two detector geometries in consideration and the difference in the height of the ^{56}Fe peak at 847 keV is used as an estimate for the increase in efficiency of the system. For the detector system with 10 cm detectors, 11809 counts were measured in the 847 keV peak, while the 30 cm diameter detectors measured 121599 counts. The efficiency of the system is thus found to increase by a factor of 10.29 with the larger detectors. All the data in the tomography analysis is corrected for the efficiency increase.

Comparison of Detector Geometries: Simulated Spectrum for Iron-Copper Sample

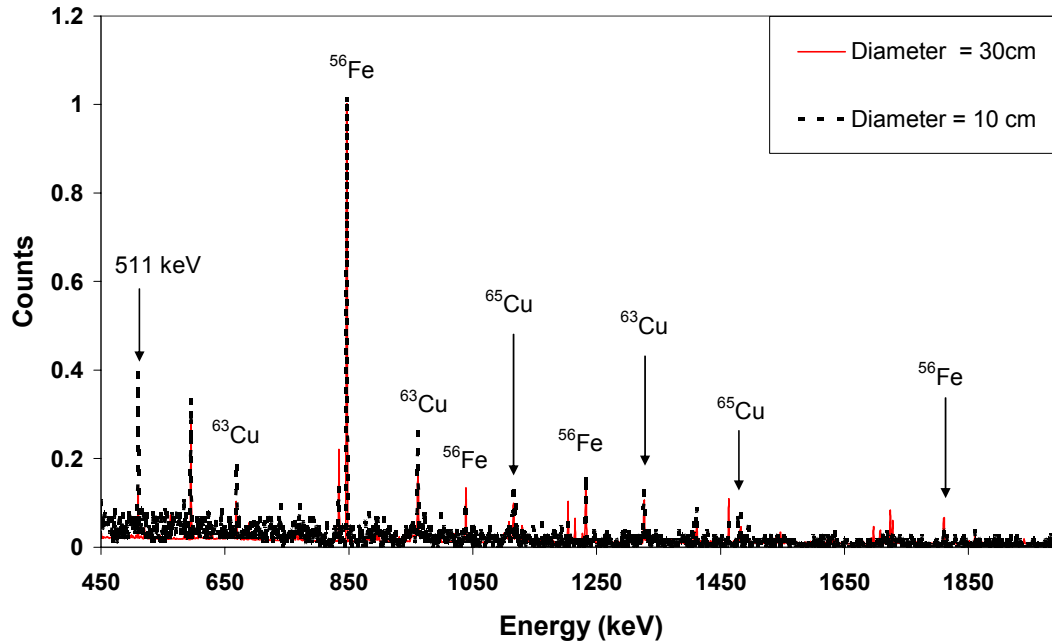


Figure 32. Comparison of gamma spectra for the array detectors with different diameters. With the larger detector geometry, the system provides an increase in detection efficiency by factor of 10 while the shape of the gamma spectrum remains relatively unchanged.

The second change made to the system to increase the speed of simulation is the removal of elastic scatter from the physics list. As mentioned earlier, in samples with high hydrogen content, elastic scatter interactions make up a substantial fraction of the total interactions observed in the sample. They affect the spectrum in two ways. First, neutrons scattering elastically with hydrogen scatter onto the gamma detectors which gives rise to the germanium gamma lines seen in the spectrum. Second, elastic scatter reduces the energy of the incident neutrons with each interaction, which leads to reduced detection of nuclei of interest. This effect is especially pronounced for nuclei

that have their first excited state close to the energy of the incident neutron. Few neutrons that undergo elastic scatter in the sample are able to retain their initial incident energy. For example, consider ^{12}C , which has its first excited state at 4438.91 keV. When this isotope is scanned with a 5 MeV beam, the presence of elastic scatter significantly reduces the excitation of carbon nuclei unless the initial incident neutron energy is sufficient to compensate for this loss. Because of this reason, eliminating elastic scatter will lead to an increase in the detected iron in the simulated torso sample.

This increased iron detection must be investigated and quantified in order to compensate for the lower number of neutrons required to obtain a certain number of counts in the iron peak.

Figure 33 shows a spectrum from an iron sample in water. As with most hydrogen containing samples, this spectrum shows several peaks corresponding to germanium. The dotted gray line shows the uncorrected gamma spectrum, while the solid black line shows the spectrum after background reduction. While the peaks from germanium can be significantly reduced through sample-out background subtraction, this process requires an additional scan with a water sample, which for a large tomographic acquisition such as this one, can be extremely time consuming.

Simulated Spectrum from Fe lesion in Water Torso

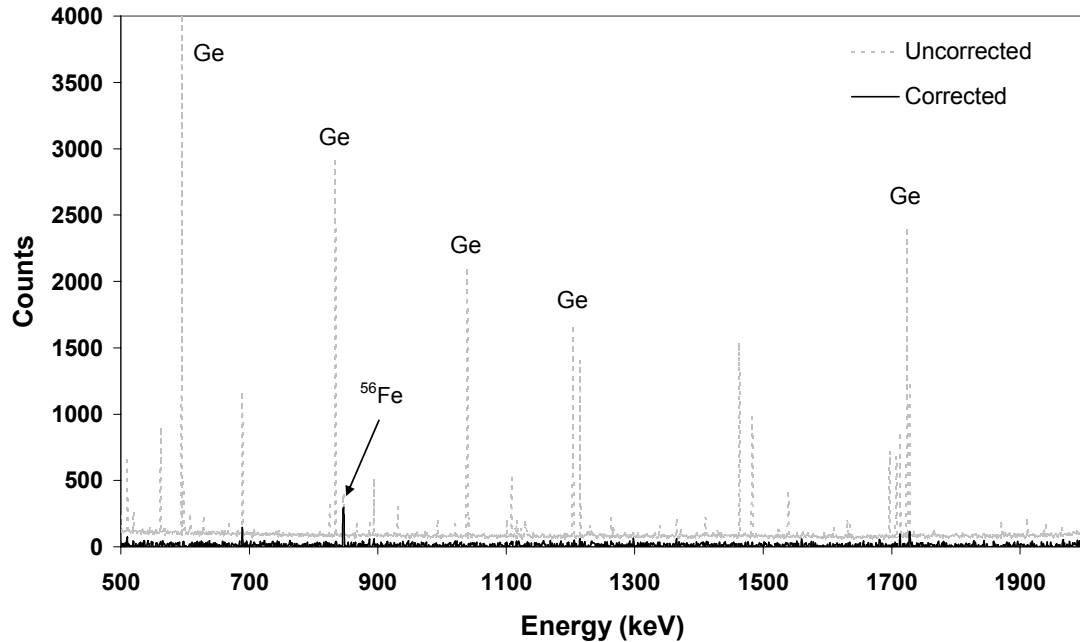


Figure 33. Gamma spectrum for an iron sample in water with elastic scatter included in the system. The original uncorrected spectrum is shown as a dotted line while the background corrected spectrum is shown as a solid line. Gamma lines seen in the uncorrected spectrum can be significantly reduced through sample-out background reduction.

Figure 34 shows a comparison of two simulated spectra for the iron sample in water, one obtained with elastic scatter and the other without. Both spectra are normalized to the number of neutrons used. As expected, the spectrum without elastic scatter is relatively free of gamma lines even without any background reduction. The peak corresponding to iron is seen to be taller in this spectrum. Both effects are expected due to reasons described above.

Iron sample in Water: Physics List Testing

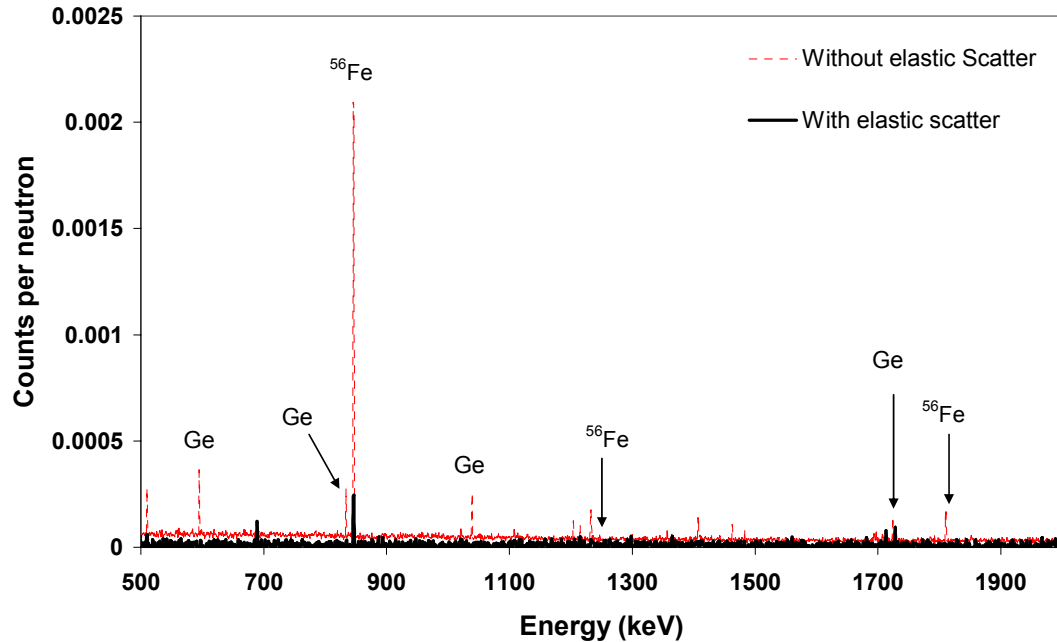


Figure 34. Comparison of gamma spectra from an iron sample in water with and without elastic scatter. The elastic scatter spectrum is background corrected using the sample-out subtraction technique. The dotted red line corresponds to the system without elastic scatter while the system with elastic scatter is shown as a solid black line. Both spectra are normalized to the number of incident neutrons.

This simulation has been acquired for 800,000 neutron events with identical geometry to that used for tomography of the torso sample in the following section. With sufficient statistical accuracy in the spectrum, the relative height of the iron peak at 847 keV is found to differ by a factor of 8 between the two spectra. This correction is applied uniformly to all data in tomographic analysis.

Elastic scatter is an important constituent of patient dose. A significant fraction of neutrons that deposit energy into tissue do so through elastic scatter. Therefore, the simulation model without elastic scatter cannot be used to obtain any reasonable

estimate of patient dose. All dose analysis experiments described in subsequent chapters have been performed with a simulation model which includes elastic scatter.

One more effect is observed when elastic scatter is reduced from the simulation. Without elastic scatter, a significant reduction is observed in the neutron capture energy peak at 2224 keV. This is likely due to the reduction in repeated collisions of neutrons in the sample which will be observed with elastic scatter. Without these repeated collisions, neutrons have lesser chance of interacting with hydrogen in the sample through neutron capture.

With the above modifications to the simulation system, the next step is to perform tomographic acquisition of the non-uniform iron overload torso sample.

Due the large number of variables present in the NSECT tomography simulation, a two disease-model method has been used to approach the optimization problem systematically, where a control sample is first used to determine the effects of varying the different parameters in the system, and then testing the optimized parameters with a clinically relevant disease model. Both models are based on the tomography iron overload sample described in section 4.2.3 and differ from each other only in the concentration of iron within different regions.

The control model is designed with high concentrations of iron that are expected to be successfully reconstructed for several combinations of acquisition parameters. High concentrations of iron will reduce errors in the system that may otherwise be

caused by variability of iron concentration. Therefore, variations seen in the images will primarily be due to the combination of acquisition parameters and not due to insufficient accuracy in detection of iron. From the spectroscopy analysis described in chapter 5, it is known that NSECT can image an iron concentration of 5 mg/g with sufficient accuracy through single beam spectroscopy. Therefore, the control model is designed with an iron concentration of at least 5 mg/g in all regions corresponding to the liver. The two lesions are given concentrations of 10 mg/g and 20 mg/g. As it is not known what concentration differences can be detected in a tomographic scan, concentrations that are higher than the surrounding tissue by a factor of 2 and 4 are used as starting points. Unless the extreme concentrations can be detected with adequate accuracy, it is unlikely for the simulated system to be successful for a disease model with lower iron concentrations.

After successful reconstruction of the control model, the optimized parameters will be tested with a clinically relevant sample designed with two lesions of 5 mg/g and 3 mg/g in an overload-free liver. These two lesion concentrations are selected based on results of spectroscopic analysis where 5 mg/g was detected with sufficient accuracy while 3 mg/g was not, thereby enabling some comparison between the spectroscopy and tomography techniques.

The following section describes the analysis of each of these disease models.

6.3.1 Acquisition Geometry

The acquisition geometry for tomographic scanning of the torso sample must account for 3 parameter combinations – number of neutrons, spatial sampling and angular sampling. The goal of selecting the acquisition geometry is to include as many combinations of parameters as possible while ensuring maximum efficiency in the system. In order to avoid performing a new simulated acquisition for each combination of parameters in consideration, the simulation is run only once with the highest sampled combination. As the data is acquired and sorted by individual projection, each projection can be treated as an individual spectroscopic simulation by itself. As this simulation is based on a Monte-Carlo technique that uses a different random seed for each projection, every projection is truly independent of every other. Therefore, any combination of projections can be used to recreate new acquisition geometries without having to rerun the simulation.

The acquisition geometry corresponding to the highest-sampled combination uses the following acquisition parameters:

- Beam width = 0.5 cm
- Number of angles = 24, at 7.5 degree intervals between 0-180 degrees
- Number of translations at each angle = 52, at intervals of 0.5 cm

This combination allows the following lower sampled projections to be created:

Angles	Spatial steps	Beam width	Number of Projections
24	52	0.5 cm	1248
24	51	1 cm	1224
24	26	1 cm	624
24	13	2 cm	312
12	52	0.5 cm	624
12	51	1 cm	612
12	26	1 cm	312
12	13	2 cm	156
8	52	0.5 cm	416
8	51	1 cm	408
8	26	1 cm	208
8	13	2 cm	104
6	52	0.5 cm	312
6	51	1 cm	306
6	26	1 cm	156
6	13	2 cm	78

Table 10. Tomographic acquisition geometries evaluated for detection of iron overload in the liver.

The highest-sampled combination of parameters contains 1248 projections acquired at 24 angles with 52 steps at each angle. Sampling every alternate projection from this list forms a combination with 26 steps per angle with 24 angles. Sampling every alternate angle yields a combination with 12 angles and 52 steps per angle. Instead of sampling alternate steps, two successive positions can be added together to give a 1 cm beam. This technique is used to create a sampling scenario where a 1 cm beam is translated at increments of 0.5 cm through the sample. In physical experimental scenarios, it is often difficult to obtain high beam flux from a thin neutron beam.

Therefore, this pseudo-sampling combination has been investigated to explore the possibility of using a thick beam to scan thinner objects in the sample space.

This simulation is run for a total of 1.5 million events at each projection. To investigate the effect of reducing the number of incident neutrons on the simulation, the data from each projection is parsed to provide a smaller number of neutron events. This parsing is performed by randomly sampling a predefined number of neutron events and their resulting interactions from the complete projection file. The number of neutron events is parsed down to evaluate 7 values of incident neutron flux - 500000, 250000, 125000, 75000 and 25000.

Data parsing and angular and spatial projection sampling is performed using a combination of C programs, Perl scripts and programs in MATLAB.

The final element of data parsing with respect to the acquisition geometry is the need to create multiple tomographic data sets. Optimization of the NSECT tomography system is performed with ROC analysis of each combination of scanning parameters. To be able to generate meaningful ROC curves from a combination of parameters, multiple data sets are needed for each sample. While generating multiple data sets through independent simulations would be ideal, restrictions in simulation time make this process difficult. As this simulation is Monte-Carlo system which uses a random seed for every projection, each neutron event in the NSECT simulation is a random independent event. Therefore, it is reasonable to consider two files created from the

same overall data set as independent projections in different tomographic scans of the sample.

Ten sample files are created at each neutron count by randomizing the data and dividing the output file into multiple parts. For example, to generate 10 files with 500000 counts, the original data set of 1.5 million counts is randomized 3 times. Each randomized set is then split into 3 parts of 500000 counts each. Thus, although the overall data may have some overlap when added together, each individual data set can be considered independent of another.

The acquisition geometry described above was used to run this simulation for 1248 projections with 1.5 million counts per projection. To give the reader an idea of the time required to execute this simulation, acquisition of the complete dataset required 7 days of processor time with as many as 38 processors running the simulation simultaneously.

The following section shows reconstructed images from the tomographic acquisition of the iron overload torso sample.

6.3.2 Reconstructed Images

As described earlier in this chapter, tomographic images are reconstructed separately for each element in the torso using the MLEM algorithm for emission tomography. This reconstruction requires an estimation of the probability matrix C_{ij} , which is estimated using the Monte-Carlo simulation described in section 6.1.3. As

described earlier, satisfactory performance of the MLEM probability matrix simulation was found to be 95% accurate when 10000 neutron histories were used in the Monte-Carlo process. Therefore, in order to reconstruct images from the GEANT4 tomography simulation of the liver, the MLEM Monte-Carlo simulation is run with 10000 neutron histories for each combination of parameters in consideration for image reconstruction.

Two elements in the torso have been considered for reconstruction – iron in the liver, and carbon in the liver and spine. While quantification and analysis is performed only for iron, carbon is reconstructed to obtain visual verification of the validity of the tomography process. Images for each element are reconstructed by extracting the gamma peaks corresponding to that element separately from every projection file to form an NSECT sinogram. Peaks from ^{56}Fe are extracted for 846 keV and 847 keV and peaks for ^{12}C are extracted for 4438 keV and 4439 keV. Each sinogram is reconstructed using 25 iterations of the MLEM algorithm. This number has been estimated empirically using an experiment described below.

As MLEM is an expectation maximization algorithm, the reconstructed image first shows a rise in the SNR until it reaches a local maximum, and then begins to drop at the point where the algorithm begins to model noise into the image. From earlier experiments with tomographic reconstruction [61], it is known that the maximum value of SNR occurs between iterations 10 and 20. Therefore, all images are reconstructed with at least 25 iterations to safely include the iteration with maximum SNR. This value has

been empirically verified as shown in figure 35, which shows the variation in SNR for 4 regions of interest (ROI) with successive iterations of the MLEM algorithm for a reconstructed image of iron. The four ROIs correspond to regions within the liver, spine and the two lesions, and the background corresponds to a region in the torso that it outside the liver).

From figure 35, it can be seen that the SNR for all 4 regions peaks at around iteration 15 and declines when reconstruction is terminated at iteration 25. All images in this work are reconstructed using iteration 15 henceforth.

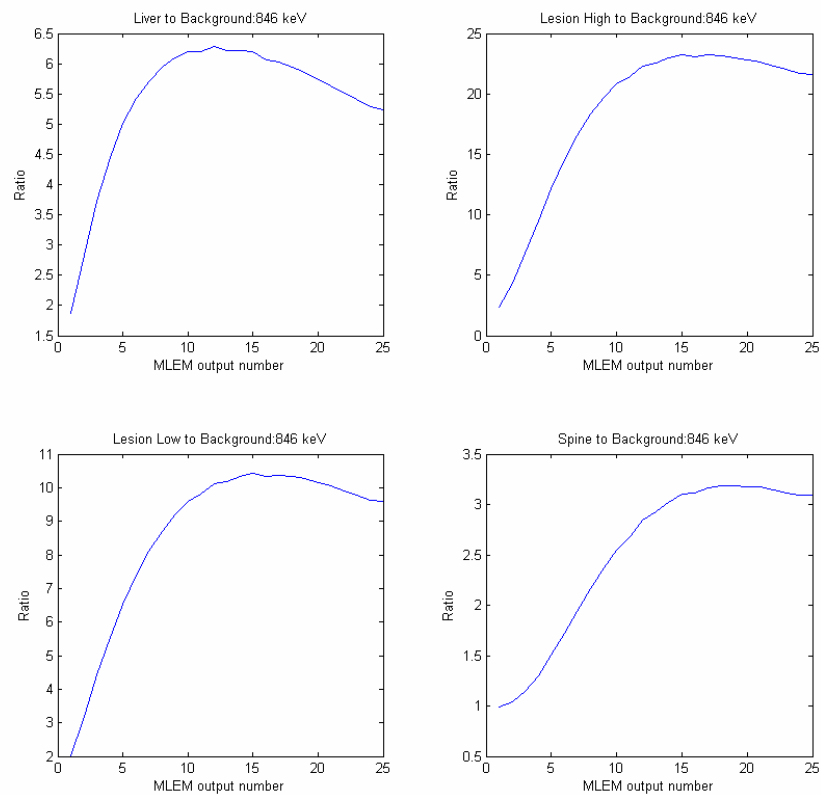


Figure 35. Variation in the SNR for 4 regions of interest in an image from iron with successive iterations of MLEM. The SNR appears to peak around iteration 15 and is on the decline when the reconstruction algorithm is terminated.

Figure 36 shows the reconstructed image for iron from the highest sampled scan geometry. This image uses 52 spatial projections at 24 angles with 0.5 step increments. Each image corresponds to a successive iteration of the MLEM algorithm. While images from several iterations of the MLEM algorithm are available, the data presented in this section has been restricted to 12 as the later images show no visible improvements.

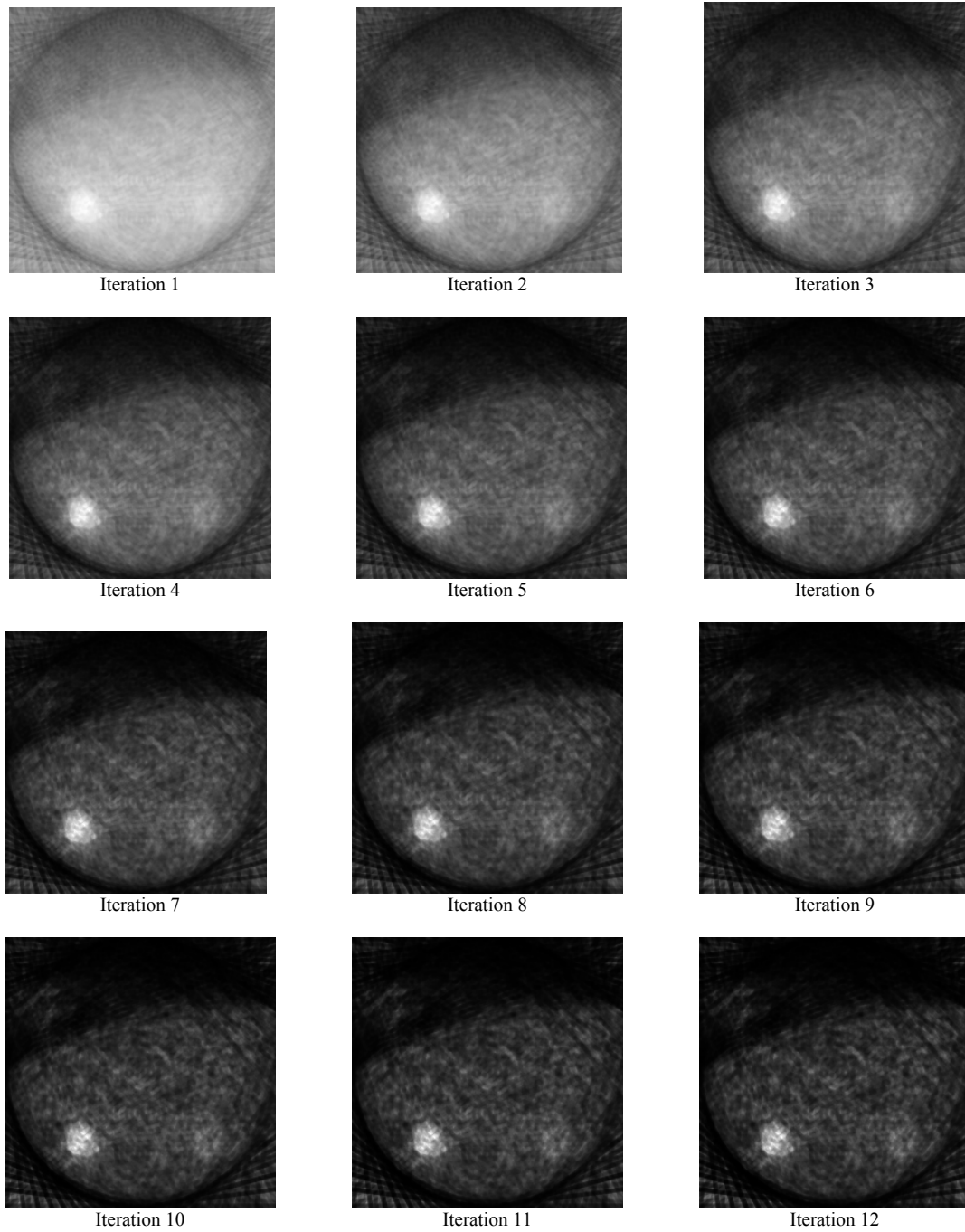


Figure 36. Reconstructed image for ^{56}Fe showing successive iterations of the MLEM algorithm. This image is reconstructed using the highest sampled acquisition geometry with 24 angles and 52 spatial steps at 0.5 cm increments. Each reconstruction is performed in a 260 x 260 pixel image grid.

As can be seen, the liver and the two high-concentration lesions are clearly visible above the background even to the naked eye. The two high-concentration lesions appear brighter than the rest of the liver. The variation in intensities of the 4 regions with different iron concentrations are observed to be in agreement with the variation in concentration. The brightest spot corresponds to the lesion with an iron concentration of 20 mg/g, the second brightest spot corresponds to the 10 mg/g lesion and the third bright region corresponds to the 5 mg/g uniform liver iron overload. Aliasing artifact is visible in the image. In the geometry seen in this figure, the beam enters from the left and scans from the bottom edge of the image to the top. Angles are acquired by rotating the sample in a clockwise direction. The region directly above the liver appears dark due to the shadow of the liver being projected onto that space as the liver is scanned. This shadowing effect is clearly visible in iteration 1 of the MLEM algorithm.

Figure 37 shows the reconstructed image for carbon using this same highest sampled acquisition geometry. Carbon in the torso sample is located in the liver and in the spine. The reconstructed images show excellent agreement with the original simulated sample.

The original sample and the reconstructed images from carbon and iron are shown side by side in figures 38 and 39 for a visual comparison.

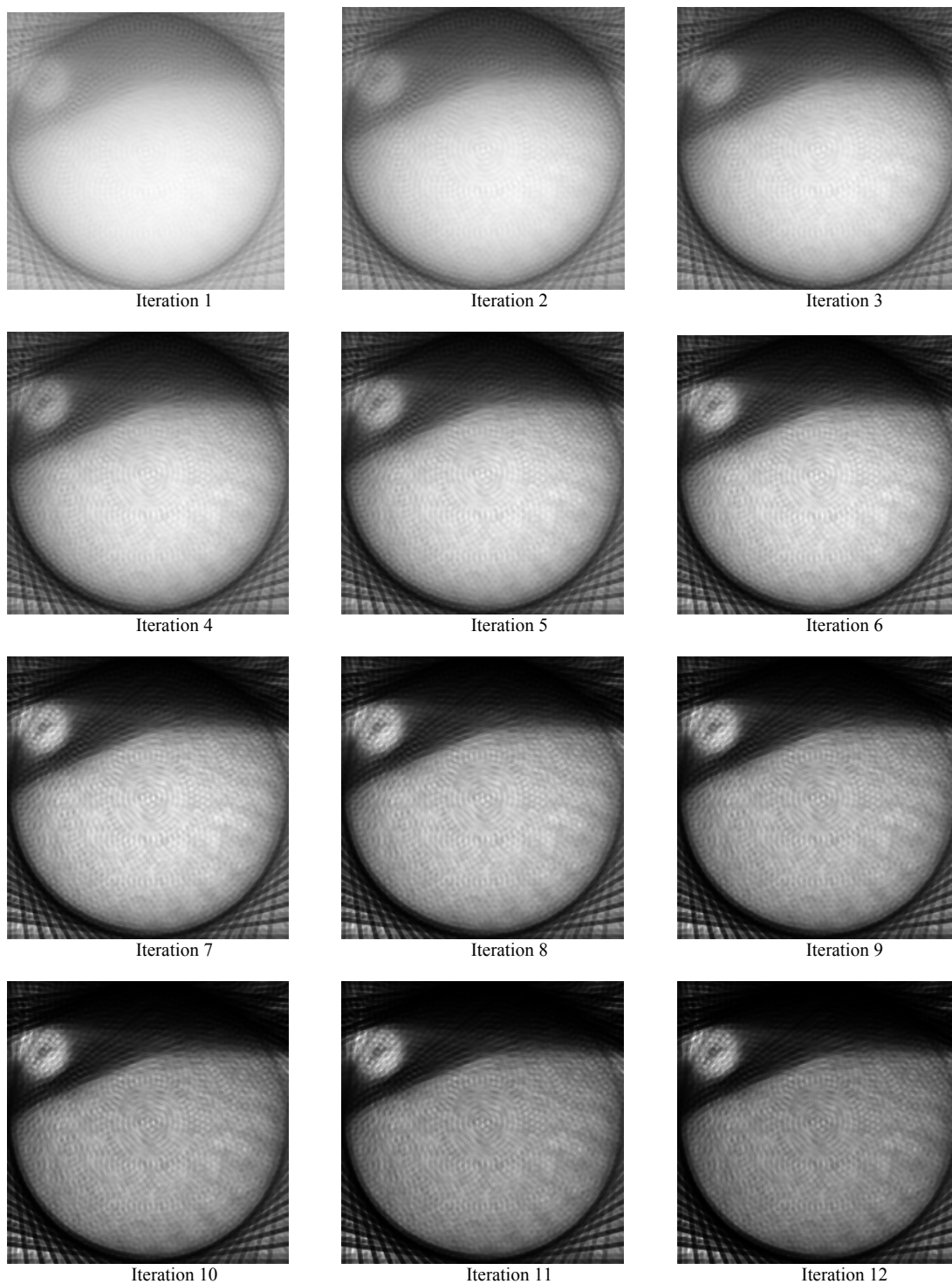
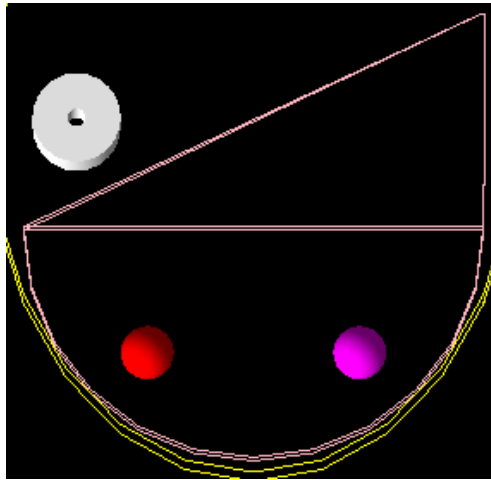
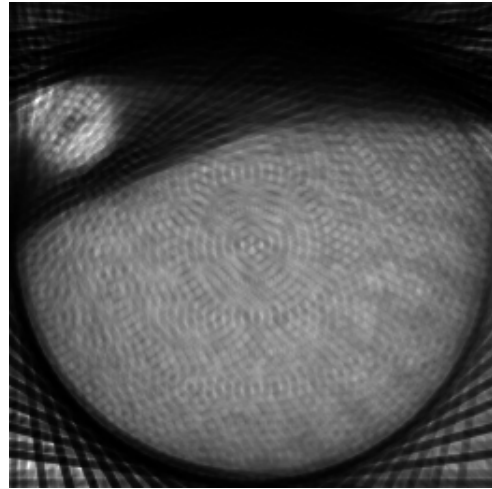


Figure 37. Reconstructed image for ^{12}C showing successive iterations of the MLEM algorithm. This image is reconstructed using the highest sampled acquisition geometry with 24 angles and 52 spatial steps at 0.5 cm increments. Distribution of intensities in the image corresponds to the distribution of carbon in the original sample. Aliasing artifact is visible in the image.

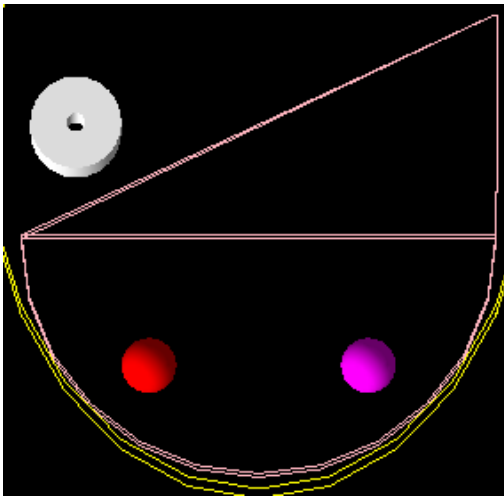


(a) Simulated sample

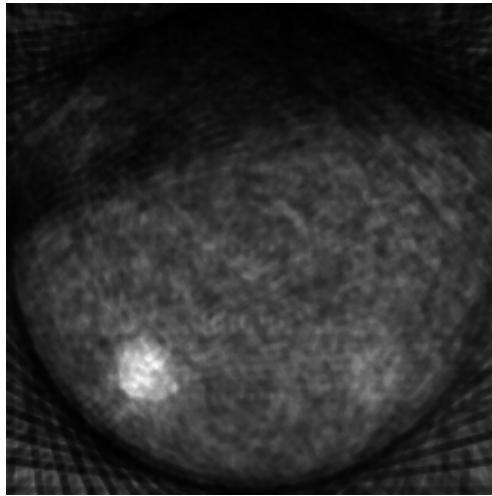


(b) Reconstructed Image

Figure 38. Comparison of the original sample with the corresponding reconstructed image for carbon. Intensities in the reconstructed image can be seen in regions corresponding to carbon in the original sample.



(a) Simulated sample



(b) Reconstructed Image

Figure 39. Comparison of the original sample with the corresponding reconstructed image for iron. The distribution of intensities in the reconstructed image is found to be in agreement with the distribution of iron concentration in the original sample.

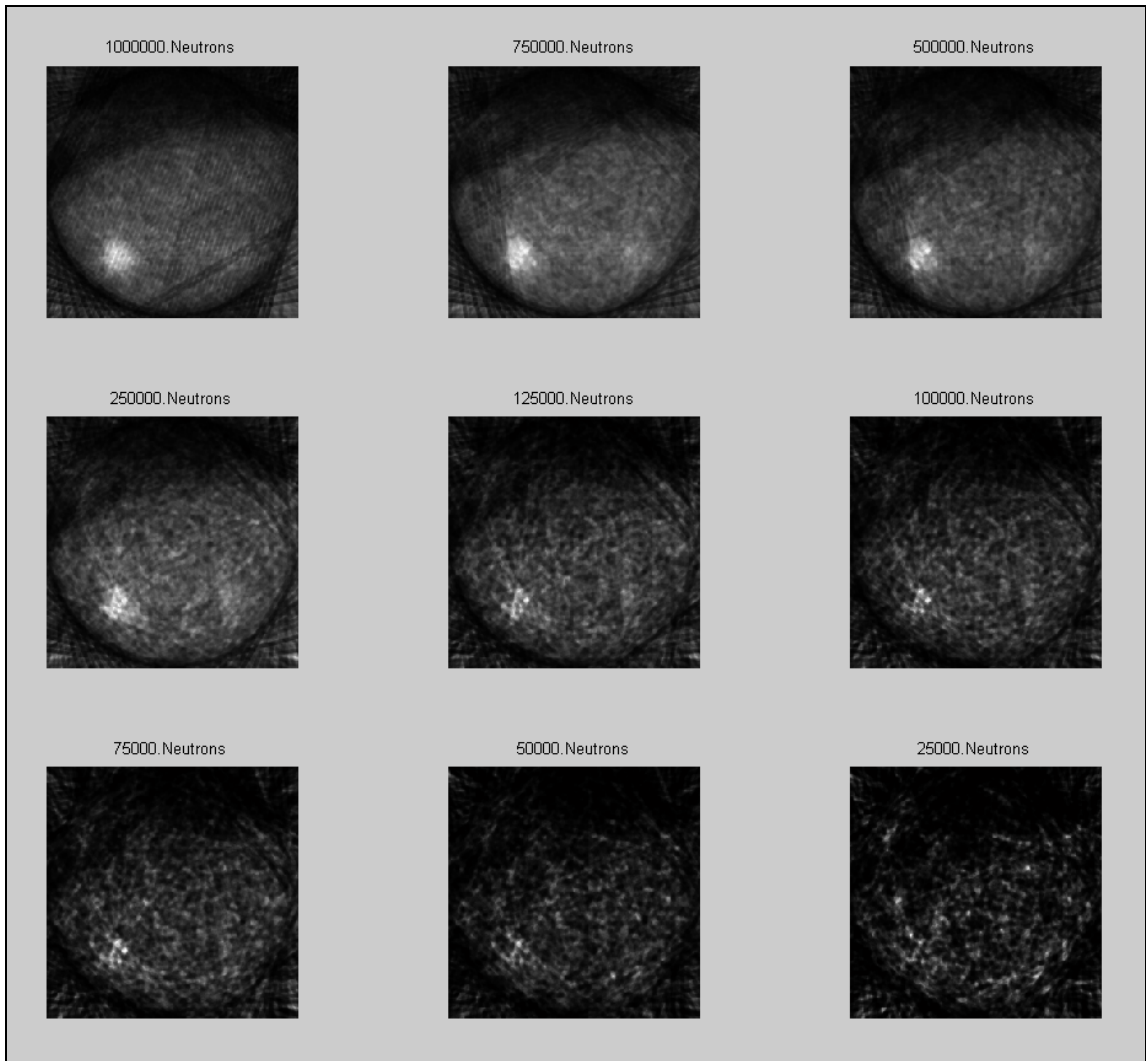


Figure 40. Effect of downsampling the number of neutron counts on the reconstructed image.

Figure 40 shows the effect of downsampling the number of incident neutrons on the reconstructed image. As expected, degradation in the image is observed when fewer neutrons are used per projection. Analysis to determine the loss in accuracy due to downsampling has been described in the next section.

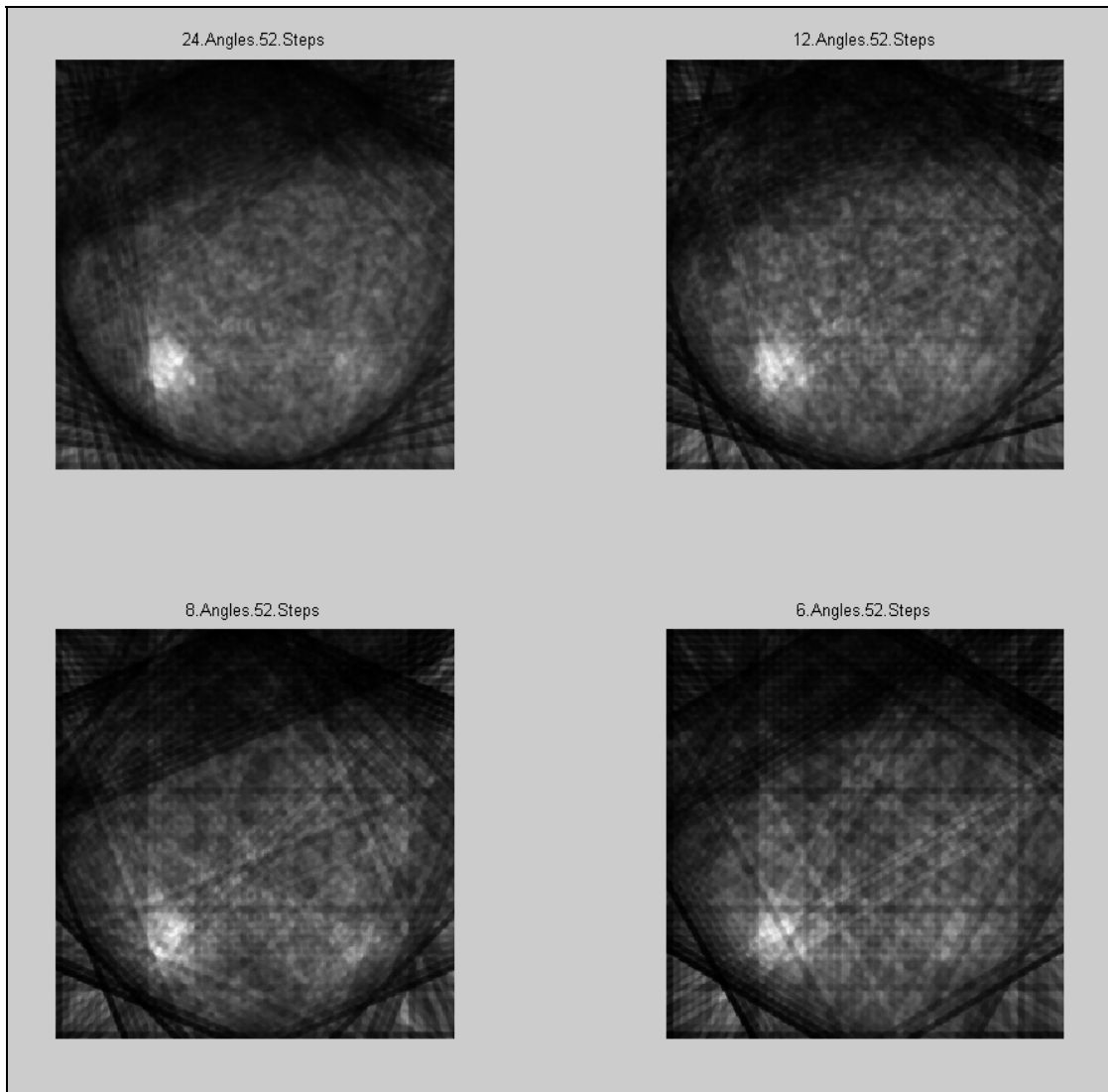


Figure 41. Effect of downsampling the number of angular positions on the reconstructed image.

Figure 41 shows the effect of downsampling the number of angles on the reconstructed image. For the two images acquired at 8 and 6 angles, the smooth circular border of the liver becomes more angular.

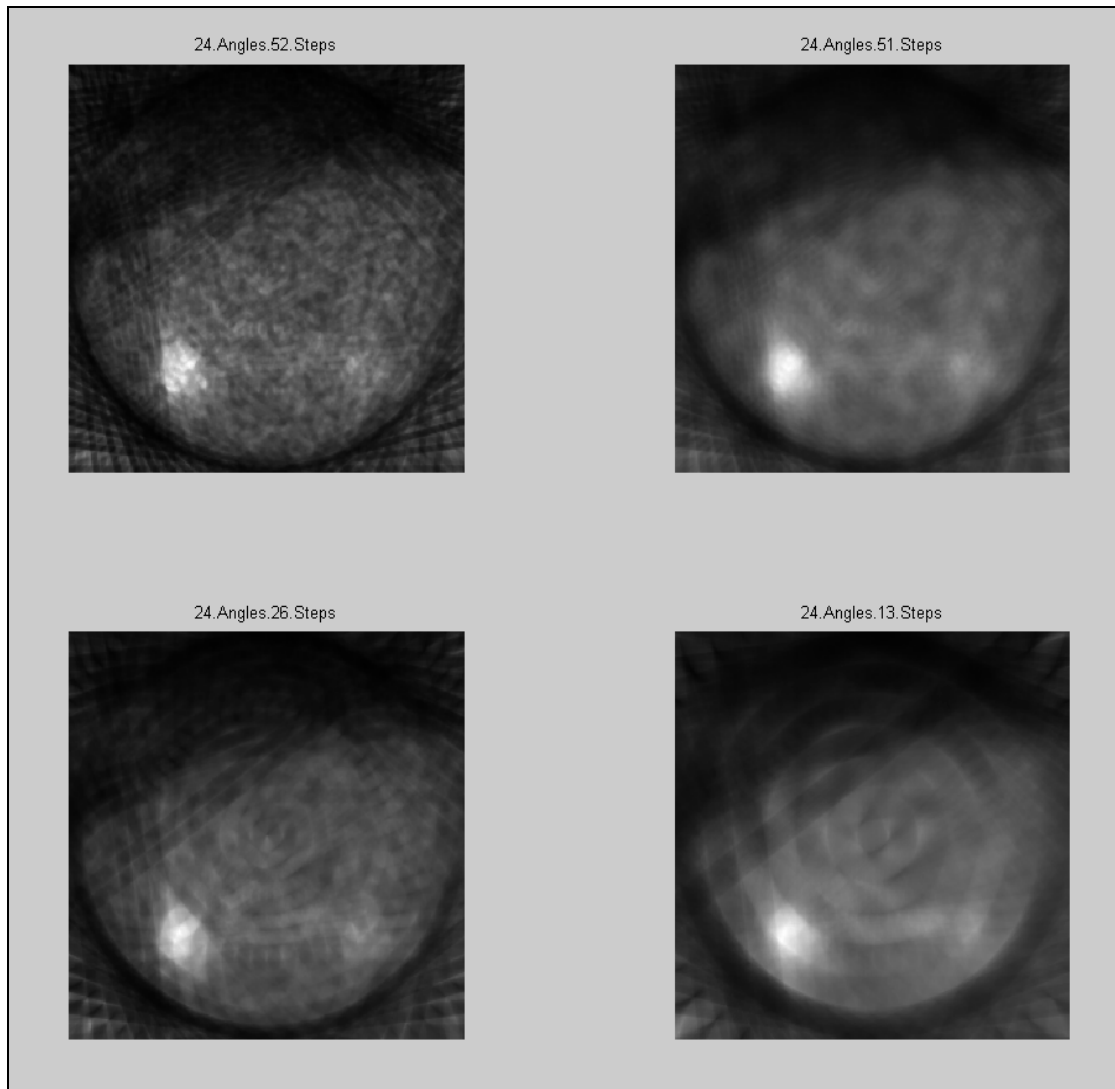


Figure 42. Effect of downsampling the number of spatial steps on the reconstructed image.

Figure 42 shows the effect of downsampling the number of spatial translation steps on the reconstructed image. In this tomographic acquisition, the degradation in the image is due to a combination of two factors, the loss in spatial sampling as well as an increase in the beam width. Therefore, with fewer translations steps used per angle, the image appears blurred.

The following section describes the analysis of each of the regions of interest in the reconstructed images.

6.3.3 ROC Analysis

The high-sampled images presented in the previous sections are both, aesthetically pleasing as well as encouraging for the performance of the NSECT technique. However, as the sampling parameters are reduced to generate undersampled geometries, the images begin to degrade considerably. Degradation of images will affect the accuracy of detection and quantification of iron overload. In order to optimize the simulation for a clinical system, the effects of varying each acquisition parameter must be analyzed for each set of parameters in consideration.

The accuracy of iron overload detection in the reconstructed image is analyzed through ROC analysis using the pixel value in the reconstructed image as the decision variable. The design of the ROC analysis is similar to that described in sensitivity analysis of the spectroscopy sample. Three regions of interest are selected corresponding to the three regions of iron concentration in the simulated sample, and their average pixel values are compared with each other to determine the accuracy of diagnosis. For the two nodules with iron concentrations 20 mg/g and 10 mg/g, pixel values are averaged within a 2 cm diameter circular region centered on the nodule. The 2 cm diameter is selected to avoid the spread in reconstructed pixel intensity that can be caused by sampling with a wide beam. The liver background is averaged within a 10 cm

diameter circular region centered at the center of the liver. Each region is selected based on apriori knowledge of the anatomy of the sample. The pixel intensity in the torso background is averaged for a sector shaped ROI located in the region of the torso that is scanned in every acquisition. The corners of the reconstructed image matrix that are not scanned in all projections are not included.

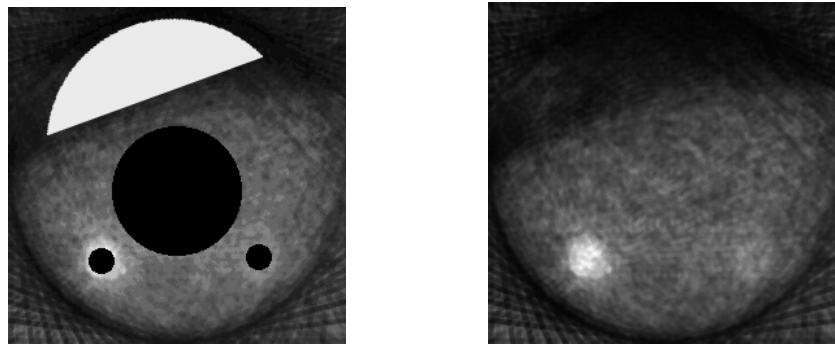


Figure 43. Regions corresponding to locations of known iron concentrations in the reconstructed image. The original image is shown for visual comparison. The pixel value within each region of interest is averaged and used as a decision variable for ROC analysis. The two ROIs corresponding to high iron concentration lesions (shown as small black circles) have diameter 2 cm, while the large ROI corresponding to liver background (large black circle) has diameter 10 cm. The torso background is estimated in a sector shaped region located in a portion of the torso that is scanned completely.

Comparisons are made for 3 combinations of pixel values within the ROIs.

- (a) 20 mg/g lesion and 5 mg/g liver
- (b) 10 mg/g lesion and 5 mg/g liver
- (c) 5 mg/g liver with the 0 mg/g torso

For each combination of parameters acquired, pixel values in the ROIs are averaged for the image reconstructed in iteration 15 of the MLEM algorithm for all 10 samples of a data set. ROC analysis is performed using LABROC analysis software to determine the area under the curve A_z .

As expected from the clarity of the 20 mg/g region in the reconstructed images, analysis of the 20 mg/g region against the 5 mg/g liver background showed a perfect Az value of 1 in almost all combinations of parameters investigated except when the neutron counts were brought down to 10000. Similar result was observed in the detection of the 5 mg/g liver vs the 0 mg/g torso with perfect Az value for all combinations until the number of neutrons is dropped to 10000.

Table 11 shows a summary of the ROC analysis for the 10 mg/g sample vs the 5 mg/g liver background.

Angular Positions	Spatial Positions	Incident neutrons				
		500000	250000	125000	75000	25000
24	52	1.00	1.00	0.97 ± 0.03	1.00	0.97 ± 0.04
	51	1.00	1.00	1.00	1.00	0.91 ± 0.05
	26	1.00	0.98 ± 0.01	0.90 ± 0.04	0.91 ± 0.05	0.90 ± 0.04
	13	0.97 ± 0.01	0.97 ± 0.01	0.92 ± 0.03	0.90 ± 0.03	0.91 ± 0.05
12	52	1.00	0.95 ± 0.02	0.98 ± 0.01	0.91 ± 0.04	0.98 ± 0.01
	51	1.00	0.86 ± 0.04	0.97 ± 0.02	0.90 ± 0.03	0.97 ± 0.03
	26	1.00	0.85 ± 0.05	0.94 ± 0.04	0.92 ± 0.01	0.94 ± 0.04
	13	0.97 ± 0.01	0.87 ± 0.04	0.85 ± 0.05	0.85 ± 0.03	0.86 ± 0.06
8	52	0.91 ± 0.03	0.95 ± 0.02	0.93 ± 0.03	0.89 ± 0.05	0.93 ± 0.05
	51	0.93 ± 0.02	0.88 ± 0.04	0.90 ± 0.04	0.86 ± 0.04	0.91 ± 0.05
	26	0.93 ± 0.02	0.89 ± 0.06	0.88 ± 0.05	0.83 ± 0.05	0.85 ± 0.06
	13	0.97 ± 0.02	0.90 ± 0.04	0.89 ± 0.03	0.84 ± 0.05	0.79 ± 0.07
6	52	0.90 ± 0.03	0.94 ± 0.01	0.86 ± 0.05	0.80 ± 0.04	0.86 ± 0.05
	51	0.98 ± 0.03	0.93 ± 0.03	0.80 ± 0.06	0.69 ± 0.05	0.63 ± 0.04
	26	0.99 ± 0.02	0.88 ± 0.04	0.77 ± 0.05	0.62 ± 0.04	0.65 ± 0.05
	13	0.82 ± 0.05	0.89 ± 0.05	0.71 ± 0.04	0.60 ± 0.06	0.55 ± 0.06

Table 11. Results of ROC analysis for the 10 mg/g lesion compared with the liver background. The ROC values for Az and their standard errors are obtained from LABROC software. Values corresponding to acquisition parameter combinations that are below the detection threshold of Az = 0.85 are shown shaded in gray.

As can be seen above, the values of Az are found to vary between 0.55 for the lowest sampled acquisition to a perfect value of 1 for the better sampled geometries. Higher values of Az are observed for the acquisitions that are sampled with a higher number of projections. However, the variation in Az observed quicker than the other two samples. This is consistent with visual examination of the reconstructed images, which show visible degradation in the 10 mg/g lesion with as many as 125000 neutrons in figure 40.

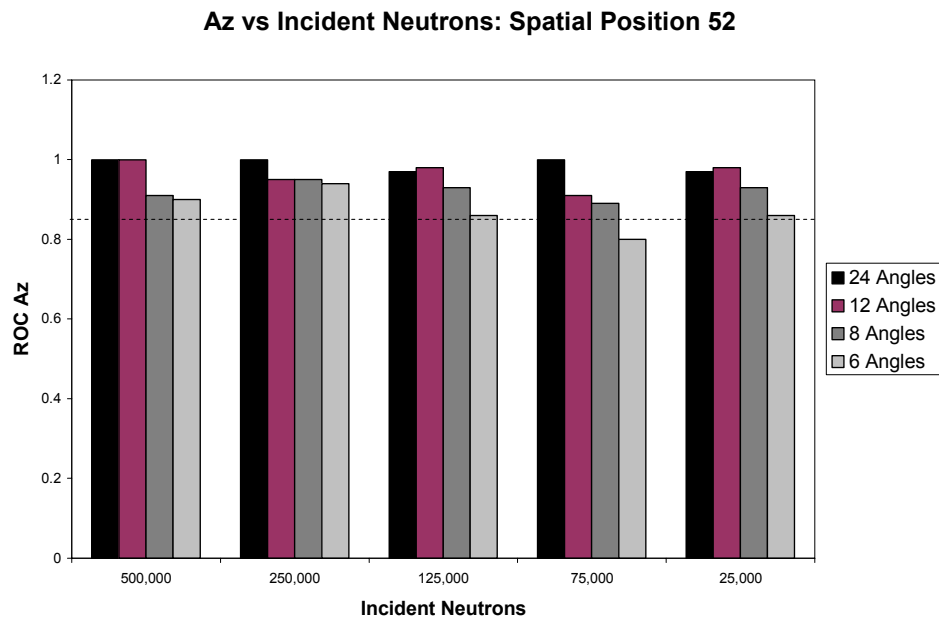


Figure 44. Variation in Az values with reducing neutron counts and angular positions for the 10 mg/g lesion. The number of spatial positions in this image is held constant at 52.

Az vs Incident Neutrons: Spatial Position 51

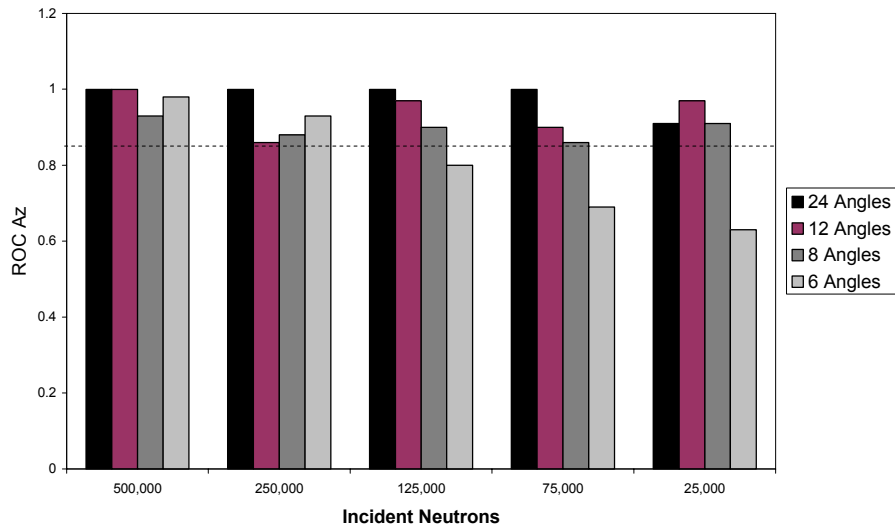


Figure 45. Variation in Az values with reducing neutron counts and angular positions for the 10 mg/g lesion. The number of spatial positions in this image is held constant at 51.

Az vs Incident Neutrons: Spatial Position 26

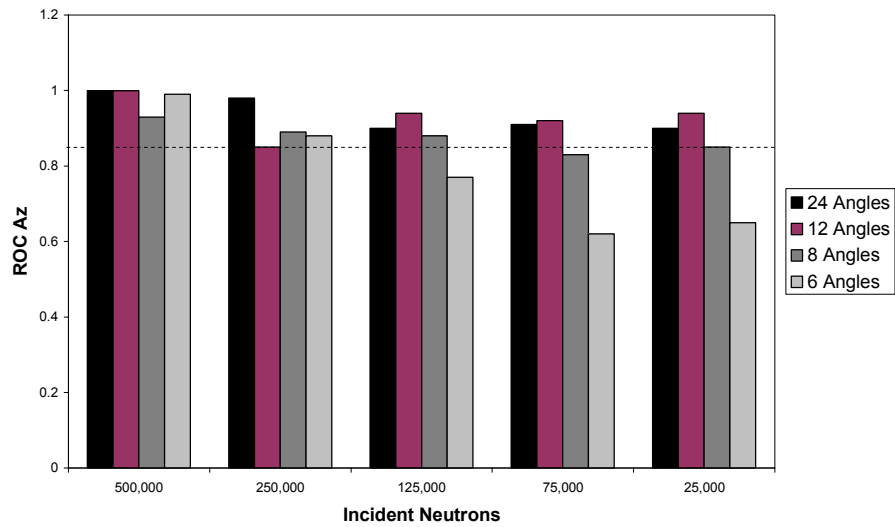


Figure 46. Variation in Az values with reducing neutron counts and angular positions for the 10 mg/g lesion. The number of spatial positions in this image is held constant at 26.

Az vs Incident Neutrons: Spatial Position 13

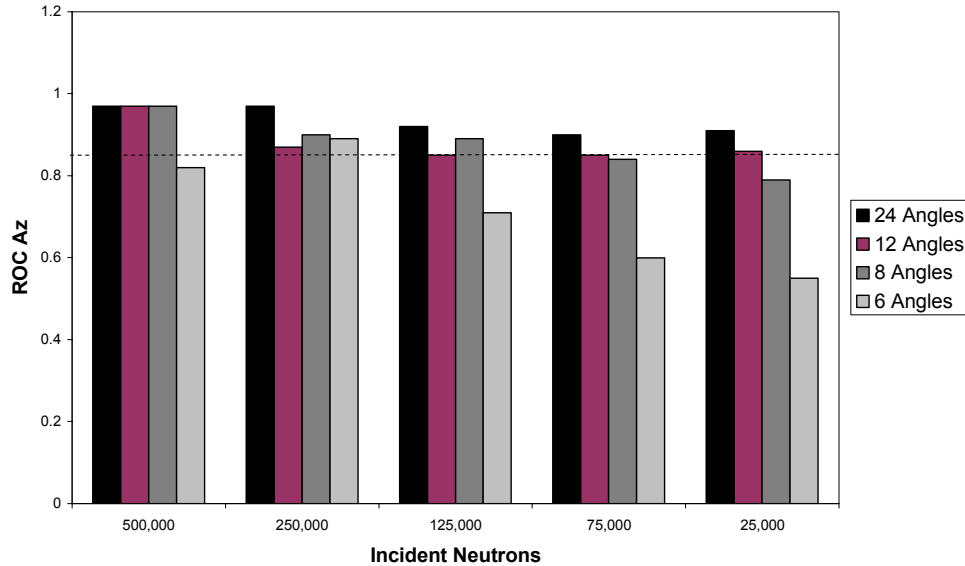


Figure 47. Variation in Az values with reducing neutron counts and angular positions for the 10 mg/g lesion. The number of spatial positions in this image is held constant at 13.

Three trends can be seen in the results of the ROC analysis for the 10 mg/g lesion. First, none of the individual parameters has a marked effect on the value of Az when the system is adequately sampled. Second, varying the number of angular positions has a more prominent effect on the value of Az compared to the other two parameters when the system is under-sampled. For example, for the combination of 6 angles, 25000 neutrons and 13 spatial positions, varying the number of angular positions while keeping the other two parameters constant changes Az by 0.36 (from 0.91 to 0.55), while varying the number of neutrons and spatial positions changes Az by 0.27 and 0.31 respectively. Third, varying the number of neutrons has a limited effect on the value of Az as long as the number is above a certain threshold. While the value of the threshold

is dependent to some extent on the other two parameters, it appears to be approximately 125000 for the ROC results presented above.

The 10 mg/g lesion can be detection above the background with $Az \geq 0.85$ for as few as 25000 neutrons per projection with 26 projections at 8 angles. When compensated for the increase in detection efficiency for the system from using larger detectors (10.3 x) and omitting elastic scatter (8 x), this result corresponds to a value of 2.06×10^6 neutrons per projections with 26 spatial locations and 8 angles.

To obtain an estimate of quantitative accuracy for the different parameter combinations, the pixel value in the 10 mg/g lesion is compared to the 20 mg/g lesion assuming the 20 mg/g lesion as a calibration standard. Table 12 shows the variation of the ratio of pixel values and the error compared to the expected value of 2. The difference between the expected and measured values varies between 1 % and 70 % for different combinations. The effect of downsampling the number of angles appears to have the most impact on the average pixel value within the reconstructed region. Within an angular position, the ratio of the pixel values of the two regions does not vary significantly. This suggests that the pixel value within a region in the tomographic image may be a realistic measure of its iron concentration provided the measurement is made against a calibration sample which his acquired using the same number of angles.

Angular Posn.	Spatial Posn.	Incident neutrons									
		500000		250000		125000		75000		25000	
		Value	Error	Value	Error	Value	Error	Value	Error	Value	Error
24	52	1.86	0.07	1.77	0.12	1.92	0.04	1.81	0.10	1.46	0.27
	51	1.79	0.10	1.69	0.15	1.84	0.08	1.73	0.14	1.35	0.32
	26	1.78	0.11	1.69	0.16	1.87	0.06	1.70	0.15	1.32	0.34
	13	1.67	0.16	1.74	0.13	1.97	0.01	1.74	0.13	1.63	0.18
12	52	1.90	0.05	1.55	0.22	1.78	0.11	1.66	0.17	1.71	0.14
	51	1.86	0.07	1.52	0.24	1.75	0.12	1.65	0.17	1.54	0.23
	26	1.84	0.08	1.49	0.25	1.69	0.15	1.59	0.20	1.51	0.25
	13	1.69	0.15	1.42	0.29	1.49	0.26	1.37	0.32	1.68	0.16
8	52	1.55	0.22	1.24	0.38	1.25	0.38	0.90	0.55	0.96	0.52
	51	1.50	0.25	1.18	0.41	1.18	0.41	0.87	0.57	0.83	0.59
	26	1.50	0.25	1.16	0.42	1.18	0.41	0.82	0.59	0.80	0.60
	13	1.50	0.25	1.32	0.34	1.34	0.33	0.98	0.51	1.31	0.35
6	52	1.68	0.16	1.36	0.32	1.59	0.20	1.48	0.26	1.49	0.26
	51	1.64	0.18	1.33	0.34	1.62	0.19	1.53	0.23	1.48	0.26
	26	1.65	0.18	1.35	0.32	1.52	0.24	1.38	0.31	1.29	0.35
	13	1.52	0.24	1.27	0.37	1.34	0.33	1.47	0.26	3.41	0.70

Table 12. Ratio of pixel values within the 10 mg/g and 20 mg/g lesions. The first column shows the ratio of pixel values while the second shaded column shows their difference from the expected value of 2.

From the ROC analysis, detection of the 5 mg/g liver against the torso background shows $A_z = 1.00$ for all combinations of 25000 neutrons implying that 25000 neutrons are adequate to make an accurate decision about the presence of iron in the liver. The second iron overload model with 5 mg/g and 3 mg/g lesions is therefore scanned with 250000 neutrons at each projection with a 24 angle acquisition to create 10 independent data sets with 25000 non-overlapping neutron counts in each set. To reduce

the computing time required to run the simulation, the number of spatial positions is limited to 26 with a 1 cm beam width.

ROC analysis is performed as described above to compare the 5 mg/g lesion and 3 mg/g lesion with the liver background. A summary of the results from ROC analysis for the 5 mg/g region is shown in table 13 below.

Angular Positions	Spatial Positions	Incident neutrons			
		50000	25000	15000	10000
24	26	0.91 ± 0.05	0.88 ± 0.05	0.82 ± 0.04	0.81 ± 0.04
	13	0.82 ± 0.04	0.83 ± 0.05	0.81 ± 0.04	0.79 ± 0.04
12	26	0.89 ± 0.05	0.82 ± 0.05	0.83 ± 0.04	0.79 ± 0.04
	13	0.81 ± 0.04	0.83 ± 0.04	0.76 ± 0.04	0.61 ± 0.04
8	26	0.86 ± 0.04	0.79 ± 0.04	0.77 ± 0.04	0.76 ± 0.05
	13	0.73 ± 0.05	0.66 ± 0.05	0.65 ± 0.05	0.66 ± 0.05
6	26	0.81 ± 0.05	0.80 ± 0.05	0.64 ± 0.05	0.51 ± 0.04
	13	0.72 ± 0.05	0.68 ± 0.05	0.65 ± 0.05	0.49 ± 0.04

Table 13. Results of ROC analysis for the 5 mg/g lesion compared with the normal liver background. The ROC values for Az and their standard errors are obtained from LABROC software. Values corresponding to acquisition parameter combinations that are below the detection threshold of Az = 0.85 are shown shaded in gray.

Only four combinations of acquisition parameters are able to detect the 5 mg/g lesion above background with Az > 0.85. Four of these require at least 50000 neutrons per projection. Only one combination of parameters with 25000 neutrons is able to get Az higher than the threshold value. However, this combination also requires 24 angles, which makes the total number of neutrons used in the projection equal to the number of neutrons in the 12 angle projection with 50000 neutrons per projection.

Az vs Incident Neutrons: Spatial Position 26

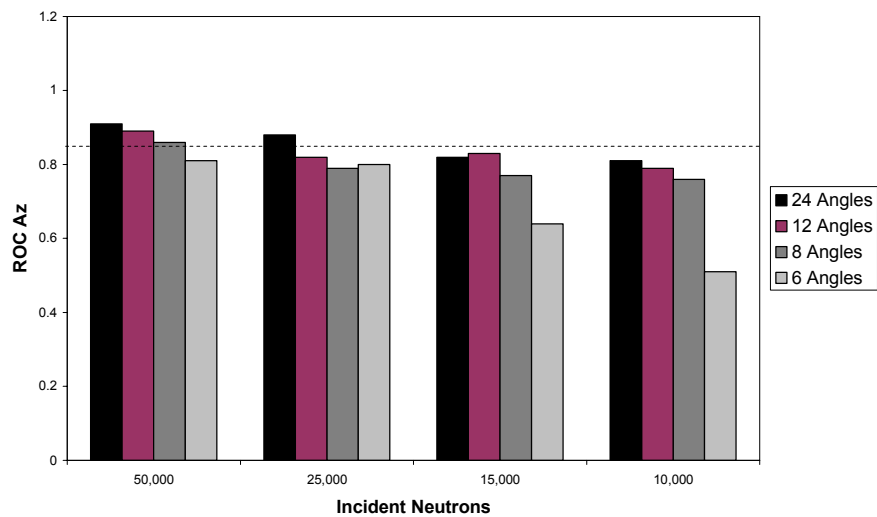


Figure 48. Variation in Az values with reducing neutron counts and angular positions for the 5 mg/g lesion. The number of spatial positions in this image is held constant at 26.

Az vs Incident Neutrons: Spatial Position 13

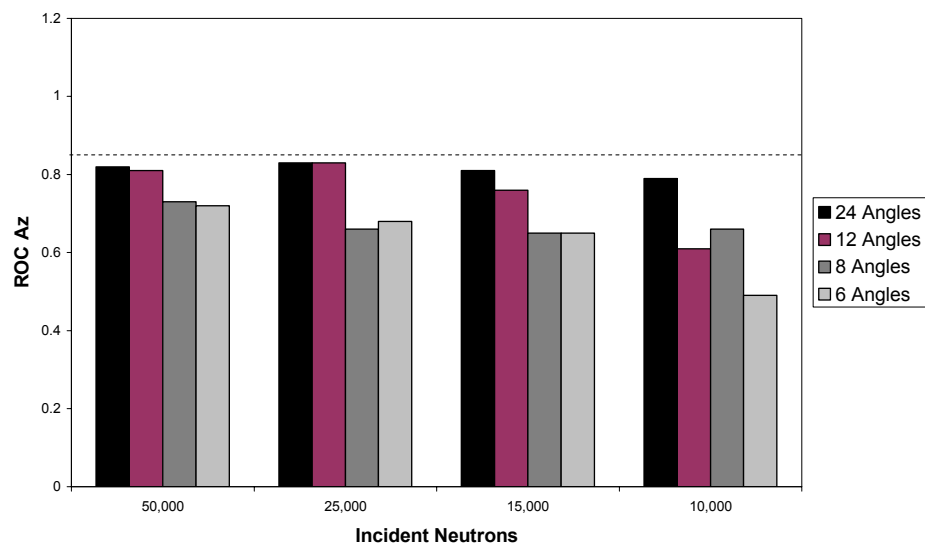


Figure 49. Variation in Az values with reducing neutron counts and angular positions for the 5 mg/g lesion. The number of spatial positions in this image is held constant at 13.

Table 14 shows a summary of the results for the 3 mg/g lesion. None of the acquisition combinations investigated is able to detect the lesion with $A_z \geq 0.85$. The standard errors in A_z observed for this lesion are also larger, making it difficult to draw any reasonable conclusions about the trends in its detectability.

Angular Positions	Spatial Positions	Incident neutrons			
		50000	25000	15000	10000
24	26	0.75 ± 0.08	0.64 ± 0.08	0.65 ± 0.11	0.61 ± 0.14
	13	0.62 ± 0.09	0.55 ± 0.10	0.59 ± 0.09	0.49 ± 0.13
12	26	0.61 ± 0.09	0.65 ± 0.09	0.63 ± 0.12	0.55 ± 0.11
	13	0.55 ± 0.13	0.63 ± 0.12	0.58 ± 0.11	0.52 ± 0.09
8	26	0.66 ± 0.13	0.53 ± 0.09	0.61 ± 0.09	0.57 ± 0.07
	13	0.55 ± 0.11	0.57 ± 0.13	0.54 ± 0.09	0.51 ± 0.09
6	26	0.63 ± 0.12	0.60 ± 0.11	0.61 ± 0.12	0.56 ± 0.11
	13	0.58 ± 0.12	0.49 ± 0.13	0.53 ± 0.13	0.49 ± 0.13

Table 14. Results of ROC analysis for the 3 mg/g lesion compared with the normal liver background. The ROC values for A_z and their standard errors are obtained from LABROC software. Values corresponding to acquisition parameter combinations that are below the detection threshold of $A_z = 0.85$ are shown shaded in gray.

Az vs Incident Neutrons: Spatial Position 26

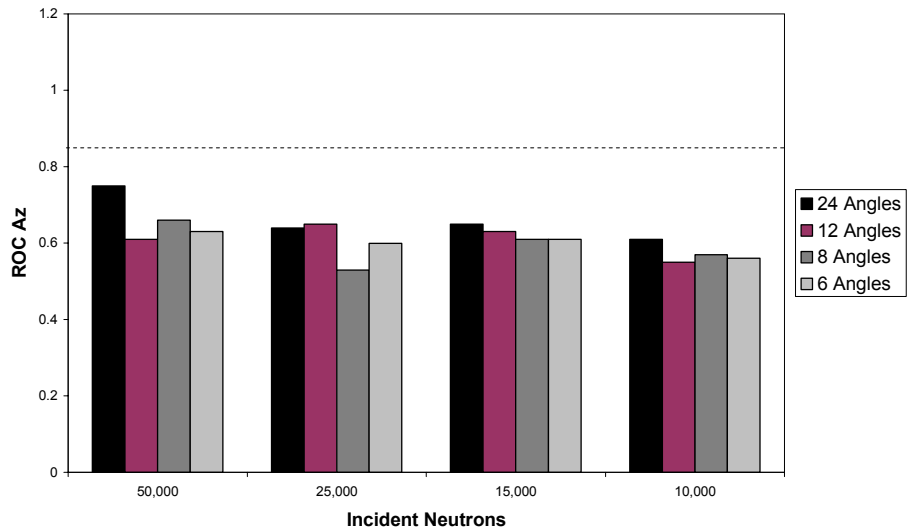


Figure 50. Variation in Az values with reducing neutron counts and angular positions for the 3 mg/g lesion. The number of spatial positions in this image is held constant at 26.

Az vs Incident Neutrons: Spatial Position 13

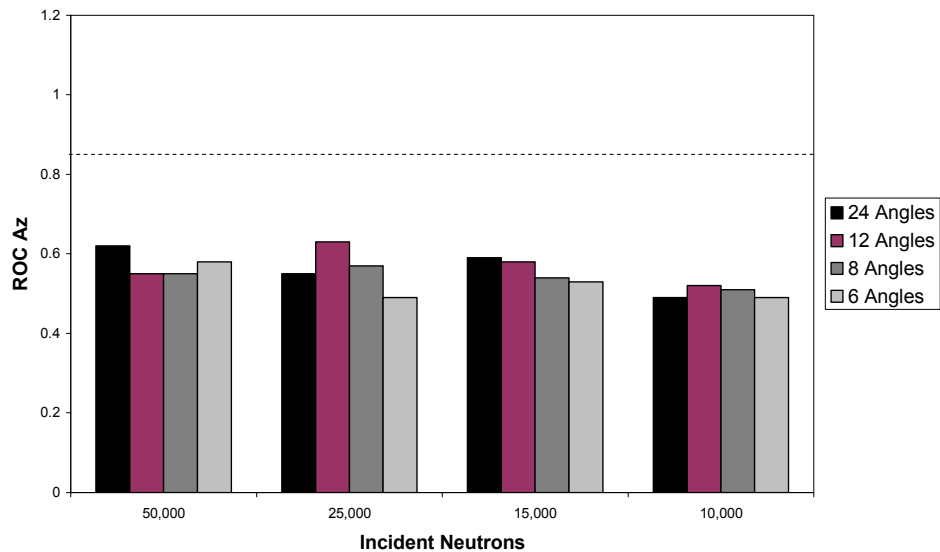
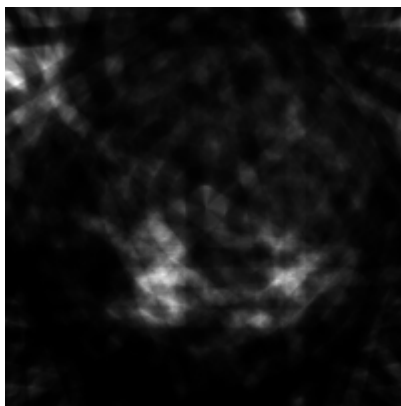


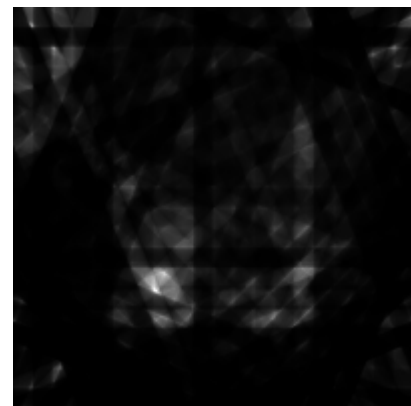
Figure 51. Variation in Az values with reducing neutron counts and angular positions for the 3 mg/g lesion. The number of spatial positions in this image is held constant at 13.

The analysis results indicate that a lesion with an iron concentration of 5 mg/g in a normal liver will require at least 50000 neutron counts per projection with at least 8 angles at 26 spatial locations. When compensated for the increase in detection efficiency for the system from using larger detectors (10.3 x) and omitting elastic scatter (8 x), this result corresponds to a value of 4.12×10^6 neutrons per projections with 26 spatial locations and 8 angles with a six-detector system.

To verify the feasibility of using the optimized acquisition geometry on a normal sized human torso, the optimized acquisition parameter set is used to scan a smaller liver measuring 17 cm major axis and 15 cm minor axis, filled with normal liver tissue. The liver contains lesions that are 3 cm diameter spheres with concentrations of 5 mg/g and 3 mg/g as before. Figure 52 shows the reconstructed image from the optimized scan of the smaller liver sample.



(a) 24 angles



(b) 8 angles

Figure 52. Reconstructed images for the optimized scan of a normal sized human liver sample. The liver measures 17 cm major axis and 15 cm minor axis, and contains 2 spherical lesions 3 cm in diameter, with iron concentrations of 3 mg/g and 5 mg/g.

Figure 52a shows the super-sampled reconstruction for 24 angles, while figure 52b shows the optimized reconstruction for 8 angles. In both images, the 3 mg/g lesion is visible more clearly than in the larger liver sample. This may be explained by the observation that although the 3 mg/g lesion contains the same amount of iron as in the larger sample, the reduction in the size of the torso reduces the scatter noise originating from the torso. Therefore, the overall SNR of the system is higher, allowing the 3 mg/g lesion to be detected.

To determine whether this combination of parameters is possible to implement in patients, the dose delivered from this scan must be calculated. The following chapter describes the simulation technique used to model NSECT patient dose and describes the optimal set of acquisition parameters for detection of iron overload in patients.

7. Optimization of NSECT Scanning Strategy

The final goal of all the research experiments described thus far is to optimize the NSECT acquisition system for iron overload detection in the liver. For spectroscopic scanning, the variable optimization parameter is the number of neutrons that are required to detect a certain concentration of iron in the liver. For tomography, however, the set of variable parameters that must be optimized contains 3 independent variables – the number of neutrons, angular positions and spatial positions. The NSECT simulations developed for spectroscopy and tomography have suggested a set of parameters that yield the best detection accuracy for both acquisition systems. However, for the sets of parameters to be truly optimal, they must also correspond to reasonable values of patient dose.

This chapter describes the final step of obtaining an estimate of patient dose from an NSECT scan and determining a truly optimal set of acquisition parameters that will provide maximum accuracy while delivering minimum dose.

7.1 Calculation of Patient Dose

Patient dose in NSECT is of significant concern because fast neutrons, which are the primary contributors of NSECT dose, have a dose quality factor (Q-factor) of 10. To achieve any chance of clinical success, the dose delivered to a patient from an NSECT

scan must be comparable to the dose from other ionizing imaging modalities in clinical use currently.

Dose analysis for an NSECT scan is performed by using GEANT4 to measure the energy deposited in an irradiated volume and converting the measured value to a total effective dose equivalent [62]. The dose-calculation process is summarized in 3 steps.

1. The GEANT4 simulation is used to estimate 2 parameters for an incident neutron beam:
 - i. the number of neutrons that interact in the volume of interest
 - ii. the average energy deposited per interacting neutron
2. The resulting energy deposited is converted from MeV to J/kg using the known mass of the volume of interest, which gives the absorbed energy in units of Gray (Gy).
3. The absorbed energy is multiplied by the quality factor for neutrons (10), and by the weighting factor for the organ of interest (0.05 for liver) to give the effective dose equivalent in units of Sieverts (Sv).

Measurement of deposited energy is performed by modifying the GEANT4 simulation of the spectroscopy liver sample to define the liver and torso volume as sensitive detectors. As described earlier, all sensitive detectors in GEANT4 can track and accumulate particle interactions and energy deposits in them thereby facilitating

measurement of the average energy deposited per incident neutron in each of these regions.

The physics-list of the dose estimation model contains interactions for neutrons and gamma-rays expected to occur at NSECT energy, as well as dose-contributing interactions for particles including positrons and electrons. Elastic scatter is a primary constituent of neutron dose which must be included in the dose model. All the techniques used to increase computational efficiency by turning off elastic scatter are removed from this model.

The liver sample is irradiated with 1 million neutron events using a 5 MeV simulated beam to measure the amount of energy deposited in the liver and the surrounding torso. For the simulation of 1 million neutron events incident on the liver, the average energy deposited per incident neutron is found to be 4.85 MeV. The dose calculation for the simulated spectroscopy liver is explained below and the relevant values are shown in table 15.

- Total number of neutrons required for spectroscopic quantification = 1×10^6
- Total energy deposited (MeV) = total number of neutrons x energy deposited per neutron
- Total energy deposited (J) = Total energy deposited (MeV) x 1.6×10^{-13} J/MeV
- Absorbed Dose = Total energy deposited / Mass of irradiated tissue

- Weighting factors: Neutron quality factor at 5 MeV = 10

Liver weighting factor (RBE) = 0.05

- Effective Dose Equivalent = Absorbed dose x Neutron Q-factor x Liver RBE

For this liver model, the mass of illuminated tissue is calculated based on the 1 cm² beam used for irradiation. For the spectroscopic liver model scanned with the geometry shown in figure 20, the beam illuminates a linear length of 20 cm. Considering a 1 cm² beam and liver density of 1.060 g/cm³, this gives an illuminated mass of 21.2 g.

Parameter	Calculated Value
Number of Incident Neutrons	1E+06
Total Energy Deposited (MeV)	4.85E+06
Total Energy Deposited (J)	7.75E-07
Mass of Liver (kg)	0.0212
Effective Dose (J/kg) Gy	3.71E-05
Neutron Q-factor	10
Liver RBE	0.05
Effective Dose Equivalent (mSv)	1.86E-02 = 0.02 mSv

Table 15. Effective dose delivered from an NSECT spectroscopy scan with 1 million incident neutrons.

The total dose from a single spectroscopic NSECT scan with 1 million incident neutrons is calculated to be 0.02 mSv, which is significantly lower than an abdominal X-ray exam which typically delivers 2 mSv [63].

For the tomography model, the most accurate method to calculate dose would be to perform a complete tomographic scan with 1 million neutron events incident on the liver. However, due to the low computational efficiency of performing this scan, an

approximation is used to determine the energy deposited from all projections acquired at 1 angle. The simulation is run with 26 spatial projections at the 90 degree position to illuminate the entire area of the liver as shown in figure 53. This acquisition geometry corresponds to the projection that will deliver maximum dose to the liver which makes this calculation an upper estimate of the patient dose.

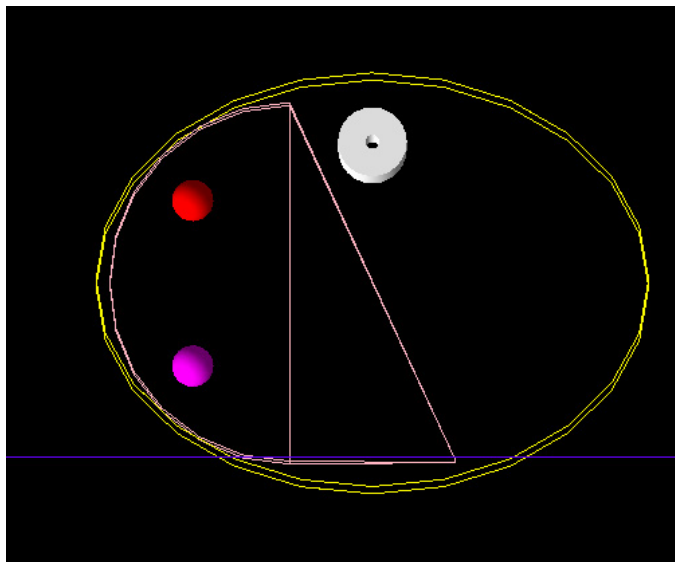


Figure 53. Geometry for scanning the tomographic liver to measure patient dose. The incident neutron beam is shown in blue. This projection angle corresponds to the maximum illumination of the liver and the torso.

Dose for this model is calculated separately for the liver region and the torso region, and the individual doses are then added. From the GEANT4 simulation for the tomography model, the average energy deposited per incident neutron is found to be 2.96 MeV for the liver and 1.33 MeV for the torso. The irradiated mass for both volumes is calculated as follows. A 1 cm² beam is used to illuminate the liver with a 26 cm diameter major axis. As the beam translates across the liver, it illuminates the entire

volume of the liver and torso that lies in the beam plane. The illuminated area for the liver is calculated by adding the areas of the semi-circular and trapezoidal regions to give 350 cm³ per tomographic slice. Therefore, with a density of 1.06 g/cm³ the mass of the liver scanned is 370 grams per angular projection. As each angle illuminates the same mass of the liver again, the dose calculated per angle can be added together over the total number of angles. Similarly, the illuminated mass of the torso is calculated as 590 grams per angular position. The optimal tomographic scanning geometry for this sample was determined to be 4.12×10^6 neutrons per projection with 26 spatial locations and 8 angles. With 4.12×10^6 neutrons per projection at 26 projections, the total number of neutrons per angular position is calculated as 1.07×10^8 neutrons per angle. Table 16 shows the dose calculation for the tomography model below.

Parameter	Liver	Torso
Number of Incident Neutrons	1.07E+08	1.07E+08
Total Energy Deposited (MeV)	3.18E+08	1.43E+08
Total Energy Deposited (J)	5.08E-05	2.29E-05
Mass of Liver (kg)	0.37	0.59
Effective Dose (J/kg) Gy	1.37E-04	3.86E-05
Neutron Q-factor	10	10
Liver RBE	0.05	0.05
Effective Dose Equivalent (mSv)	6.85E-02 = 0.07 mSv	1.93E-02 = 0.02 mSv

Table 16. Effective dose delivered from an NSECT tomography scan corresponding to the optimal set of acquisition parameters.

The dose delivered from the tomographic scan is 0.07 mSv for the liver and 0.02 mSv for the torso. The total patient dose is calculated as the sum of the liver and torso

dose as 0.09 mSv per angular position. Multiplying by 8 angles for the optimized 8-angle tomographic scan, the total patient dose is approximately 0.56 mSv. This value is significantly lower than an abdominal CT scan which typically delivers 10 mSv [63].

Both forms of NSECT examination have the potential to detect iron overload in the liver with sufficient accuracy at dose levels that are lower than other currently existing imaging modalities based on ionizing radiation. Based on the results described above, the optimum set of parameters for NSECT scanning can be discussed.

7.2 Optimum Acquisition Geometry

As mentioned earlier, the optimal scanning strategy for an NSECT scan is defined as the combination of parameters which provides the maximum accuracy at the minimum patient dose. In the current implementation of NSECT, the optimizable parameters are the neutron flux and the tomographic acquisition geometry, i.e. the number of angular and spatial projections used in sampling an object.

For a spectroscopy system, the optimal set of parameters is described in terms of the neutron flux irradiated onto a certain minimum concentration of iron. Results of the ROC analysis show that sufficient detection accuracy can be achieved in detecting 5 mg/g of iron with as few as 0.5 million neutrons, which corresponds to a dose of 0.01 mSv. However, at least 1 million neutrons are required to obtain reasonable quantitative accuracy in the spectrum, delivering a dose of 0.02 mSv to the patient.

For the tomography system, the optimal acquisition geometry is slightly more complicated, with 3 variables that can be individually modified. Of the 32 combinations analyzed through ROC analysis, only four combinations are able to detect a 5 mg/g lesion with $A_z > 0.85$. Table 17 shows the dose associated with each of these combinations. As the combination with 8 angles, 26 projections provides sufficient detection accuracy with minimum dose, it is described as the optimal parameter combination to scan a 5 mg/g lesion inside a normal iron concentration of 0 mg/g iron.

Angular Positions	Spatial Positions	Projections	Neutrons per projection	Total neutron fluence	Dose
24	26	624	4.12E+06	2.57E+09	1.6 mSv
24	26	624	2.06E+06	1.29E+09	0.84 mSv
12	26	312	4.12E+06	1.29E+09	0.84 mSv
8	26	208	4.12E+06	8.57E+08	0.56 mSv

Table 17. Dose values for different combinations of acquisition parameters.

8. Summary, Conclusion and Future Work

The purpose of this research project was to investigate the potential of iron overload detection through NSECT in a clinical scenario using simulations in GEANT4. Two simulations were developed and validated for both models of NSECT acquisition – spectroscopy and tomography. The validated simulations were used to determine whether iron overload detection was possible in a clinical scenario, and what optimal set of acquisition parameters could be used for each model. ROC analysis was used to determine detection accuracy, using the area under the ROC curve as the decision variable to determine accuracy. Finally, the simulation was used to determine the dose delivered to the patient from an NSECT scan.

8.1 Summary of Findings

Chapters 2 and 3 describe the theoretical principles of NSECT and the motivation behind its selection for detecting iron overload in patients. The theoretical principles of NSECT give it a unique advantage over other imaging modalities in its specificity to iron. The simulation has demonstrated that NSECT can identify iron even when it occurs amongst a host of other elements and isotopes, and when it occurs in extremely high quantities.

Chapter 4 discusses the design of the NSECT simulation developed for both acquisition models. GEANT4 was found to be an ideal simulation environment for the

NSECT system. The ease of modeling different objects and geometries facilitates the development and testing of several different samples and disease models. GEANT4's ability to track particle interactions in any object within the simulation makes it an ideal candidate for dose estimation studies. Samples were designed for system testing and evaluation as well as for two types of iron overload distribution in patients.

Chapter 5 discusses the validation and working of the NSECT spectroscopy system and describes its application to iron overload detection in patients. Simulated acquisition experiments were performed for several different concentrations of iron in the liver. ROC analysis determined that a concentration of 5 mg/g could be detected with $A_z > 0.85$ with as few as 0.5 million incident neutrons in a clinical system for iron overload diagnosis. However, at least 1 million neutrons are needed to achieve quantification accuracy of 85%. The dose corresponding to 1 million neutrons in this model was found to be 0.02 mSv, which is lower than an abdominal X-ray radiography exam.

Chapter 6 discusses the validation and working of the tomographic acquisition system and describes optimization experiments performed for tomographic detection of non-uniform iron overload. Two non-uniform distributions were investigated, one where a 3 cm diameter spherical lesion with 10 mg/g iron concentration was present in a liver with iron overload of 5 mg/g, and two, where a 5 mg/g lesion was present in a normal liver with no iron overload. The results of tomographic analysis showed that the

high concentration lesion with 10 mg/g could be detected above the 5 mg/g background within an iron overloaded liver with as few as 2 million neutrons per projection with 26 projections and 8 angles. For the second liver model, the 5 mg/g lesion could be detected with as few as 4 million neutrons per projection with 26 projections at 8 angles. The patient dose calculated for this acquisition geometry was 0.56 mSv which is lower than an abdominal CT exam. All of the optimization experiments were performed with a larger than normal liver in order to maximize the intensity of the signal from the liver. When the optimized parameters were tested on a normal sized liver, the 3 mg/g lesion was visible in the reconstructed image, most likely due to the reduction in scatter noise from the smaller torso.

Finally, chapter 7 describes the technique used for calculating dose in NSECT and validates the possibility of the different combinations of acquisition parameter being reasonable in terms of patient dose.

8.2 Conclusion

In conclusion, this work demonstrates that potential of NSECT to develop into a clinical diagnostic technique for detection of iron overload. NSECT's ability to detect clinically relevant concentrations of iron through spectroscopy and tomography has been demonstrated, and each model has been optimized for a set of acquisition parameters. The simulation designed in this work will greatly aid the experimental development of the NSECT technique. While the simulation is not a fully complete

model of the experimental technique, it provides a platform on which further development can take place.

8.3 Future Work

As the NSECT imaging technique continues to grow, it will require some improved detection and decision making tools to classify energy peaks from elements that have overlapping gamma lines. A possible way to approach the task is to use the GEANT4 simulation from this work to scan a variety of elements and isotopes and obtain simulated estimates of their relative line contributions to different energies. A classifier could be trained on the simulated data and be optimized to classify a peak as one of several possible elements based on the relative ratios of gamma lines present. The model could also be expanded to make a diagnostic decision based on the different elements detected.

An extremely useful approach to explore for NSECT would be non-uniform limited angle tomography. All the data analyzed in this work was acquired through uniform limited-angle tomography. Some of the parameter combinations at the lower end of the sampling set did not show adequate detection accuracy. However, the trends in the data were consistent with the higher-sampling combinations. A possibility that can be explored is whether these non-accurate low-dose scans can be used to obtain some preliminary information about the sample, which can then be used to acquire a

non-uniformly sampled image with higher sampling rates in regions with more information.

A third aspect that can be addressed is dose analysis. The dose analysis models described in this work obtain estimates for dose delivered to the liver tissue and surrounding torso based on calculations of energy deposits from GEANT4. However, what remains to be tested is how the distributed energy affects all the other organs around the irradiated region, i.e. is the energy deposited primarily in the liver delivering a large dose to a single organ, or is it distributed throughout the body resulting in a lower dose to each individual organ. This will require extensive simulation of a detailed model of the human body which incorporates other vital organs around the liver. Information about the temporal effects of dose on different tissue types can be used to determine whether a strategy of high dose - short scan can extract more information from the tissue than using a low dose - long scan.

Finally, experimental implementation of NSECT has several practical aspects that are not included in this simulation. For example, the simulation does not model detector electronic noise and dead time, two issues that are of practical concern. Consequently, a higher number of neutrons will be required to extract the same amount of information from the sample, thereby increasing patient dose further. All of these potential challenges must be investigated before NSECT can be implemented as a clinical imaging technique for in-vivo diagnosis of iron overload.

References

- [1] Floyd CE, Bender JE, Sharma AC, Kapadia AJ, Xia JQ, Harrawood BP, Tourassi GD, Lo JY, Crowell AS, and Howell CR, "Introduction to neutron stimulated emission computed tomography," *Physics in Medicine and Biology*, vol. 51, pp. 3375-3390, 2006.
- [2] Floyd CE, Howell CR, Harrawood BP, Crowell AS, Kapadia AJ, Macri R, Xia JQ, Pedroni R, Bowsher J, Kiser MR, Tourassi GD, Tornow W, and Walter R, "Neutron Stimulated Emission Computed Tomography of Stable Isotopes," *Proceedings of SPIE Medical Imaging 2004*, vol. 5368, pp. 248-254.
- [3] Schwartz A and Fink R, "Trace Elements in Normal and Malignant Human Breast Tissue," *Surgery*, vol. 76, pp. 325-329, 1974.
- [4] Rizk S and Sky-Peck H, "Comparison between concentrations of trace elements in normal and neoplastic human breast tissue," *Cancer Research*, vol. 44, pp. 5390-5394, 1984.
- [5] Yaman M, Atici D, Bakirdere S, and Akdeniz I, "Comparison of trace metal concentrations in malign and benign human prostate," *J. Med. Chem.*, vol. 48, pp. 630-634, 2005.
- [6] Ng KH, Bradley, D.A., Looi, L.M., "Elevated trace element concentrations in malignant breast tissues," *British Journal of Radiology*, vol. 70, pp. 375-382, 1997.
- [7] Milman N, Laursen J, Asnaes S, and Podenphant J, "Elements in normal and cirrhotic human liver tissue. II. Potassium, sulphur, chlorine and bromine measured by X-ray fluorescence spectrometry," *Liver*, vol. 7, pp. 206-10, 1987.
- [8] Milman N, Laursen J, Podenphant J, and Asnaes S, "Trace elements in normal and cirrhotic human liver tissue. I. Iron, copper, zinc, selenium, manganese, titanium and lead measured by X-ray fluorescence spectrometry," *Liver*, vol. 6, pp. 111-7, 1986.
- [9] Powell LW, "Diagnosis of hemochromatosis," *Semin Gastrointest Dis*, vol. 13, pp. 80-8, 2002.

- [10] Joffe S, "Hemochromatosis," N. Lamki, B. Coombs, U. Schmiedl, R. M. Krasny, and J. Karani, Eds., 2005.
- [11] Powell L, "Hemochromatosis," in *Harrison's Principles of Internal Medicine*, vol. 2, D. Kasper, Fawci, AS, Longo, DL, Braunwald, E, Hauser, SL, Jameson, JL, Ed., 16 ed. NY: McGraw Hill, 2005, pp. 2298-2303.
- [12] Garg A, V. Singh, et al., "An elemental correlation study in cancerous and normal breast tissue with successive clinical stages by neutron activation analysis," *Biological Trace Element Research*, vol. 46, pp. 185-202, 1994.
- [13] Ng K-H, Ong S-H, Bradley DA, and Looi L-M, "Discriminant analysis of normal and malignant breast tissue based upon INAA investigation of elemental concentration," *Appl. Radiat. Isot.*, vol. 48, pp. 105-109, 1997.
- [14] Engelhardt R, Langkowski JH, Fischer R, Nielsen P, Kooijman H, Heinrich HC, and Bucheler E, "Liver iron quantification: studies in aqueous iron solutions, iron overloaded rats, and patients with hereditary hemochromatosis," *Magn Reson Imaging*, vol. 12, pp. 999-1007, 1994.
- [15] Hollan SR, "Transfusion-associated iron overload," *Curr Opin Hematol*, vol. 4, pp. 436-41, 1997.
- [16] Cecchin E, De Marchi S, Querin F, Marin MG, Fiorentino R, and Tesio F, "Efficacy of hepatic computed tomography to detect iron overload in chronic hemodialysis," *Kidney Int*, vol. 37, pp. 943-50, 1990.
- [17] Brewer G, "Wilson Disease," in *Harrison's Principals of Internal Medicine*, vol. 2, D. Kasper, Fawci, AS, Longo, DL, Braunwald, E, Hauser, SL, Jameson, JL, Ed., 16 ed. NY: McGraw Hill, 2005, pp. 2313-2315.
- [18] Danielsen A, Steinnes, E., "A study of some selected trace elements in normal and cancerous tissue by neutron activation analysis," *J. Nuclear Med.*, vol. 11, pp. 260-264, 1970.
- [19] Ng KH, Bradley, D.A., Looi, L.M., Seman Mahmood, C., Khalik Wood, A., "Differentiation of elemental composition of normal and malignant breast tissue by instrumental neutron activation analysis," *Appl. Radiat. Isot.*, vol. 44, pp. 511-516, 1993.

- [20] Mutter J, Naumann J, Schneider R, and Walach H, "Mercury and Alzheimer's Disease.," *Fortschr Neurol Psychiatr*, 2007.
- [21] Lovell MA, Robertson JD, Teesdale WJ, Campbell JL, and Markesbery WR, "Copper, iron and zinc in Alzheimer's disease senile plaques," *J Neurol Sci*, vol. 158, pp. 47-52, 1998.
- [22] Cornett CR, Ehmann WD, Wekstein DR, and Markesbery WR, "Trace elements in Alzheimer's disease pituitary glands," *Biol Trace Elem Res*, vol. 62, pp. 107-14, 1998.
- [23] Andrasi E, Farkas E, Scheibler H, Reffy A, and Bezur L, "Al, Zn, Cu, Mn and Fe levels in brain in Alzheimer's disease," *Arch Gerontol Geriatr*, vol. 21, pp. 89-97, 1995.
- [24] Chmielnicka J and Nasiadek M, "The trace elements in response to lithium intoxication in renal failure," *Ecotoxicol Environ Saf*, vol. 55, pp. 178-83, 2003.
- [25] Zima T, Tesar V, Mestek O, and Nemecek K, "Trace elements in end-stage renal disease. 2. Clinical implication of trace elements," *Blood Purif*, vol. 17, pp. 187-98, 1999.
- [26] Zima T, Tesar V, Mestek O, and Nemecek K, "Trace elements in end-stage renal disease. 1. Methodological aspects and the influence of water treatment and dialysis equipment," *Blood Purif*, vol. 17, pp. 182-6, 1999.
- [27] Altekin E, Coker C, Sisman AR, Onvural B, Kuralay F, and Kirimli O, "The relationship between trace elements and cardiac markers in acute coronary syndromes," *J Trace Elem Med Biol*, vol. 18, pp. 235-42, 2005.
- [28] Nath R, "Copper deficiency and heart disease: molecular basis, recent advances and current concepts," *Int J Biochem Cell Biol*, vol. 29, pp. 1245-54, 1997.
- [29] Oster O, Dahm M, and Oelert H, "Element concentrations (selenium, copper, zinc, iron, magnesium, potassium, phosphorous) in heart tissue of patients with coronary heart disease correlated with physiological parameters of the heart," *Eur Heart J*, vol. 14, pp. 770-4, 1993.
- [30] Oster O, "Trace element concentrations (Cu, Zn, Fe) in sera from patients with dilated cardiomyopathy," *Clin Chim Acta*, vol. 214, pp. 209-18, 1993.

- [31] Oster O, Dahm M, Oelert H, and Prellwitz W, "Concentrations of some trace elements (Se, Zn, Cu, Fe, Mg, K) in blood and heart tissue of patients with coronary heart disease," *Clin Chem*, vol. 35, pp. 851-6, 1989.
- [32] Li CK, Chik KW, Lam CWK, To KF, Yu SCH, Lee V, Shing MMK, Cheung AYK, and Yuen PMP, "Liver disease in transfusion dependent thalassaemia major," *Arch Dis Child*, vol. 86, pp. 344-347, 2002.
- [33] Nash S, Marconi S, Sikorska K, Naeem R, and Nash G, "Role of liver biopsy in the diagnosis of hepatic iron overload in the era of genetic testing," *Am J Clin Pathol*, vol. 118, pp. 73-81, 2002.
- [34] Powell LW, George DK, McDonnell SM, and Kowdley KV, "Diagnosis of hemochromatosis," *Ann Intern Med*, vol. 129, pp. 925-31, 1998.
- [35] Villeneuve JP, Bilodeau M, Lepage R, Cote J, and Lefebvre M, "Variability in hepatic iron concentration measurement from needle-biopsy specimens," *J Hepatol*, vol. 25, pp. 172-7, 1996.
- [36] Butensky E, Fischer R, Hudes M, Schumacher L, Williams R, Moyer TP, Vichinsky E, and Harmatz P, "Variability in hepatic iron concentration in percutaneous needle biopsy specimens from patients with transfusional hemosiderosis," *Am J Clin Pathol*, vol. 123, pp. 146-52, 2005.
- [37] Brittenham G and Badman D, "Noninvasive measurement of iron: report of an NIDDK workshop," *Blood*, vol. 101, pp. 15-19, 2003.
- [38] Howard JM, Ghent CN, Carey LS, Flanagan PR, and Valberg LS, "Diagnostic efficacy of hepatic computed tomography in the detection of body iron overload," *Gastroenterology*, vol. 84, pp. 209-15, 1983.
- [39] Chapman RW, Williams G, Bydder G, Dick R, Sherlock S, and Kreel L, "Computed tomography for determining liver iron content in primary haemochromatosis," *Br Med J*, vol. 280, pp. 440-2, 1980.
- [40] Chezmar JL, Nelson RC, Malko JA, and Bernardino ME, "Hepatic iron overload: diagnosis and quantification by noninvasive imaging," *Gastrointest Radiol*, vol. 15, pp. 27-31, 1990.

- [41] Angelucci E, Giovagnoni A, Valeri G, Paci E, Ripalti M, Muretto P, McLaren C, Brittenham GM, and Lucarelli G, "Limitations of magnetic resonance imaging in measurement of hepatic iron," *Blood*, vol. 90, pp. 4736-42, 1997.
- [42] Wang ZJ, Haselgrove JC, Martin MB, Hubbard AM, Li S, Loomes K, Moore JR, Zhao H, and Cohen AR, "Evaluation of iron overload by single voxel MRS measurement of liver T2," *J Magn Reson Imaging*, vol. 15, pp. 395-400, 2002.
- [43] Ivanchenko VN, "Geant4 toolkit for simulation of HEP experiments," *Nuclear Instruments and Methods in Physics Research Section A*, vol. 502, pp. 666-668, 2003.
- [44] ICRU, International Commission on Radiation Units and Measurements, "Photon, electron, proton and neutron interaction data for body tissues." Bethesda, MD, ICRU Report 46, 1992.
- [45] Bender JE, Kapadia AJ, Sharma AC, Tourassi GD, Harrawood BP, and Floyd CE, "Breast cancer detection using Neutron Stimulated Emission Computed Tomography: prominent elements and dose requirements," *Medical Physics* (accepted), 2007.
- [46] National Nuclear Data Center BNL, "NuDat 2.3," 2007.
- [47] IAEA-NDS and NNDC, "Evaluated Nuclear Data Files (ENDF)."
- [48] Bauman JH and Hoffman RW, "Magnetic susceptibility meter for in vivo estimation of hepatic iron stores," *IEEE Trans Biomed Engg*, vol. BME-14, pp. 239-243, 1967.
- [49] Metz CE, "ROC methodology in radiologic imaging," *Invest Radiol*, vol. 21, pp. 720-33, 1986.
- [50] Metz CE, "ROC analysis software - LABROC."
- [51] Bushberg JT, Boone JM, Seibert JA, and Leidholdt EM, *Essential Physics of Medical Imaging*: Lippincot, Williams and Wilkin, 2001.
- [52] Kak AC and Slaney M, *Principles of Computerized Tomographic Imaging*. New York: IEEE Press, 1999.
- [53] Hsieh J, *Computed Tomography*. Washington: SPIE Press, 2003.

- [54] Dempster AP, Laird NM, and Rubin DB, "Maximum likelihood from incomplete data via the EM algorithm," *J R Stat Soc Series B*, vol. 39, pp. 1-38, 1977.
- [55] Sundberg R, "Maximum likelihood theory for incomplete data from an exponential family," *Scand J Stat*, vol. 1, pp. 49-58, 1974.
- [56] Shepp L and Vardi Y, "Maximum likelihood reconstruction for emission tomography," *IEEE Trans. Med. Imag.*, vol. MI-1, pp. 113-122, Oct.1982.
- [57] Stark H and Woods JW, *Probability and Random Processes with Applications to Signal Processing*. New Jersey: Prentice Hall, 2002.
- [58] Lange K and Carson R, "EM reconstruction Algorithms for Emission and Transmission Tomography," *Journal of Computer Assisted Tomography*, vol. 8, pp. 306-316, 1984.
- [59] Kapadia AJ, Floyd CE, Howell CR, and Harrawood BP, "Sampling Requirements for Neutron Stimulated Emission Computed Tomography," in *RSNA, Physics (Digital Imaging, PACS) session*. Chicago, IL, 2004.
- [60] Schumaker MA, Hackman G, et al., "Measured and simulated performance of Compton-suppressed TIGRESS HPGe clover detectors," *Nuclear Instruments and Methods in Physics Research Section A*, vol. 570, pp. 437-445, 2007.
- [61] Floyd CE, Kapadia AJ, Bender JE, Sharma AC, Xia JQ, Harrawood BP, Tourassi GD, Lo JY, Crowell AS, and Howell CR, "Neutron Stimulated Emission Computed Tomography of a Multi-Element Phantom," *IEEE Trans Med Imag (submitted)*, 2006.
- [62] Sharma AC, Harrawood BP, Kapadia AJ, Bender JE, and Tourassi GD, "Neutron Stimulated Emission Computed Tomography: a Monte Carlo simulation approach," *Physics in Medicine and Biology (submitted)*, 2007.
- [63] "Radiation Exposure in X-ray Examinations," in *American College of Radiology (ACR) and the Radiological Society of North America (RSNA)*, 2007.

Biography

Name: Anuj Jawahar Kapadia

Date of birth: July 18, 1979

Place of birth: Mumbai, India

Education

Duke University, Durham, NC

- Biomedical Engineering, Ph.D, expected Summer 2007

Dissertation: "Accuracy and Patient Dose in Neutron Stimulated Emission Computed Tomography for Diagnosis of Liver Iron Overload: Simulations in GEANT4".

Advisor: Georgia D. Tourassi, Ph.D. (Radiology)

Gregg E. Trahey, Ph.D (Biomedical Engineering)

University of Mumbai, Mumbai, India

- Biomedical Engineering, B. E, 2001

Senior project "Development of a Portable Backpack Ventilator"

Scholarships and Awards

Duke University, Durham, NC

Graduate Fellowship, Department of Biomedical Engineering, (2003 – 2007)

IEEE Nuclear Science Symposium and Medical Imaging Conference

Traineeship Award (2005, 2006)

U.S. Army Medical Research and Materiel Command (Breast Cancer Research Program)

Pre-doctoral Traineeship Award, 2006 – 2009

Yearbook of Nuclear Medicine Abstract Selection

Publication titled "Introduction to Neutron Stimulated Emission Computed Tomography" selected for abstraction, 2006

Grants and External Support

- US Army Breast Cancer Research Program

"Simulations to evaluate accuracy and patient dose in neutron stimulated emission computed tomography (NSECT) for diagnosis of breast cancer"

PI: Anuj Kapadia

Agency: DOD - BCRP (W81XWH-06-1-0484)

Period: 4/1/06 to 3/31/09

Funding: \$90,000

Publications

A. Refereed journal publications

1. Floyd CE, Bender JE, Sharma AC, **Kapadia AJ**, Xia JQ, Harrawood BP, Tourassi GD, Lo JY, Crowell AS, and Howell CR, "Introduction to neutron stimulated emission computed tomography," *Physics in Medicine and Biology*, vol. 51, pp. 3375-3390, 2006. (Abstract selected for the "Yearbook of Nuclear Medicine".)
2. Floyd CE, Sharma AC, Bender JE, **Kapadia AJ**, Xia JQ, Harrawood BP, Tourassi GD, Lo JY, Kiser MR, Crowell AS, Pedroni RS, Macri RA, Tajima S, and Howell CR, "Neutron Stimulated Emission Computed Tomography: Background Corrections,"

Nuclear Instruments and Methods in Physics Research Section B, vol. 254, pp. 329 - 336, 2007.

3. **Kapadia AJ**, Sharma AC, Bender JE, Tourassi GD, Howell CR, Crowell AS, Kiser MR, Harrawood BP, and Floyd CE, "Neutron Stimulated Emission Computed Tomography for Diagnosis of Breast Cancer," *IEEE Trans Nuc Sci* (accepted, 2007).
4. Sharma AC, Tourassi GD, **Kapadia AJ**, Harrawood BP, Crowell AS, Kiser MR, Howell CR, and Floyd CE, "Design and Development of a High-Energy Gamma Camera for use with NSECT Imaging: Feasibility for Breast Imaging," *IEEE Trans Nuc Sci* (accepted, 2007).

B. Refereed papers in review or preparation

1. Floyd CE, **Kapadia AJ**, Bender JE, Sharma AC, Xia JQ, Harrawood BP, Tourassi GD, Lo JY, Crowell AS, and Howell CR, "Neutron Stimulated Emission Computed Tomography of a Multi-Element Phantom," *IEEE Trans Med Imag*, (in review, 2007).
2. Sharma AC, Harrawood BP, **Kapadia AJ**, Bender JE, Tourassi GD, "Neutron Stimulated Emission Computed Tomography: a Monte Carlo simulation approach," *Physics in Medicine and Biology*, (in review), 2007.
3. **Kapadia AJ**, Sharma AC, Harrawood BP, Tourassi GD, Howell CR, Crowell AS, Kiser MR, "Experimental Validation of NSECT for Detection of Iron Overload in Liver," (in preparation).
4. **Kapadia AJ**, Harrawood BP, Tourassi GD, "A Monte-Carlo simulation for the NSECT acquisition matrix," (in preparation).

C. Refereed conference proceedings

1. Floyd CE, Howell CR, Harrawood BP, Crowell AS, **Kapadia AJ**, Macri R, Xia JQ, Pedroni R, Bowsher J, Kiser MR, Tourassi GD, Tornow W, and Walter R, "Neutron Stimulated Emission Computed Tomography of Stable Isotopes," *Proceedings of SPIE Medical Imaging 2004*, vol. 5368, pp. 248-254.
2. **Kapadia AJ** and Floyd CE, "An attenuation correction technique to correct for neutron and gamma attenuation in the reconstructed image of a neutron stimulated

- emission computed tomography (NSECT) system," *Proceedings of SPIE Medical Imaging 2005*, vol. 5745, pp. 737-743.
3. **Kapadia AJ**, Floyd CE, Bender JE, Howell CR, Crowell AS, and Kiser MR, "Non-invasive quantification of iron ^{56}Fe in beef liver using neutron stimulated emission computed tomography," *Proceedings of IEEE Nuclear Science Symposium, Medical Imaging Conference 2005*, vol. 4, pp. 2232-2234.
 4. Floyd CE, Bender JE, Harrawood BP, Sharma AC, **Kapadia AJ**, Tourassi GD, Lo JY, and Howell CR, "Breast cancer diagnosis using Neutron Stimulated Emission Computed Tomography: Dose and Count requirements," *Proceedings of SPIE Symposium on Medical Imaging 2006*, vol. 6142, pp. 597-603.
 5. Bender JE, Floyd CE, Harrawood BP, **Kapadia AJ**, Sharma AC, and Jesneck JL, "The effect of detector resolution for quantitative analysis of neutron stimulated emission computed tomography," *Proceedings of SPIE Medical Imaging 2006*, vol. 6142, pp. 1597-1605.
 6. **Kapadia AJ**, Sharma AC, Tourassi GD, Bender JE, Howell CR, Crowell AS, Kiser MR, and Floyd CE, "Neutron Spectroscopy of Mouse Using Neutron Stimulated Emission Computed Tomography (NSECT)," *Proceedings of IEEE Nuclear Science Symposium, Medical Imaging Conference 2006*.
 7. **Kapadia AJ**, Sharma AC, Tourassi GD, Bender JE, Howell CR, Crowell AS, Kiser MR, and Floyd CE, "Neutron Stimulated Emission Computed Tomography (NSECT) for Early Detection of Breast Cancer," *Proceedings of IEEE Nuclear Science Symposium, Medical Imaging Conference 2006*.
 8. **Kapadia AJ**, Sharma AC, Tourassi GD, Bender JE, Howell CR, Crowell AS, Kiser MR, and Floyd CE, "Non-Invasive Estimation of Potassium (^{39}K) in Bovine Liver Using Neutron Stimulated Emission Computed Tomography (NSECT)," *Proceedings of IEEE Nuclear Science Symposium, Medical Imaging Conference 2006*.
 9. Sharma AC, Tourassi GD, **Kapadia AJ**, Harrawood BP, Bender JE, Crowell AS, Kiser MR, Howell CR, and Floyd CE, "Design and Construction of a Prototype Rotation Modulation Collimator for near-Field High-Energy Spectroscopic Gamma Imaging," *Proceedings of IEEE Nuclear Science Symposium, Medical Imaging Conference 2006*.
 10. Sharma AC, Tourassi GD, **Kapadia AJ**, Bender JE, Xia JQ, Harrawood BP, Crowell AS, Kiser MR, Howell CR, and Floyd CE, "Development of a High-Energy Gamma

- Camera for Use with NSECT Imaging of the Breast," *Proceedings of IEEE Nuclear Science Symposium, Medical Imaging Conference 2006*.
11. Sharma AC, Floyd CE, Harrawood BP, Tourassi GD, **Kapadia AJ**, Bender JE, Lo JY, and Howell CR, "Rotating slat collimator design for high-energy near-field imaging," *Proceedings of SPIE Medical Imaging 2006*, vol. 6142, pp. 405-413.
 12. Sharma AC, Tourassi GD, **Kapadia AJ**, Crowell AS, Kiser MR, Hutcheson A, Harrawood BP, Howell CR, Floyd CE. "Elemental Spectrum of a Mouse Obtained via Neutron Stimulation." *Proceedings of the 2007 SPIE Symposium on Medical Imaging*, vol. 6510, 65100K, 2007.
 13. **Kapadia AJ**, Harrawood BP, Tourassi GD, " A Geant4 Simulation for Iron Overload Detection using NSECT," *IEEE Nuclear Science Symposium, Medical Imaging Conference*, (accepted, 2007).
 14. Sharma AC, **Kapadia AJ**, Harrawood BP, Tourassi GD, "Optimization of a Rotating Modulation Collimator for NSECT imaging," *IEEE Nuclear Science Symposium, Medical Imaging Conference*, (accepted, 2007).